First-principles calculations of magnetotransport and electron-phonon interactions in semiconductors and topological materials

Thesis by
Dhruv Chimanbhai Desai

In Partial Fulfillment of the Requirements for the
Degree of
Doctor of Philosophy

CALIFORNIA INSTITUTE OF TECHNOLOGY
Pasadena, California

2025
Defended September 12, 2024

ACKNOWLEDGEMENTS

I am very grateful to a lot of individuals who had a significant role in shaping my graduate school experience at Caltech. As a common tradition that aligns with the Indian culture, I would like to start by bowing down to my parents, Chimanbhai Desai and Harshidaben Desai, who have made immense sacrifices to ensure that I received the best possible education. They have always put my need ahead of theirs, and I could not have reached where I am without their love and support.

I would like to extend my sincerest gratitude to my advisor, Dr. Marco Bernardi, for his unwavering support and guidance during my PhD. I first met with him when I visited Caltech while still pursuing my undergraduate studies. Since then, all my conversations with him have been very inspiring, regardless of any challenges I faced in research. I believe Marco's approach and guidance are perfectly tailored to the needs of each student. I was still exploring my research goals when I joined Caltech, and Marco's ideas for potential directions ultimately guided the development of this work. I attribute a major portion of my personal and professional growth to Marco.

I thank all my thesis committee members, Dr. Brent Fultz, Dr. Jason Alicea, and Dr. Joseph Falson, for their invaluable feedback and advice.

I would like to thank all members of the Bernardi group, from whom I have learned so much during my time at Caltech. Particularly, I would like to thank Dr. Ivan Maliyov, who has served as an invaluable mentor and a friend to me. Ivan's dedication to work and his guidance are truly commendable. I would also like to thank Dr. Jinsoo Park, whose professional and personal guidance have been nothing short of inspiring. I am very grateful to Dr. Jin-Jian Zhou for patiently answering all my questions, especially during my initial years of graduate school. I thank Khoa Le, Shiyu Peng, and Yao Luo, who have always provided exciting research ideas, in addition to help and support in times of personal crisis. I also thank other members of the group (in no particular order): Dr. I-Te Lu, Dr. Hsiao-Yi Chen, Dr. Nien-En Lee, Dr. Benjamin Chang, Ina M. Sorensen, Kelly Yao, David Abramovitch, Sergei Kliavinek, Lauren Tan, Shaelyn Iyer, Dr. Sergio Pineda Flores, and others. I thank our department administrators, Christy Jenstad and Jennifer Blankenship, who have gone above and beyond to ensure a pleasant experience with the Applied Physics Department.

Lastly, I would like to thank all my friends here at Caltech and outside for all the great times we had, and my family members in the US for their unconditional love and support.

ABSTRACT

Understanding and predicting electron transport in novel materials is crucial to develop practical applications and accelerate materials discovery. Electron-phonon (e-ph) interactions are a key source of electron scattering and therefore play a dominant role in limiting electron transport under applied external fields. These interactions and the resulting phonon-limited charge transport can be calculated very accurately using *ab-initio* methods based on the semiclassical Boltzmann transport qquation (BTE), where electron and phonon properties are obtained using density functional theory (DFT) and density functional perturbation theory (DFPT) techniques. Despite these advances, first-principles calculations of magnetotransport are still in their infancy, primarily due to technical challenges associated with solving the BTE in the presence of a magnetic field. Additionally, calculations of electrical charge transport and magnetotransport in topological materials are lacking because of various technical challenges, including computational cost and the absence of a unified formalism combining electron scattering and band topology in the BTE. In this thesis, we develop a framework that incorporates these effects into the BTE to compute charge transport, magnetotransport, and topological transport regimes in several classes of conventional and quantum materials. Our magnetotransport calculations achieve excellent agreement with experiments, and we uncover an interplay of strong e-ph interactions and magnetic fields in graphene through a microsopic analysis of steady-state electron distributions. As a first step toward including band topology, we compute e-ph interactions and charge transport in the Dirac semimetal Na_3Bi, and find that specific two-dimensional phonons control charge transport near room temperature. These lattice vibrations induce a dynamic phase transition to a Weyl semimetal, providing a platform for ultrafast control of dynamical phases in Na_3Bi. Expanding into more advanced phenomena, we incorporate the electron Berry curvature in the BTE formalism and study topological transport effects such as the chiral anomaly and nonlinear Hall effect (NLHE). Our calculations provide an accurate quantitative framework and demonstrate the importance of e-ph interactions in accurately describing topological transport in quantum materials. Lastly, we compute e-ph interactions in a novel correlated metal, RuO_2 which has been widely studied for its unconventional magnetism. We uncover various interesting properties such as phonon softening, strong e-ph band renormalization, and a high superconducting T_c upon application of strain in RuO_2. Finally, we show a method to significantly accelerate all these calculations by compressing the matrices representing e-ph interactions. In summary, this thesis expands the scope of first-principles transport calculations to include magnetic fields and band topology. This enables future studies of electron dynamics in broad classes of novel quantum materials.

PUBLISHED CONTENT AND CONTRIBUTIONS

[1] Dhruv C. Desai, Bahdan Zviazhynski, Jin-Jian Zhou, and Marco Bernardi. Magnetotransport in semiconductors and two-dimensional materials from first principles. *Phys. Rev. B*, 103:L161103, Apr 2021. doi: 10.1103/PhysRevB.103.L161103.
D.C.D participated in the conception of the project, performed calculations, analyzed the data, and participated in the writing of the manuscript.

[2] Dhruv C. Desai*, Jinsoo Park*, Jin-Jian Zhou, and Marco Bernardi. Dominant two-dimensional electron–phonon interactions in the Bulk Dirac semimetal Na3Bi. *Nano Lett.*, 23(9):3947–3953, May 2023. doi: 10.1021/acs.nanolett.3c00713.
D.C.D participated in the conception of the project, performed calculations, analyzed the data, and participated in the writing of the manuscript.
*These authors contributed equally to this work.

[3] Dhruv C. Desai, Yao Luo, and Marco Bernardi. Electron-phonon band renormalization and superconductivity in strained RuO_2. *To be submitted*, 2024.
D.C.D participated in the conception of the project, performed calculations, analyzed the data, and participated in the writing of the manuscript.

[4] Dhruv C. Desai, Jin-Jian Zhou, Shiyu Peng, Jinsoo Park, and Marco Bernardi. First-principles magnetotransport with band topology for quantitative modeling of chiral anomaly and nonlinear Hall effect. *To be submitted*, 2024.
D.C.D participated in the conception of the project, performed calculations, analyzed the data, and participated in the writing of the manuscript.

[5] Yao Luo, Dhruv Desai, Benjamin K. Chang, Jinsoo Park, and Marco Bernardi. Data-driven compression of electron-phonon interactions. *Phys. Rev. X*, 14:021023, May 2024. doi: 10.1103/PhysRevX.14.021023.
D.D participated in the conception of the project, performed calculations, analyzed the data, and participated in the writing of the manuscript.

TABLE OF CONTENTS

LIST OF ILLUSTRATIONS

Chapter 1

INTRODUCTION

1.1 Overview

Transport phenomena can range from conventional charge transport in well-known metals and semiconductors to more advanced effects such as magnetotransport, band topology effects, and superconductivity. This physics finds applications across diverse fields. For example, magnetotransport has applications in memory storage and Hall sensors [1, 2], and topological materials, such as topological insulators [3] and topological semimetals [4], have novel transport properties with applications in quantum computing [5], thermoelectrics, and spintronics [6], among others.

These transport regimes can be described quantitatively in real materials by examining the microscopic scattering processes that govern charge transport. For instance, the Hall effect, which refers to the appearance of a Hall voltage on application of magnetic fields, is limited by electron scattering processes [7]. More recently, there has been a surge in the discovery of novel topological transport regimes such as the chiral anomaly [8] and nonlinear Hall effect (NLHE) [9]. The chiral anomaly, which refers to charge pumping between two Weyl cones on application of parallel electric and magnetic fields, requires a knowledge of both electron scattering processes and band topology. Another phenomenon with a similar physical origin is the NLHE, which leads to the generation of a nonlinear Hall voltage in materials without any external magnetic fields or magnetization. A detailed microscopic understanding of these phenomena requires new computational methods able to accurately describe electrons, phonons, their coupling, and topology in complex materials.

While electronic motions near and above room temperature are limited by various sources of scattering, these effects are governed by electrons scattering with phonons, or thermal atomic vibrations. Electron-phonon (e-ph) interactions are therefore key to understanding the microsopic processes governing charge transport, and the semiclassical equation that describes electronic dynamics in the presence of e-ph interactions is the Boltzmann transport equation (BTE). The BTE combines the effects of external fields and electron scattering into a set of coupled transport equations, which can be extended by adding the Berry curvature to account for nontrivial band topology. The remarkable versatility of the BTE lies in its applicability for a wide variety of materials with relatively weak e-ph interactions. However, one major limitation is the lack of closed-form solutions in the presence of scattering processes. Much theoretical work focuses on solving the BTE by using analytical techniques or numerically using constant relaxation times obtained empirically or estimated computationally [7]. This prompts the use of state-of-the-art numerical techniques for more accurate solutions.

In recent years, first-principles methods using density functional theory (DFT) [10] and density functional perturbation theory (DFPT) [11] have enabled accurate calculations of e-ph interactions and charge transport [12–17]. These calculations have demonstrated excellent agreement with experiments in a wide variety of materials. However, the current BTE framework is limited primarily to computation of charge and heat transport. A more general version that incorporates external magnetic fields, magnetism, or band topology is still missing. The primary reasons are technical and numerical challenges associated with solving the BTE when e-ph collisions, magnetic field, and Berry curvature are all present at once. For example, magnetotransport calculations evaluate derivatives in electron momentum space, and therefore typically require momentum grids much finer than a zero magnetic field calculation. Similarly, analyzing chiral anomaly and NLHE require additional calculations of electron Berry curvature to incorporate band topology. In turn, solving the BTE with Berry curvature is nontrivial and requires advanced techniques to avoid or integrate out singularities in the Berry curvature and predict sensible transport properties. Large unit cells and overall structural complexity of such materials further complicate the calculations.

In this thesis, we develop first-principles methods to address this physics. With these new tools, we study novel transport effects such as charge transport, magnetotransport and topological transport in semiconductors, topological semimetals, and other advanced quantum materials. Our primary goals are expanding the BTE framework and providing a deeper microscopic understanding of the above-mentioned effects. We derive expressions for the full BTE in the presence of magnetic field and Berry curvature, and implement them in our open-source code PERTURBO [18]. We also develop numerical techniques such as adaptive grid refinement for chiral anomaly calculations and finite-difference schemes for evaluating momentum-space derivatives for magnetotransport [19]. Our calculations are compared carefully with available experimental data. They provide a deeper insight into the interplay of e-ph interactions, electric and magnetic fields, and band topology. Overall, this work advances first-principles transport calculations, showing a quantitatively accurate framework to predict and understand magnetotransport phenomena in both conventional and topological quantum materials.

1.2 Charge transport and magnetotransport

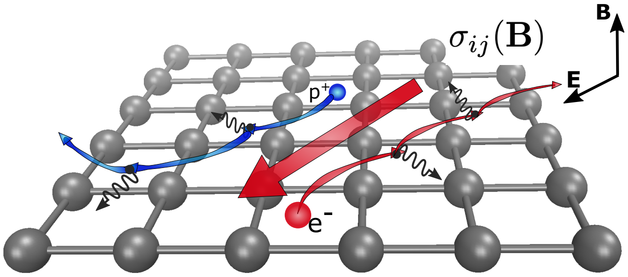

Figure 1.1: A Schematic illustration of electron (red) and hole (blue) motions under electric and magnetic fields, $\mathbf{E}$ and $\mathbf{B}$, respectively. The black wavy arrows represent phonons, and $\sigma_{ij}(\mathbf{B})$ is the conductivity tensor. This figure has been taken from the Editor's suggestion image representing our work in Ref. [20].

In the semiclassical approximation, electrons are viewed as localized wavepackets with position $\mathbf{x}$ and crystal momentum $\mathbf{k}$. Electronic motions in a lattice comprise two components: the drift terms due to applied electric and magnetic fields, and the scattering processes, particularly with phonons (Fig. 1.1) and impurities. The semiclassical equations of motion under applied electric and magnetic fields ($\mathbf{E}$ and $\mathbf{B}$ respectively) are given by [7]

$$\begin{aligned} \dot{\mathbf{x}} &= \frac{1}{\hbar}\frac{\partial \epsilon_{n\mathbf{k}}}{\partial k} \\ \dot{\mathbf{k}} &= -\frac{e}{\hbar}[\mathbf{E} + \dot{\mathbf{x}} \times \mathbf{B}], \end{aligned} \tag{1.1}$$

where $\epsilon_{n\mathbf{k}}$ is the electron band energy for crystal momentum $\mathbf{k}$ and band index n, while e and $\hbar$ denote the absolute value of electron's charge and Planck's constant respectively. In weak electric fields, the linear current response is described by the conductivity tensor σ_{ij}. Additionally, electrons acquire a transverse velocity on application of a magnetic field $\mathbf{B}$, which changes σ_{ij} and gives it a $\mathbf{B}$ dependence.

The electronic transport properties can be calculated using the BTE, which at steady-state takes the form [7]

$$\frac{df_{n\mathbf{k}}}{dt} = (\frac{\partial f_{n\mathbf{k}}}{\partial t})_{\text{forces}} + (\frac{\partial f_{n\mathbf{k}}}{\partial t})_{\text{e−ph}} = 0, \tag{1.2}$$

where we ignore impurity and other forms of scattering. The BTE expresses the principle of particle number conservation in a system. The changes in the electronic occupations $f_{n\mathbf{k}}$ due to external fields and e-ph scattering processes balance out at steady-state. One can solve for $f_{n\mathbf{k}}$ using Equations (1.1) and (1.2) and knowledge of the electron collisions. Additionally, from the steady state occupations $f_{n\mathbf{k}}$ (and their deviation from thermal equilibrium), we can calculate transport properties such as the conductivity and resistivity.

Beyond the classical picture: Berry phase and Berry curvature

While the semiclassical equations of motion (Eq. (1.1)) are sufficient to capture transport in conventional materials, additional quantum corrections are needed for the case of topological systems. We present a brief overview of these corrections in this section.

A complete quantum description of electrons is given by the Bloch wavefunctions $|\psi_{n\mathbf{k}}\rangle$. When external fields are applied, electrons move across the parameter space (in this case, the momentum $\mathbf{k}(t)$), and their time evolution is given by [21]

$$|\psi_n(t)\rangle = e^{i\theta_n(\mathbf{k}(t))} e^{i\gamma_n(\mathbf{k}(t))} |\psi_{n\mathbf{k}(t)}\rangle \, . \tag{1.3}$$

Here, $\theta_n(\mathbf{k}(t))$ is the dynamic phase acquired by the electrons:

$$\theta_n(\mathbf{k}(t)) = \frac{-1}{\hbar} \int_0^t dt' \epsilon_{n\mathbf{k}(t')}, \tag{1.4}$$

where $\epsilon_{n\mathbf{k}(t')}$ is the energy of the Bloch state $|\psi_{n\mathbf{k}}\rangle$. The non-trivial phase $\gamma_n(\mathbf{k}(t))$ is called the Berry phase, which can be derived by plugging the Bloch wavefunction into the time-dependent Schrondiger equation. As the electron moves through the parameter space $\mathbf{k}(t)$, the Hamiltonian changes adiabatically as $\hat{H}(\mathbf{k}(t))$, and the Schrodinger equation becomes

$$i\hbar\partial_t |\psi_n(t)\rangle = \hat{H}(\mathbf{k}(t)) |\psi_n(t)\rangle = \epsilon_{n\mathbf{k(t)}} |\psi_n(t)\rangle \, . \tag{1.5}$$

Plugging Eq. (1.3) into Eq. (1.5) and rearranging terms, we get

$$-\hbar \frac{d\gamma_{n\mathbf{k}(t)}}{dt} |\psi_{n\mathbf{k}(t)}\rangle + i\hbar \frac{\partial}{\partial t} |\psi_{n\mathbf{k}(t)}\rangle = 0. \tag{1.6}$$

If the electron traverses a closed path in $\mathbf{k}$- space from time t=0 to time t=t, one obtains

$$\begin{aligned} \gamma_n(\mathbf{k}(\mathrm{t})) &= \int_0^t \langle\psi_{n\mathbf{k}}(t)| \frac{\partial}{\partial t} |\psi_{n\mathbf{k}}(t)\rangle \, dt = \oint_{\mathbf{k}} d\mathbf{k} \cdot \langle\psi_{n\mathbf{k}}| \frac{\partial}{\partial \mathbf{k}} |\psi_{n\mathbf{k}}\rangle \\ &= \int d\mathbf{S} \cdot (\nabla_{\mathbf{k}} \times \langle\psi_{n\mathbf{k}}| \frac{\partial}{\partial \mathbf{k}} |\psi_{n\mathbf{k}}\rangle), \end{aligned} \tag{1.7}$$

where we used Stokes' theorem to convert the line integral to a surface integral in the last step. The quantity $\mathbf{A}_{n\mathbf{k}} = \langle\psi_{n\mathbf{k}}| \frac{\partial}{\partial\mathbf{k}} |\psi_{n\mathbf{k}}\rangle$ is called the Berry connection, and its curl $\mathbf{\Omega}_{n\mathbf{k}} = \nabla_{\mathbf{k}} \times \mathbf{A}_{n\mathbf{k}}$ is the Berry curvature.

The Berry curvature is gauge-invariant and is a fundamental quantity with observable consequences on electronic motions. It is key to describing band geometric and topological properties of a material. The simultaneous presence of external electric and magnetic fields and Berry curvature modifies the semiclassical wavepacket dynamics. Equations (1.1) become [21, 22]

$$\begin{aligned}\dot{\mathbf{x}} &= \frac{1}{\hbar}\frac{\partial\epsilon_{n\mathbf{k}}}{\partial k} - \dot{\mathbf{k}} \times \mathbf{\Omega}_{n\mathbf{k}} \\ \dot{\mathbf{k}} &= -\frac{e}{\hbar}[\mathbf{E} + \dot{\mathbf{x}} \times \mathbf{B}],\end{aligned} \tag{1.8}$$

which shows that the electrons now acquire an anomalous velocity given by $\dot{\mathbf{k}} \times \mathbf{\Omega}_{n\mathbf{k}}$.

Topological transport : Chiral anomaly and nonlinear Hall effect

The introduction of the anomalous velocity term in Equation (4.1) influences transport in systems with a finite Berry curvature. Part of this thesis aims to explore two such effects, namely the chiral anomaly and nonlinear Hall effect (NLHE). We provide a brief overview of these two effects in this section.

Topological semimetals are characterized by band crossings with linear band dispersion near the Fermi level. We consider a Weyl semimetal, a class of materials with two-fold band degeneracies near the Fermi level, commonly called Weyl nodes. The Weyl nodes act as sources and sinks of Berry curvatures, which exhibits large values in their vicinity [4]. Therefore, the anomalous velocity term in Equation (4.1) becomes important and influences transport significantly in the presence of external electric and magnetic fields. Particularly, the application of parallel electric and magnetic fields induces a charge pumping effect between two Weyl nodes with opposite Berry curvatures, causing a net increase in charge carriers near one node and a decrease near the other [8]. This phenomenon, called chiral anomaly, leads to a net increase in electrical conductivity along the direction of the applied fields. A related effect occurs in Dirac semimetals (materials with four-fold band degeneracies), where application of magnetic fields separates the Dirac nodes into pairs of Weyl nodes in momentum space, inducing a similar charge-pumping effect.

Let us also briefly discuss the physics of NLHE. In materials with time-reversal symmetry, the Hall conductivity, which measures the linear response of a transverse current to applied electric fields, is zero. A finite Hall response is achieved only by breaking the time-reversal symmetry, typically by applying external magnetic fields or in systems with finite magnetization. However, in time-reversal symmetric systems with a finite Berry curvature, it is possible to obtain a Hall response as a nonlinear effect in the applied electric field, but without any external magnetic field or magnetization [9, 23]. This response, which originates from the anomalous velocity term in Equation (4.1), is second-order in the electric field. The generation of a nonlinear Hall voltage in time-reversal symmetric materials is called the NLHE.

1.3 First-principles transport calculations

Numerical solution of the first-principles BTE relies on calculations of electrons, phonons and e-ph interactions. First-principles methods using DFT and DFPT provide state-of-the-art accuracy in predicting these properties. DFT has become increasingly widespread in the past three decades due to its tremendous predictive power in computing electronic properties such as the electronic ground state, wavefunctions and band energies. Similarly, DFPT, a linear response variant of DFT, enables accurate calculations of phonons and thermal properties in real materials. Recent years have seen a surge in the combined use of these two methods to compute e-ph interactions [12, 14, 15, 17, 24–26]. This section summarizes some of the first-principles methods employed in this thesis.

Electrons, phonons and electron-phonon interactions

We accurately compute the electronic structure, including the Bloch wavefunctions $|\psi_{n\mathbf{k}}\rangle$ and band energies $\epsilon_{n\mathbf{k}}$ by solving the Kohn-Sham (KS) Hamiltonian in DFT self-consistently, with the atomic positions as the only input [10]. The KS Hamiltonian is based on the Hohenberg-Kohn theorem, which states that the ground-state energy of a system is a unique functional of the charge density. Therefore, DFT is, in principle, an exact theory. However, construction of the KS Hamiltonian requires a knowledge of the electronic correlations, particularly the exchange-correlation terms. These terms are typically modelled using well-known approximations [27].

We implement our calculations using the QUANTUM ESPRESSO code [28, 29], which allows us to compute the charge density, wavefunctions $|\psi_{n\mathbf{k}}\rangle$, and energies $\epsilon_{n\mathbf{k}}$ on momentum grids of desired accuracy. We also calculate lattice dynamical properties such as the phonon dispersions ($\omega_{\nu\mathbf{q}}$), displacement eigenvectors ($\mathbf{e}^{\kappa\alpha}_{\nu\mathbf{q}}$), and perturbation potentials using QUANTUM ESPRESSO, where ν and $\mathbf{q}$ are the phonon mode index and momenta respectively. These calculations provide the quantities necessary to compute e-ph coupling matrices, which are defined as [18]

$$g_{mn\nu}(\mathbf{k},\mathbf{q}) = \sqrt{\frac{\hbar}{2\omega_{\nu\mathbf{q}}}} \sum_{\kappa\alpha} \frac{\mathbf{e}^{\kappa\alpha}_{\nu\mathbf{q}}}{\sqrt{M_\kappa}} \left\langle \psi_{m\mathbf{k}+\mathbf{q}} \right| \partial_{\mathbf{q},\kappa\alpha} V \left| \psi_{n\mathbf{k}} \right\rangle . \tag{1.9}$$

Here, $|\psi_{n\mathbf{k}}\rangle$ and $|\psi_{m\mathbf{k}+\mathbf{q}}\rangle$ represent the initial and final Bloch states, $\mathbf{e}^{\kappa\alpha}_{\nu\mathbf{q}}$ is the displacement of the atom κ (with mass M_κ) along direction α due to a phonon with momentum $\mathbf{q}$ and mode index ν, and $\partial_{\mathbf{q},\kappa\alpha}V$ is the corresponding perturbation potential. Therefore, $g_{mn\nu}(\mathbf{k},\mathbf{q})$ quantifies the amplitude of scattering between the Bloch states $|\psi_{n\mathbf{k}}\rangle$ and $|\psi_{m\mathbf{k}+\mathbf{q}}\rangle$ by either absorption or emission of a phonon $|\nu\mathbf{q}\rangle$.

Note that transport calculations require computing $g_{mn\nu}(\mathbf{k},\mathbf{q})$ on very fine $\mathbf{k}$- and $\mathbf{q}$-grids, typically of order 100 × 100 × 100 or finer. However, the large computational cost of DFPT limits the phonon grid sizes to much smaller values. Therefore, a practical implementation involves computing these matrix elements on relatively coarse grids of order 10 × 10 × 10, and then interpolating them to finer grids using maximally localized Wannier functions (MLWF) [30] from WANNIER90 [19] code. This interpolation and the full workflow are implemented in the open-source code PERTURBO developed in our group [18], which uses electron and phonon properties from QUANTUM ESPRESSO and MLWF from WANNIER90 as inputs to compute $g_{mn\nu}(\mathbf{k},\mathbf{q})$ on very fine grids.

Wannier interpolation of the electronic structure

Wannier interpolation relies on the construction of MLWF $|n\mathbf{R}_e\rangle$ in real space, with band index n and unit cell $\mathbf{R}_e$ [18],

$$|n\mathbf{R}_e\rangle = \frac{1}{N_{\mathbf{k}_c}} \sum_{\mathbf{k}_c} e^{-i\mathbf{k}_c\mathbf{R}_e} |\psi^{(W)}_{n\mathbf{k_c}}\rangle = \frac{1}{N_{\mathbf{k}_c}} \sum_{\mathbf{k}_c} e^{-i\mathbf{k}_c\cdot\mathbf{R}_e} \sum_m U_{mn}(\mathbf{k}_c) \left|\psi_{m\mathbf{k_c}}\right\rangle , \tag{1.10}$$

where $N_{\mathbf{k}_c}$ is the number of points in a coarse electron-grid represented by $\mathbf{k}_c$, $|\psi^{(W)}_{n\mathbf{k_c}}\rangle$ are Bloch states in the Wannier gauge, defined in the last step of Eq. (1.10), and $U_{mn}(\mathbf{k}_c)$ are unitary matrices relating the Bloch and the Wannier representations. The $U_{mn}(\mathbf{k}_c)$ matrices provide a degree of freedom to construct the Wannier functions, and are obtained by iterative solution to achieve maximum real-space localization.

We now construct the real-space electronic Hamiltonian $H_{mn}(\mathbf{R}_e) = \langle m\mathbf{0}| \hat{H} |n\mathbf{R}_e\rangle$. Using Eq. (1.10), we obtain

$$H_{mn}(\mathbf{R}_e) = \frac{1}{N_{\mathbf{k}_c}} \sum_{\mathbf{k}_c} e^{-i\mathbf{k}_c\cdot\mathbf{R}_e} H^{(W)}(\mathbf{k}_c) = \frac{1}{N_{\mathbf{k}_c}} \sum_{\mathbf{k}_c} e^{-i\mathbf{k}_c\cdot\mathbf{R}_e} (U^\dagger H(\mathbf{k}_c) U)_{mn}, \tag{1.11}$$

where $H(\mathbf{k}_c)$ and $H^{(W)}(\mathbf{k}_c)$ are momentum-space Hamiltonians in the Wannier and Bloch bases respectively.

Because the Wannier functions are localized in real-space, $H_{mn}(\mathbf{R}_e)$ decays rapidly as $|\mathbf{R}_e|$ increases away from the center of the supercell $|n\mathbf{0}\rangle$. As a result, the Hamiltonian in the Wannier function basis can be smoothly interpolated to any arbitrary electron momentum $\mathbf{k}$, using

$$H^{(W)}(\mathbf{k}) = \sum_{\mathbf{R}_e} e^{i\mathbf{k}\cdot\mathbf{R}_e} H(\mathbf{R}_e). \tag{1.12}$$

In addition, $H^{(W)}(\mathbf{k})$ can be further diagonalized to obtain the Bloch Hamiltonian using $H^{(W)}(\mathbf{k}) = U^\dagger(\mathbf{k}) H(\mathbf{k}) U(\mathbf{k})$. The quantity $H(\mathbf{k})$ is a diagonal matrix with energies $\epsilon_{n\mathbf{k}}$, and the matrices $U(\mathbf{k})$ are the eigenvectors of $H^{(W)}(\mathbf{k})$, representing the wavefunctions $|\psi_{n\mathbf{k}}\rangle$.

The e-ph coupling matrices are interpolated in a similar manner. One first constructs the e-ph matrix elements in Wannier basis using MLWF, and interpolates back to arbitrary $\mathbf{k}$- and $\mathbf{q}$- points using their localization property. Note that since $g_{mn\nu}(\mathbf{k}, \mathbf{q})$ depends on both electron and phonon momenta, the real-space transformation involves a double summation over coarse $\mathbf{k}_c$ and $\mathbf{q}_c$ grids, which can be viewed as a generalized double Fourier transform.

Berry curvature using Wannier interpolation

A final component necessary to compute transport in topological materials is the Berry curvature $\mathbf{\Omega}_{n\mathbf{k}}$. We summarize the formalism developed by Wang et al. to compute Berry curvature using MLWF [31].

We define a generalized rank-2 Berry curvature tensor with two band indices, $\mathbf{\Omega}_{mn,\alpha\beta}(\mathbf{k})$, in terms of the Berry connection $\mathbf{A}_{mn}(\mathbf{k}) = i \langle\psi_{m\mathbf{k}}| \partial_{\mathbf{k}} |\psi_{n\mathbf{k}}\rangle$:

$$\mathbf{\Omega}_{mn,\alpha\beta}(\mathbf{k}) = \partial_{k_\alpha} A_{mn,\beta} - \partial_{k_\beta} A_{mn,\alpha}, \tag{1.13}$$

where α,β are Cartesian directions. The physical Berry curvature $\mathbf{\Omega}_{n\mathbf{k}}$ can be expressed in terms of $\mathbf{\Omega}_{mn,\alpha\beta}(\mathbf{k})$ as

$$\Omega_{n\mathbf{k},\gamma} = \frac{1}{2}\epsilon_{\alpha\beta\gamma}\Omega_{nn,\alpha\beta}(\mathbf{k}), \tag{1.14}$$

where ϵ is the Levi-Civita tensor and we assume an implied summation over repeated indices α and β.

Using the formalism described in Ref. [31], we can compute the Berry curvature using the relation

$$\Omega_{\alpha\beta}(\mathbf{k}) = \bar{\Omega}_{\alpha\beta}(\mathbf{k}) - [D_\alpha(\mathbf{k}), \bar{A}_\beta(\mathbf{k})] + [D_\beta(\mathbf{k}), \bar{A}_\alpha(\mathbf{k})] - i[D_\alpha(\mathbf{k}), D_\beta(\mathbf{k})]. \tag{1.15}$$

Here, $\bar{\Omega}_{\alpha\beta}(\mathbf{k}) = U^\dagger(\mathbf{k})\Omega^{(W)}_{\alpha\beta}U(\mathbf{k})$ and $\bar{A}_\alpha(\mathbf{k}) = U^\dagger(\mathbf{k})A^{(W)}_\alpha U(\mathbf{k})$, where (W) denotes the Wannier gauge, and $U(\mathbf{k})$ is the unitary matrix obtained when constructing the MLWF, as described in the previous section (Eq. (1.10)). In addition, $D_{mn,\alpha}(\mathbf{k})$ is defined as

$$D_{mn,\alpha}(\mathbf{k}) \equiv (U^\dagger(\mathbf{k})\partial_{k_\alpha}U)_{mn} = \frac{\partial_{k_\alpha}\bar{H}_{mn}(\mathbf{k})}{\epsilon_{n\mathbf{k}} - \epsilon_{m\mathbf{k}}}(1 - \delta_{mn}). \tag{1.16}$$

The four quantities need to calculate the right-hand side of Eq. (1.15) can be computed in the Wannier gauge using the following relations:

$$\begin{aligned}
H^{(W)}_{mn}(\mathbf{k}) &= \sum_{\mathbf{R}} e^{i\mathbf{k}\cdot\mathbf{R}} \langle \mathbf{0}m| \hat{H} |\mathbf{R}n\rangle \\
\partial_{k_\alpha} H^{(W)}_{mn}(\mathbf{k}) &= \sum_{\mathbf{R}} e^{i\mathbf{k}\cdot\mathbf{R}} iR_\alpha \langle \mathbf{0}m| \hat{H} |\mathbf{R}n\rangle \\
A^{(W)}_{mn,\alpha}(\mathbf{k}) &= \sum_{\mathbf{R}} e^{i\mathbf{k}\cdot\mathbf{R}} \langle \mathbf{0}m| \hat{r}_\alpha |\mathbf{R}n\rangle \\
\Omega^{(W)}_{mn,\alpha\beta}(\mathbf{k}) &= \sum_{\mathbf{R}} e^{i\mathbf{k}\cdot\mathbf{R}} (iR_\alpha \langle \mathbf{0}m| \hat{r}_\beta |\mathbf{R}n\rangle - iR_\beta \langle \mathbf{0}m| \hat{r}_\alpha |\mathbf{R}n\rangle)
\end{aligned} \tag{1.17}$$

Since the WANNIER90 code allows us to calculate $\langle \mathbf{0}m| \hat{H} |\mathbf{R}n\rangle$ and $\langle \mathbf{0}m| \hat{r}_\alpha |\mathbf{R}n\rangle$, we can compute the quantities in the Wannier gauge using Eq. (1.17), and convert them to Bloch gauge using unitary transformations $U(\mathbf{k})$. The quantities in the Bloch gauge can be used to compute the Berry curvature using Eq. (1.15). This formalism is exact, and can be used to obtain the Berry curvatures accurately in real materials. We have implemented this formalism in PERTURBO.

Electron-phonon scattering rates, Boltzmann transport equation and charge transport

Using the semiclassical equations of motion and the steady-state BTE (Eqs. (1.1) and (1.2)), one can rewrite the linearized BTE in the presence of an external electric field as

$$\mathbf{v}_{n\mathbf{k}} = \frac{1}{\mathcal{N}_{\mathbf{q}}} \sum_{m,\nu\mathbf{q}} W^{\nu\mathbf{q}}_{n\mathbf{k},m\mathbf{k}+\mathbf{q}} (\mathbf{F}_{n\mathbf{k}} - \mathbf{F}_{m\mathbf{k}+\mathbf{q}}), \tag{1.18}$$

where $\mathbf{v}_{n\mathbf{k}}$ and $\mathcal{N}_{\mathbf{q}}$ are the band velocities and the number of $\mathbf{q}$- points used in the summation, respectively. Here, $\mathbf{F}_{n\mathbf{k}}$ represents the change in electronic occupations relative to thermal equilibrium, and is defined as $f_{n\mathbf{k}} - f^0_{n\mathbf{k}} = -f^0_{n\mathbf{k}}(1 - f^0_{n\mathbf{k}})\frac{e\mathbf{E}}{k_B T} \cdot \mathbf{F}_{n\mathbf{k}}$, while $W^{\nu\mathbf{q}}_{n\mathbf{k},m\mathbf{k}+\mathbf{q}}$ is the scattering rate from $|\psi_{n\mathbf{k}}\rangle$ to $|\psi_{m\mathbf{k}+\mathbf{q}}\rangle$ calculated using Fermi's golden rule. The total e-ph scattering rate for state $|\psi_{n\mathbf{k}}\rangle$ can be calculated as [18]

$$\begin{aligned} \Gamma_{n\mathbf{k}}(T) &= \frac{1}{\mathcal{N}_{\mathbf{q}}} \sum_{m,\nu\mathbf{q}} W^{\nu\mathbf{q}}_{n\mathbf{k},m\mathbf{k}+\mathbf{q}} \\ &= \frac{2\pi}{\hbar} |g_{mn\nu}(\mathbf{k},\mathbf{q})|^2 [\delta(\epsilon_{n\mathbf{k}} - \hbar\omega_{\nu\mathbf{q}} - \epsilon_{m\mathbf{k}+\mathbf{q}})(1 + N^0_{\nu\mathbf{q}} - f^0_{m\mathbf{k}+\mathbf{q}}) \\ &\qquad + \delta(\epsilon_{n\mathbf{k}} + \hbar\omega_{\nu\mathbf{q}} - \epsilon_{m\mathbf{k}+\mathbf{q}})(N^0_{\nu\mathbf{q}} + f^0_{m\mathbf{k}+\mathbf{q}})], \end{aligned} \tag{1.19}$$

where $f^0_{n\mathbf{k}}$ and $N^0_{\nu\mathbf{q}}$ are the Fermi-Dirac and Bose-Einstein distributions in thermal equilibrium at temperature T, respectively. The conductivity tensor σ_{ij}, defined as a linear response to the current density ($J_i = \sum_j \sigma_{ij} E_j$), can be expressed in terms of the occupation changes $\mathbf{F}_{n\mathbf{k}}$ using

$$\sigma_{ij} = \frac{e^2 S}{\mathcal{N}_{\mathbf{k}} \Omega k_{\mathrm{B}} T} \sum_{n\mathbf{k}} f^0_{n\mathbf{k}}(1 - f^0_{n\mathbf{k}})\, (\mathbf{v}_{n\mathbf{k}})_i (\mathbf{F}_{n\mathbf{k}})_j. \tag{1.20}$$

The addition of magnetic field and Berry curvature terms modifies Eq. (1.18). These will be discussed in more detail in Chapters 2 and 4.

1.4 Thesis outline

In this thesis, we systematically expand the scope of the BTE calculations to include magnetic fields and band topology.

Chapter 2 focuses on investigating magnetotransport phenomena in simple semiconductors, silicon and GaAs, and a two-dimensional material, graphene. We derive an expression for the linearized BTE in finite magnetic fields, and iteratively solve it to obtain the conductivity tensor and, consequently, the magnetotransport properties. Our calculations of magnetoresistance, Hall mobility, and the Hall factor demonstrate excellent agreement with experiments in Silicon and GaAs, and our magnetoresistance calculations in graphene predict large values, consistent with experiments. Additionally, we uncover magnetotransport signatures of e-ph interactions by analyzing steady-state occupations in graphene. This work provides a deeper insight into the microsopic mechanisms governing magnetotransport.

In Chapter 3, as a first step into topology, we analyze e-ph interactions and transport properties in the bulk topological semimetal (TSM) Na_3Bi. TSMs exhibits unconventional transport properties due to their linearly dispersing bandstructures near the Fermi level, but the nature of electronic interactions in these systems remains unexplored. Our calculations of e-ph interactions in Na_3Bi show that two-dimensional (2D) optical phonons associated with in-plane vibrations of Na atoms exhibit very strong e-ph coupling and dominates charge transport. We perform a real-space analysis of such 2D phonons and the associated perturbation potential, which explains the origin of strong e-ph coupling. We also find that atomic displacements along this 2D phonon induce a dynamical phase transition to a Weyl semimetal, with potential to engineer crystal structures with different phases on ultrafast timescales.

In Chapter 4, we advance our work to explore topological transport in several materials. We derive an expression for the linearized BTE using the modified semiclassical equations of motion in Eq. (4.1). Our approach extends the existing BTE formalism to include the Berry curvature. We perform magnetotransport calculations on the Weyl semimetal TaAs, and identify a positive contribution to magnetoconductance that arises from the Berry curvature terms. Additionally, our calculations of the NLHE and Berry curvature dipole in bulk $BaMnSb_2$, strained monolayer WSe_2 and bilayer WTe_2 are significantly altered when e-ph interactions are taken into account, highlighting the importance of these interactions in accurately quantifying nonlinear Hall transport. This work significantly extends the applicability of the BTE to study charge transport and magnetotransport in complex topological materials.

In Chapter 5, we examine the effects of e-ph interactions on novel properties beyond charge transport, such as band renormalization and superconductivity, in the correlated oxide RuO_2. RuO_2 exhibits unconventional properties such as altermagnetism, strain-induced superconductivity enhancement and metal-insulator transitions in thin films. In this work, we calculate phonons and e-ph interactions in strained

RuO_2, and find significant phonon anharmonicity upon application of strain. After including lattice anharmonicities using the temperature-dependent stochastic self-consistent harmonic approximation, we demonstrate two signatures of strong e-ph coupling: a kink in the bandstructure induced by e-ph corrections, and relatively high superconducting temperature T_c that is further enhanced by doping. Our calculations provide a detailed understanding of these phenomena, and show that e-ph interactions are the dominant mechanism for superconductivity in RuO_2.

In Chapter 6, we demonstrate a data-driven approach to compress e-ph interactions using singular value decomposition (SVD). Using a constrained-SVD method, we calculate physical properties such as mobilities, spin-relaxation times, e-ph band renormalization and superconducting critical temperature in various materials. We show that accurately predicting these properties requires only a small fraction of the total singular values, revealing the low-dimensional nature of e-ph interactions in addition to greatly accelerating the calculations. Our method opens up avenues to study larger systems previously limited by the high computational cost of e-ph interactions, advancing studies of quantum materials.

In Chapter 7, we briefly summarize the key achievements of this thesis, and explore potential future directions arising from this work.

References

[1] J. E. Lenz, Proc. IEEE **78**, 973 (1990).

[2] J. M. Daughton, J. Magn. Magn. Mater. **192**, 334 (1999).

[3] M. Z. Hasan and C. L. Kane, Rev. Mod. Phys. **82**, 3045 (2010).

[4] N. P. Armitage, E. J. Mele, and A. Vishwanath, Rev. Mod. Phys. **90**, 015001 (2018).

[5] M. He, H. Sun, and Q. L. He, Front. Phys. **14**, 43401 (2019).

[6] Q. L. He, T. L. Hughes, N. P. Armitage, Y. Tokura, and K. L. Wang, Nat. Mater. **21**, 15 (2022).

[7] J. M. Ziman, *Electrons and Phonons: the Theory of Transport Phenomena in Solids* (Oxford University Press, Oxford, 2001) p. 336.

[8] D. T. Son and B. Z. Spivak, Phys. Rev. B **88**, 104412 (2013).

[9] I. Sodemann and L. Fu, Phys. Rev. Lett. **115**, 216806 (2015).

[10] R. M. Martin, *Electronic Structure: Basic Theory and Practical Methods* (Cambridge University Press, 2004).

[11] S. Baroni, S. de Gironcoli, A. Dal Corso, and P. Giannozzi, Rev. Mod. Phys. **73**, 515 (2001).

[12] J.-J. Zhou and M. Bernardi, Phys. Rev. B **94**, 201201(R) (2016).

[13] V. A. Jhalani, J.-J. Zhou, and M. Bernardi, Nano Lett. **17**, 5012 (2017).

[14] W. Li, Phys. Rev. B **92**, 075405 (2015).

[15] T. Sohier, D. Campi, N. Marzari, and M. Gibertini, Phys. Rev. Mater. **2**, 114010 (2018).

[16] J.-J. Zhou, O. Hellman, and M. Bernardi, Phys. Rev. Lett. **121**, 226603 (2018).

[17] N.-E. Lee, J.-J. Zhou, H.-Y. Chen, and M. Bernardi, Nat. Commun. **11**, 1607 (2020).

[18] J.-J. Zhou, J. Park, I.-T. Lu, I. Maliyov, X. Tong, and M. Bernardi, Comput. Phys. Commun. **264**, 107970 (2021).

[19] A. A. Mostofi, J. R. Yates, G. Pizzi, Y.-S. Lee, I. Souza, D. Vanderbilt, and N. Marzari, Comput. Phys. Commun. **185**, 2309 (2014).

[20] D. C. Desai, B. Zviazhynski, J.-J. Zhou, and M. Bernardi, Phys. Rev. B **103**, L161103 (2021).

[21] D. Xiao, M.-C. Chang, and Q. Niu, Rev. Mod. Phys. **82**, 1959 (2010).

[22] G. Sundaram and Q. Niu, Phys. Rev. B **59**, 14915 (1999).

[23] Z. Z. Du, H.-Z. Lu, and X. C. Xie, Nat. Rev. Phys. **3**, 744 (2021).

[24] N.-E. Lee, J.-J. Zhou, L. A. Agapito, and M. Bernardi, Phys. Rev. B **97**, 115203 (2018).

[25] J. Park, J.-J. Zhou, V. A. Jhalani, C. E. Dreyer, and M. Bernardi, Phys. Rev. B **102**, 125203 (2020).

[26] J. Park, J.-J. Zhou, and M. Bernardi, Phys. Rev. B **101**, 045202 (2020).

[27] R. M. Martin, *Electronic Structure: Basic Theory and Practical Methods* (Cambridge University Press, 2004).

[28] P. Giannozzi, S. Baroni, N. Bonini, M. Calandra, R. Car, C. Cavazzoni, D. Ceresoli, G. L. Chiarotti, M. Cococcioni, I. Dabo, A. D. Corso, S. de Gironcoli, S. Fabris, G. Fratesi, R. Gebauer, U. Gerstmann, C. Gougoussis, A. Kokalj, M. Lazzeri, L. Martin-Samos, N. Marzari, F. Mauri, R. Mazzarello, S. Paolini, A. Pasquarello, L. Paulatto, C. Sbraccia, S. Scandolo, G. Sclauzero, A. P. Seitsonen, A. Smogunov, P. Umari, and R. M. Wentzcovitch, J. Phys. Condens. Matter **21**, 395502 (2009).

[29] P. Giannozzi, O. Andreussi, T. Brumme, O. Bunau, M. B. Nardelli, M. Calandra, R. Car, C. Cavazzoni, D. Ceresoli, M. Cococcioni, N. Colonna, I. Carnimeo, A. D. Corso, S. de Gironcoli, P. Delugas, R. A. DiStasio, A. Ferretti, A. Floris, G. Fratesi, G. Fugallo, R. Gebauer, U. Gerstmann, F. Giustino, T. Gorni, J. Jia, M. Kawamura, H.-Y. Ko, A. Kokalj, E. Küçükbenli, M. Lazzeri, M. Marsili, N. Marzari, F. Mauri, N. L. Nguyen, H.-V. Nguyen, A. O. de-la Roza, L. Paulatto, S. Poncé, D. Rocca, R. Sabatini, B. Santra, M. Schlipf, A. P. Seitsonen, A. Smogunov, I. Timrov, T. Thonhauser, P. Umari, N. Vast, X. Wu, and S. Baroni, J. Phys. Condens. Matter **29**, 465901 (2017).

[30] N. Marzari, A. A. Mostofi, J. R. Yates, I. Souza, and D. Vanderbilt, Rev. Mod. Phys. **84**, 1419 (2012).

[31] X. Wang, J. R. Yates, I. Souza, and D. Vanderbilt, Phys. Rev. B **74**, 195118 (2006).

Chapter 2

MAGNETOTRANSPORT IN SEMICONDUCTORS AND TWO-DIMENSIONAL MATERIALS FROM FIRST-PRINCIPLES

This chapter is a slightly modified version of the manuscript: D. C. Desai, B. Zviazhynski, J.-J. Zhou, and M. Bernardi, "Magnetotransport in semiconductors and two-dimensional materials from first principles", *Phys. Rev. B* **103**, L161103 (2021) (Editor's suggestion). D.C.D participated in the conception of the project, performed calculations, analyzed the data, and participated in the writing of the manuscript.

2.1 Introduction

Magnetic fields can strongly influence the electrical properties of materials, with changes quantified by magnetotransport coefficients such as the magnetoresistance (MR), Hall mobility, and Hall factor [1, 2]. In metals and semiconductors, the change in resistivity with magnetic field is typically small, but in certain semimetals, magnetic heterostructures and oxides the effects can be far greater or even dramatic, as in the case of giant and colossal MR [3, 4]. Magnetotransport is of practical relevance for various applications, including sensors [5], magnetoresitive RAM, and hard drives [6]. In addition, measurements of the carrier concentration and electrical mobility require knowledge of the Hall factor. Therefore it is important to understand the physical mechanisms governing magnetotransport and develop methods to accurately predict the MR and Hall factor.

Experimentally, magnetotransport has been studied extensively in metals [2] and simple semiconductors such as Si [7–12] and GaAs [13–15]. More recently, measurements on two-dimensional materials have shown unconventional behaviors, such as large non-saturating MR at high fields in graphene [16–18] and WTe_2 [19], and various studies have shown an interplay between band structure topology and magnetotransport, including the chiral anomaly and negative MR in topological semimetals [20–22]. These developments show that magnetotransport is a rapidly growing research arena.

Early attempts to formulate theories of magnetotransport phenomena [23] focused on approximate solutions of the Boltzmann transport equation (BTE) in the relaxation time approximation (RTA) [1]. Subsequent work using parametrized electronic band structures and electron-phonon (e-ph) interactions has shown calculations of the Hall factor in various materials [24, 25]. Approaches beyond the RTA have also been proposed, for example by solving BTE in polar semiconductors in terms of infinite determinants [26] or computing the phonon-limited Hall mobility in Si using deformation potential theory [27, 28]. These models lack analytic closed-form solutions, and thus were implemented numerically, highlighting the need for computational approaches to study magnetotransport.

In recent years, density functional theory (DFT) [29] and density functional perturbation theory (DFPT) [30] have enabled *ab initio* calculations of e-ph interactions. The resulting phonon-limited charge transport has been studied in various semiconductors and 2D materials in the framework of the BTE [31–39]. First-principles studies of magnetotransport have lagged behind—the only existing examples are two works by Macheda et al., who investigated an insulator (diamond) [40] and very recently the Hall factor in graphene [41] by solving the BTE in a magnetic field, as well as methods employing the Fermi surface topology to investigate magnetotransport [42]. However, first-principles calculations of magnetotransport in semiconductors are still missing and the MR in 2D materials has not yet been computed.

Here we show calculations of the MR, Hall mobility and Hall factor, as a function of temperature and magnetic field, in group-IV and polar semiconductors, focusing on the prototypical cases of Si and GaAs, and in graphene. Our approach, implemented in our open-source PERTURBO code [43], solves the linearized BTE in a magnetic field using Jacobi iteration (as opposed to conjugate gradient implemented in Ref. [40]) to obtain the conductivity tensor and from it the magnetotransport properties. The calculations employ *ab initio* e-ph interactions and include spin-orbit coupling (SOC), which is particularly important for holes. We evaluate $\mathbf{k}$-space derivatives from a central finite difference approximation [44] and obtain the conductivity using tetrahedron integration. To our knowledge, magnetotransport calculations employing such precise numerical techniques and correctly including SOC have not yet been reported. Extensive comparisons with experiments demonstrate the accuracy of our first-principles magnetotransport calculations for semiconductors. Analysis of the relative occupation changes in momentum space shows the dominant role of backscattering due to optical phonons and the breaking of the RTA in graphene. Taken together, our work demonstrates an accurate method to investigate magnetotransport in semiconductors and 2D materials and clarify the underlying microscopic mechanisms.

2.2 Methods

Magnetotransport properties and BTE

In the presence of small electric ($\mathbf{E}$) and magnetic ($\mathbf{B}$) fields, the current density $\mathbf{J}$ can be written as

$$J_i = \sum_{j=1}^{3} \sigma_{ij}(\mathbf{B}) E_j \tag{2.1}$$

with the conductivity tensor σ_{ij} expanded as [1]

$$\sigma_{ij}(\mathbf{B}) = \sigma_{ij}^{(0)} + \sigma_{ijk}^{(1)} B_k + \sigma_{ijkl}^{(2)} B_k B_l + \dots \tag{2.2}$$

with implied summations over repeated indices (which correspond to Cartesian components). We write the current in terms of electronic occupations $f_{n\mathbf{k}}$ and band velocities $v_{n\mathbf{k}}$ (n is the band index and $\mathbf{k}$ the crystal momentum of the electronic state),

$$\mathbf{J} = \frac{-Se}{\mathcal{N}_{\mathbf{k}}\Omega} \sum_{n\mathbf{k}} f_{n\mathbf{k}} \mathbf{v}_{n\mathbf{k}}, \tag{2.3}$$

where e is the absolute value of the electric charge, S the spin degeneracy, $\mathcal{N}_{\mathbf{k}}$ the number of unit cells, and Ω their volume. At steady-state, the BTE in the presence of both electric and magnetic fields reads [1]

$$e\frac{\partial f_{n\mathbf{k}}}{\partial \epsilon_{n\mathbf{k}}} \mathbf{v}_{n\mathbf{k}} \cdot \mathbf{E} + \frac{e}{\hbar}(\mathbf{v}_{n\mathbf{k}} \times \mathbf{B}) \cdot \nabla_{\mathbf{k}} f_{n\mathbf{k}} + \mathcal{I}^{\text{e−ph}}[f_{n\mathbf{k}}] = 0, \tag{2.4}$$

where $\epsilon_{n\mathbf{k}}$ are electronic energies, and the last term includes e-ph collision processes consisting of absorption or emission of a phonon [43]. Expanding $f_{n\mathbf{k}}$ to leading order in $\mathbf{E}$, we write $f_{n\mathbf{k}} - f^0_{n\mathbf{k}} = -f^0_{n\mathbf{k}}(1-f^0_{n\mathbf{k}})\frac{e\mathbf{E}}{k_BT} \cdot \mathbf{F}_{n\mathbf{k}}$, and solve for the unknown occupation changes $\mathbf{F}_{n\mathbf{k}}$ [43]. Factoring out $-e\mathbf{E}f^0_{n\mathbf{k}}(1-f^0_{n\mathbf{k}})/k_BT$, we obtain the linearized BTE

$$\begin{gathered}\mathbf{v}_{n\mathbf{k}} + \frac{e}{\hbar}(\mathbf{v}_{n\mathbf{k}} \times \mathbf{B})\nabla_{\mathbf{k}}\mathbf{F}_{n\mathbf{k}} = \\ \frac{1}{\mathcal{N}_{\mathbf{q}}} \sum_{m,\nu\mathbf{q}} W^{\nu\mathbf{q}}_{n\mathbf{k},m\mathbf{k}+\mathbf{q}} (\mathbf{F}_{n\mathbf{k}} - \mathbf{F}_{m\mathbf{k}+\mathbf{q}}),\end{gathered} \tag{2.5}$$

where ν is the phonon mode index, $\mathbf{q}$ the phonon wavevector, and $\mathcal{N}_{\mathbf{q}}$ the number of $\mathbf{q}$ points used in the summation. Here, $W^{\nu\mathbf{q}}_{n\mathbf{k},m\mathbf{k}+\mathbf{q}}$ is the scattering rate from $|n\mathbf{k}\rangle$ to $|m\mathbf{k}+\mathbf{q}\rangle$ and takes into account both phonon absorption and emission processes [43]. We solve for $\mathbf{F}_{n\mathbf{k}}$ by rearranging terms in Eq. (2.5) and using the iterative Jacobi scheme. For each iteration i, we get

$$\begin{aligned}\mathbf{F}^{(i+1)}_{n\mathbf{k}} = \mathbf{v}_{n\mathbf{k}}\tau_{n\mathbf{k}} &+ \frac{\tau_{n\mathbf{k}}}{\mathcal{N}_{\mathbf{q}}} \sum_{m,\nu\mathbf{q}} W^{\nu\mathbf{q}}_{n\mathbf{k},m\mathbf{k}+\mathbf{q}} \mathbf{F}^{(i)}_{m\mathbf{k}+\mathbf{q}} \\ &+ \frac{e}{\hbar}\tau_{n\mathbf{k}}(\mathbf{v}_{n\mathbf{k}} \times \mathbf{B})\nabla_{\mathbf{k}}\mathbf{F}^{(i)}_{n\mathbf{k}},\end{aligned} \tag{2.6}$$

where $\tau_{\mathrm{n}\mathbf{k}}$ is the relaxation time. The term containing the gradient in $\mathbf{k}$, $\nabla_{\mathbf{k}}\mathbf{F}_{n\mathbf{k}}$, is computed using the central finite difference approximation in Ref. [44]. Starting with the RTA solution as the initial guess, $\mathbf{F}_{n\mathbf{k}} = \mathbf{v}_{n\mathbf{k}}\tau_{n\mathbf{k}}$, we evaluate the right-hand side of Eq. (2.6) to update the solution $\mathbf{F}_{n\mathbf{k}}$, iterating this procedure until convergence.

Expanding $f_{n\mathbf{k}}$ in Eq. (2.3), we obtain [43]

$$\sigma_{ij} = \frac{e^2 S}{\mathcal{N}_{\mathbf{k}}\Omega k_{\mathrm{B}}T}\sum_{n\mathbf{k}} f^0_{n\mathbf{k}}(1 - f^0_{n\mathbf{k}})\,(\mathbf{v}_{n\mathbf{k}})_i(\mathbf{F}_{n\mathbf{k}})_j. \tag{2.7}$$

We can calculate the magnetotransport coefficients from this conductivity tensor because of its implicit dependence on $\mathbf{B}$ through Eq. (2.6). The MR can be obtained from the resistivity tensor $\rho(\mathbf{B}) = \sigma^{-1}(\mathbf{B})$ using [1]:

$$\mathrm{MR} = \frac{\rho(\mathbf{B}) - \rho(0)}{\rho(0)}. \tag{2.8}$$

At low fields, the MR is expected to be quadratic in the magnetic field [45]. In most materials, the MR perpendicular to $\mathbf{B}$ (transverse MR) is small and positive$-$classically, this increase in resistivity can be viewed as a result of the Lorentz force deviating charge carriers from their initial trajectories.

First-principles calculations typically compute the drift mobility μ_{d} in zero magnetic field, whereas in experiments a common practice is to obtain the mobility from Hall measurements [46]; the resulting Hall mobility is defined as $\mu_H = \sigma_{\mathrm{d}}R_{\mathrm{H}}$, where σ_{d} is the drift conductivity and R_{H} the Hall coefficient. In Drude theory, R_{H} evaluates to $1/ne$ for a carrier concentration n [1], so $\mu_{\mathrm{H}} = \mu_{\mathrm{d}}$. However, when the dependence of the relaxation time on electronic state is taken into account, R_{H} deviates from the Drude value by the Hall factor $r = \mu_{\mathrm{H}}/\mu_{\mathrm{d}}$ [24], so the Hall and drift mobilities differ by the Hall factor. For systems with cubic symmetry and $\mathbf{B}$ field in the z direction, the Hall factor is $r = ne\,\sigma^{(1)}_{xyz}/(\sigma^{(0)}_{xx})^2$ [25].

Computational details

We apply our approach to Si, GaAs and graphene. Their ground state is computed using DFT in the local density approximation, with a plane-wave basis set and norm-conserving pseudopotentials, using the QUANTUM ESPRESSO package. We use plane-wave kinetic energy cutoffs of 40 Ry for Si, 72 Ry for GaAs, and 90 Ry for graphene and relaxed lattice parameters of 5.43 for Si, 5.56 for GaAs, and 2.44 for graphene. The phonon dispersions and e-ph perturbation potentials on

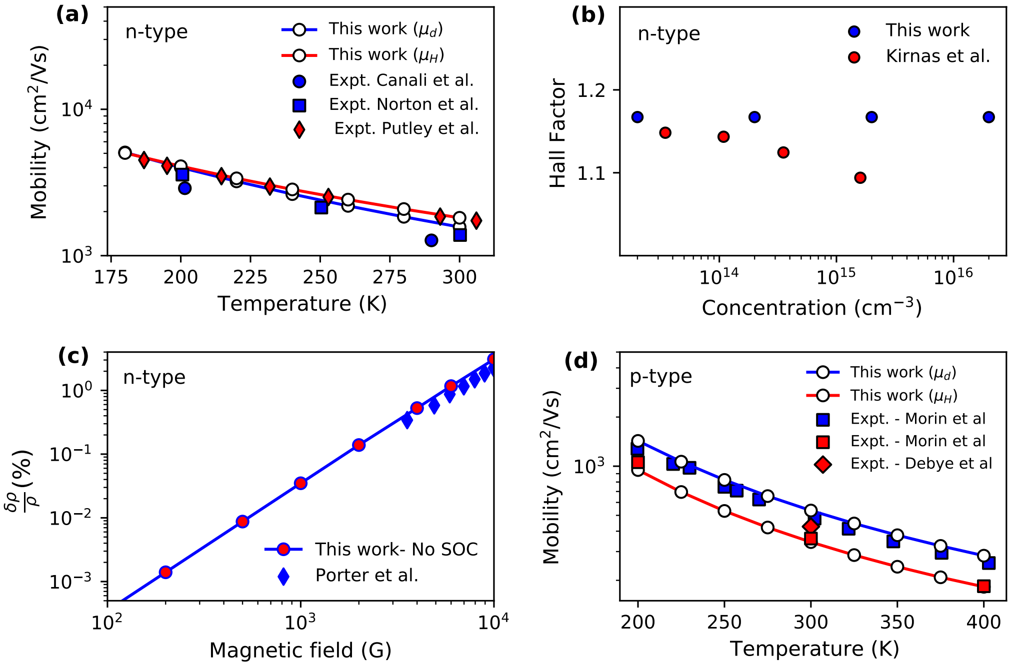

Figure 2.1: (a) Drift and Hall mobilities, in blue and red respectively, as a function of temperature in n-type silicon (experimental data are from Refs. [12, 50–52]). (b) Hall factor at 300 K as a function of carrier concentration in n-type silicon. (c) Transverse MR as a function of magnetic field in n-type silicon, compared with experiments from Ref. [8]. (d) Drift and Hall mobilities as a function of temperature in p-type silicon (experimental data are taken from Refs. [9, 11, 53]).

coarse $\mathbf{q}$-point grids are computed with DFPT [47] and the Wannier functions are obtained using WANNIER90 [48]. We use coarse electron $\mathbf{k}$-point and phonon $\mathbf{q}$-point grids of $8 \times 8 \times 8$ for Si and GaAs and $36 \times 36 \times 1$ $\mathbf{k}$- and $18 \times 18 \times 1$ $\mathbf{q}$-points for graphene. We compute and interpolate the e-ph matrix elements using our PERTURBO open source package [43]. Calculations with SOC [43, 49] employ fully relativistic pseudopotentials. We implement the iterative solution of the BTE in a magnetic field in PERTURBO, and use very fine, equal and uniform $\mathbf{k}$- and $\mathbf{q}$-point grids (with 140^3 points for Si, 650^3 for GaAs and 1800^2 for graphene) to converge the BTE solutions. The conductivity tensor is obtained via tetrahedron integration [43].

2.3 Results

Silicon

We compute the drift and Hall mobilities, Hall factor, and MR as a function of temperature for Si, and compare the computed results with experiments. Figure 2.1(a) shows the Hall and drift electron mobilities in n-type silicon. The agreement with experimental data from Refs. [12, 50–52] is excellent. As expected for electron carriers, the Hall mobility is greater than the drift mobility at all temperatures. The computed Hall factor, $r = \mu_{\mathrm{H}}/\mu_{\mathrm{d}}$, increases slightly with temperature, as evidenced by higher deviations between μ_{H} and μ_{d} for higher temperatures.

The Hall factor for electrons is shown in Fig. 2.1(b) at 300 K as a function of carrier concentration, which can be tuned in our calculations by changing the chemical potential. At low carrier density, our computed Hall factor is very close to the accepted value of $\sim$1.15 in n-type Si [7]. The computed Hall factor is within $\sim$10% of experiment at all carrier concentrations, a noteworthy result for a calculation without adjustable parameters. We attribute the increasing deviation from experiments at higher concentrations to scattering from ionized impurities not taken into account in this work.

The transverse MR is a common figure of merit for various applications. In Fig. 2.1(c), we plot the transverse MR as a function of magnetic field for electron carriers in n-type Si. The computed MR is in very good agreement with experiments from Ref. [8]. In the low field regime $\mu_{\mathrm{H}}\mathrm{B} \ll 1$ the calculations use a strict convergence threshold on the conductivity, with a change $\Delta\sigma/\sigma < 10^{-8}$ between consecutive iterations. Calculations at higher fields ($B > 2 \cdot 10^3$ G) require relaxing this convergence threshold to $\sim 10^{-4}$. Remaining differences between experiment and theory may be due to various factors, including uncertainty in the experimental temperature and doping concentration, as well as inevitable small deviations from experiment of the computed band structure and phonon dispersions.

Figure 2.1(d) shows the computed Hall and drift mobilities of hole carriers and compares them with experimental data for p-type silicon. The hole mobilities are in very good agreement with data for p-type Si [9, 11, 53]. For hole carriers, correctly, we obtain a behavior opposite to electrons, $\mu_{\mathrm{H}} < \mu_{\mathrm{d}}$ in the entire temperature range and thus a Hall factor $r < 1$. Our computed low field MR coefficient, MR/B^2, is $7.74 \cdot 10^5\ \mathrm{cm}^4/\mathrm{V}^2\mathrm{s}^2$ for holes at 300 K, within 30% of the measured value of $5.90 \cdot 10^5\ \mathrm{cm}^4/\mathrm{V}^2\mathrm{s}^2$ [54]. For hole carriers, we find that calculations without SOC fail to produce an isotropic conductivity tensor, a key sanity check

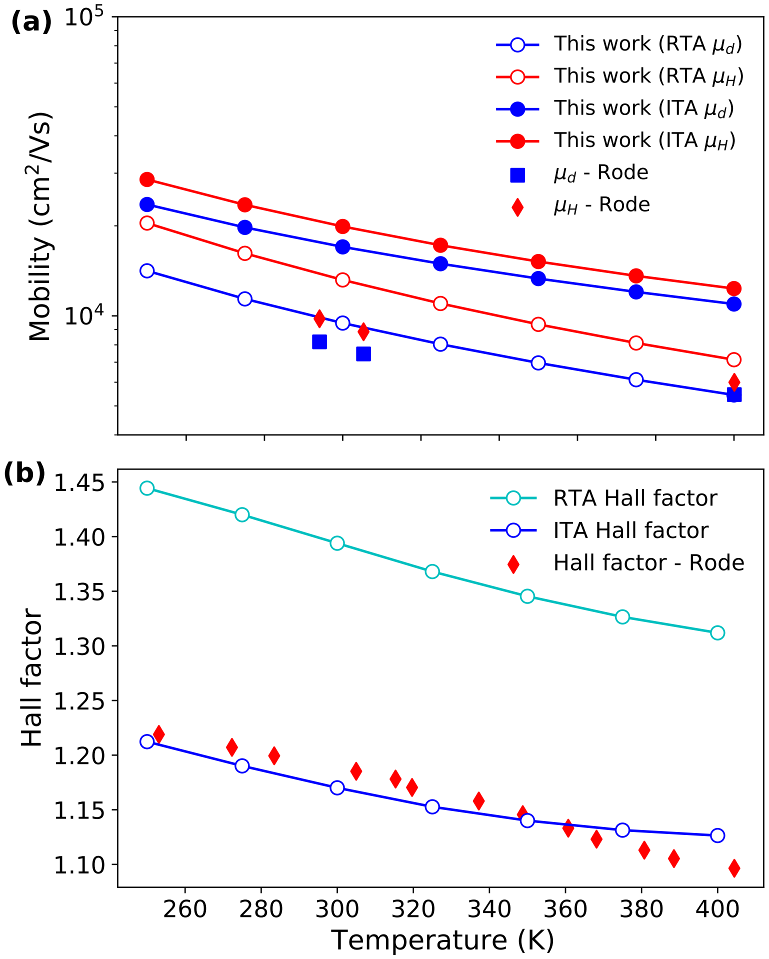

Figure 2.2: (a) Drift and Hall mobilities in GaAs as a function of temperature for an electron concentration $n = 10^{16}\,\mathrm{cm}^{-3}$. (b) Hall factor vs temperature for electrons in GaAs.

for Si(for electrons, SOC has only a minor effect). The spurious MR anisotropy for calculations without SOC is due to poor numerical convergence and greater errors in the conductivity tensor, providing further evidence that including SOC in our band structure and e-ph calculations [43, 49] is key to obtaining accurate magnetotransport for hole carriers. These results show that including SOC makes accurate magnetotransport calculations possible for hole carriers in semiconductors.

Gallium arsenide

The drift mobility has been studied extensively from first principles in GaAs [31, 34, 37]. Due to its polar character, electrons in GaAs couple strongly with longitudinal optical (LO) phonons through the Fröhlich interaction. We have recently shown that the iterative solution of the linearized BTE (ITA in short) overestimates the mobility and that including electron-two-phonon (e-2ph) scattering processes significantly improves the result; the RTA also gives a mobility in agreement with experiment [31], but due to compensation of errors [34]. We find that the same trends also hold for the Hall mobility. Figure 2.2(a) shows the drift and Hall mobilities for electrons in GaAs as a function of temperature. The experimental Hall mobility shown for comparison is obtained as μ_H = $\mu_\mathrm{d} r$ with values of μ_d and r from Ref. [13].

The ITA overestimates both the drift and Hall mobilities, by a factor of ∼2 at 300 K, while the RTA is in better agreement with experiments due to error compensation [34]. The Hall factor $r = \mu_\mathrm{H}/\mu_\mathrm{d}$ for both approaches is correctly greater than 1, but the Hall factor for ITA is much closer to the measured data [Fig. 2.2(b)]. Although each of the Hall and drift mobilities are overestimated in the ITA, their ratio is predicted accurately; we cannot establish whether this result is a coincidence or due to cancellation of effects from e-2ph processes in the ratio. Overall, these trends show that for polar semiconductors first-principles magnetotransport calculations have an accuracy similar to calculations without magnetic field.

Graphene

Similar to other semimetals [1], graphene exhibits a relatively large MR, with reported values of $20-50\%$ at room temperature and even greater at lower temperatures [17]. We discuss the MR in graphene for hole carriers but the MR values for electrons are similar. The accuracy of our settings is checked by calculating the drift mobility at 300 K; we obtain a value of $\sim 160000\ \mathrm{cm}^2/\mathrm{Vs}$ consistent with experiments in suspended graphene [55].

Figure 2.3(a) shows the computed MR in graphene at 300 K. We find that the MR depends strongly on carrier concentration—a doubling of concentration from ∼1.5 to $3 \cdot 10^{12}\,\mathrm{cm}^2/\mathrm{Vs}$ decreases the MR by an order of magnitude. This situation makes comparison with experiment difficult [Fig. 2.3(b)] as the reported carrier concentration usually does not take into account the Hall factor (we find $r = 1.45$ for $n = 1.2 \cdot 10^{12}$ cm^{-3}, consistent with recent work [41]). As by definition $n = r/(eR_\mathrm{H})$, carrier concentrations from Hall measurements are inaccurate unless the Hall factor is taken into account. In addition, most graphene samples are measured on substrates, often causing a reduction in the mobility. Accordingly, experimental values of the mobility and MR vary over a wide range [17, 18, 56]. This

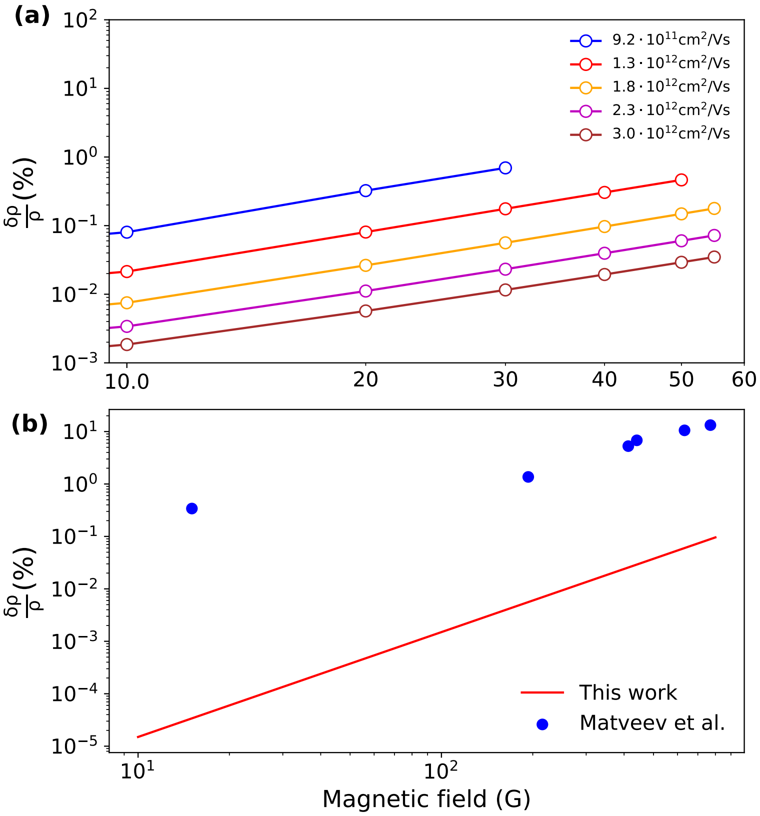

Figure 2.3: (a) Transverse MR in graphene vs magnetic field for various hole carrier concentrations at 300 K. (b) Comparison of the calculated MR for a hole concentration of $p = 2.46{\cdot}10^{13}$ cm^{-2} with experimental data for $p = (2.2{-}4.2){\cdot}10^{13}$ cm^{-2}, taken from Ref. [16].

variability in the experimental results can at least partially explain the discrepancy between the calculated and measured MR in Fig. 2.3(b).

Analysis of the electron occupations (see below) reveals that taking into account backscattering by iteratively solving the full BTE (as opposed to using the RTA) is essential in graphene, and that the RTA fails to capture the correct electronic occupations at steady state. This key role of backscattering in magnetotransport mimics trends found for thermal transport in graphene [57].

Steady-state occupations

To conclude our analysis, we study the electron occupations at steady state, focusing on their change due to the magnetic field for a constant electric field. We define this relative occupation change as $\delta f/f = [f_{n\mathbf{k}}(\mathbf{E},\mathbf{B}) - f_{n\mathbf{k}}(\mathbf{E},0)]/f_{n\mathbf{k}}(\mathbf{E},0)$, and plot it in momentum space for Si and graphene. In the results for Si, shown in Fig. 2.4(a), the occupation change projected on the k_z=0 plane clearly shows the

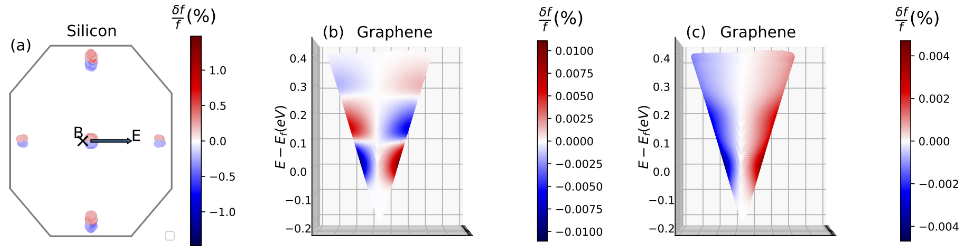

Figure 2.4: (a) Projection of the occupation changes $\delta f/f$ onto the $k_z = 0$ plane in Si. (b) Occupation change $\delta f/f$ in graphene near the Dirac cone with contributions from all phonons. (c) The same result as in (b) for graphene but with scattering from the highest-energy optical phonon branch excluded from the transport calculation.

effect of the Lorentz force, whereby the electrons deviate in the $\mathbf{E}\times\mathbf{B}$ direction near the six conduction band minima (the occupations at the zone center are projections of the two band minima along the k_z axis). As expected, the electrons are deflected in momentum space due to the magnetic field, an important sanity check for our numerical implementation.

The results for graphene, shown in Fig. 2.4(b), are more interesting. Similar to Si, the occupations near the Dirac cone are also changed by the Lorentz force. However, electrons in graphene couple strongly with LO phonons with momentum near Γ and TO phonons with momentum near K [58], which mediate intra- and inter-valley electronic processes respectively. As a result, optical phonon absorption generates a step-like pattern in the occupation changes, with $160-200$ meV spacing equal to the LO and TO phonon energies [58]. The disappearance of the alternating patches on removing scattering from the highest optical branch from the transport calculation [Fig. 2.4(c)] provides concrete evidence for the dominant optical phonon backscattering in graphene. The RTA completely misses this trend and gives occupation changes with a pattern similar to Fig. 2.4(c). While in graphene the magnetotransport RTA results are in fairly good agreement with the full solution of the BTE, which correctly includes backscattering, our results show that the RTA fails to capture important features of magnetotransport in graphene.

2.4 Conclusion

We have shown calculations of magnetotransport that can accurately predict the Hall mobility, Hall factor, and MR in Si and GaAs. Our results for graphene leave room for improvements and call for stricter protocols for magnetotransport measurements in 2D materials. Analysis of the steady state occupations in graphene highlights a key strength of first-principles calculations—they can capture the competition between mode-dependent e-ph scattering and the effect of the Lorentz force in momentum space, shedding light on the microscopic mechanisms governing magnetotransport. With calculations on materials with tens of atoms in the unit cell readily available [43], extension of these results to other semiconductors and 2D materials appears straightforward. The current formalism can be easily extended to include the Berry curvature, for example to study magnetotransport in topological semimetals and shed light on the origin of their unconventional MR. Our method is general and can be applied to a wide range of materials, including semimetals such as bismuth and graphite with large MR and topological semimetals with strong SOC and unconventional magnetotransport. As our approach allows us to calculate the full resistivity tensor, it will be interesting to apply it in the future to interpret experimental angular MR diagrams. The magnetotransport calculations shown in this work will be made available in our PERTURBO code, thus greatly expanding the reach of first-principles transport studies and connecting them more deeply with transport experiments, which are often carried out in magnetic fields.

References

[1] J. M. Ziman, *Electrons and Phonons: the Theory of Transport Phenomena in Solids* (Oxford University Press, Oxford, 2001) p. 483.

[2] A. B. Pippard, *Magnetoresistance in Metals*, Vol. 2 (Cambridge University Press, Cambridge, 1989).

[3] S. Parkin, Annu. Rev. Mater. Sci. **25**, 357 (1995).

[4] A. Ramirez, J. Phys. Condens. Matter **9**, 8171 (1997).

[5] J. E. Lenz, Proc. IEEE **78**, 973 (1990).

[6] J. M. Daughton, J. Magn. Magn. Mater. **192**, 334 (1999).

[7] I. G. Kirnas, P. M. Kurilo, P. G. Litovchenko, V. S. Lutsyak, and V. M. Nitsovich, Phys. Status Solidi (a) **23**, K123 (1974).

[8] N. A. Porter and C. H. Marrows, J. Appl. Phys. **109**, 07C703 (2011).

[9] F. J. Morin and J. P. Maita, Phys. Rev. **96**, 28 (1954).

[10] W. E. Krag, Phys. Rev. **118**, 435 (1960).

[11] P. P. Debye and T. Kohane, Phys. Rev. **94**, 724 (1954).

[12] E. H. Putley and W. H. Mitchell, Proc. Phys. Soc. **72**, 193 (1958).

[13] D. L. Rode, *Semiconductors and Semimetals* (Academic Press, New York, 1975).

[14] G. Stillman, C. Wolfe, and J. Dimmock, J. Phys. Chem. Solids **31**, 1199 (1970).

[15] J. S. Blakemore, J. Appl. Phys. **53**, R123 (1982).

[16] V. Matveev, V. Levashov, O. Kononenko, and V. Volkov, Scr. Mater. **147**, 37 (2018).

[17] K. Gopinadhan, Y. J. Shin, I. Yudhistira, J. Niu, and H. Yang, Phys. Rev. B **88**, 195429 (2013).

[18] W. J. Wang, K. H. Gao, Z. Q. Li, T. Lin, J. Li, C. Yu, and Z. H. Feng, Appl. Phys. Lett. **105**, 182102 (2014).

[19] M. N. Ali, J. Xiong, S. Flynn, J. Tao, Q. D. Gibson, L. M. Schoop, T. Liang, N. Haldolaarachchige, M. Hirschberger, N. P. Ong, and R. J. Cava, Nature **514**, 205 (2014).

[20] J. Xiong, S. K. Kushwaha, T. Liang, J. W. Krizan, M. Hirschberger, W. Wang, R. J. Cava, and N. P. Ong, Science **350**, 413 (2015).

[21] C.-Z. Li, L.-X. Wang, H. Liu, J. Wang, Z.-M. Liao, and D.-P. Yu, Nat. Commun. **6**, 10137 (2015).

[22] N. P. Armitage, E. J. Mele, and A. Vishwanath, Rev. Mod. Phys. **90**, 015001 (2018).

[23] J.-P. Jan, in *Solid State Physics*, Vol. 5 (Elsevier, 1957) pp. 1–96.

[24] J. Lin, S. Li, L. Linares, and K. Teng, Solid State Electron. **24**, 827 (1981).

[25] L. Reggiani, D. Waechter, and S. Zukotynski, Phys. Rev. B **28**, 3550 (1983).

[26] B. Lewis and E. Sondheimer, Proc. R. Soc. A **227**, 241 (1955).

[27] F. Szmulowicz, Phys. Rev. B **28**, 5943 (1983).

[28] F. Szmulowicz and F. L. Madarasz, Phys. Rev. B **27**, 2605 (1983).

[29] R. M. Martin, *Electronic Structure: Basic Theory and Practical Methods* (Cambridge University Press, 2004).

[30] S. Baroni, S. de Gironcoli, A. Dal Corso, and P. Giannozzi, Rev. Mod. Phys. **73**, 515 (2001).

[31] J.-J. Zhou and M. Bernardi, Phys. Rev. B **94**, 201201(R) (2016).

[32] V. A. Jhalani, J.-J. Zhou, and M. Bernardi, Nano Lett. **17**, 5012 (2017).

[33] N.-E. Lee, J.-J. Zhou, L. A. Agapito, and M. Bernardi, Phys. Rev. B **97**, 115203 (2018).

[34] N.-E. Lee, J.-J. Zhou, H.-Y. Chen, and M. Bernardi, Nat. Commun. **11**, 1607 (2020).

[35] J. Park, J.-J. Zhou, V. A. Jhalani, C. E. Dreyer, and M. Bernardi, Phys. Rev. B **102**, 125203 (2020).

[36] W. Li, Phys. Rev. B **92**, 075405 (2015).

[37] T.-H. Liu, J. Zhou, B. Liao, D. J. Singh, and G. Chen, Phys. Rev. B **95**, 075206 (2017).

[38] J. Ma, A. S. Nissimagoudar, and W. Li, Phys. Rev. B **97**, 045201 (2018).

[39] T. Sohier, D. Campi, N. Marzari, and M. Gibertini, Phys. Rev. Mater. **2**, 114010 (2018).

[40] F. Macheda and N. Bonini, Phys. Rev. B **98**, 201201 (2018).

[41] F. Macheda, S. Poncé, F. Giustino, and N. Bonini, Nano Lett. **20**, 8861 (2020).

[42] S. Zhang, Q. Wu, Y. Liu, and O. V. Yazyev, Phys. Rev. B **99**, 035142 (2019).

[43] J.-J. Zhou, J. Park, I.-T. Lu, I. Maliyov, X. Tong, and M. Bernardi, Comput. Phys. Commun. **264**, 107970 (2021).

[44] A. A. Mostofi, J. R. Yates, Y.-S. Lee, I. Souza, D. Vanderbilt, and N. Marzari, Comput. Phys. Commun. **178**, 685 (2008).

[45] W. Jones and N. March, *Theoretical Solid State Physics* (Wiley, London, 1973).

[46] S. M. Sze and K. K. Ng, *Physics of Semiconductor Devices* (John Wiley and Sons, Hoboken NJ, 2006).

[47] P. Giannozzi, S. Baroni, N. Bonini, M. Calandra, R. Car, C. Cavazzoni, D. Ceresoli, G. L. Chiarotti, M. Cococcioni, I. Dabo, A. D. Corso, S. de Gironcoli, S. Fabris, G. Fratesi, R. Gebauer, U. Gerstmann, C. Gougoussis, A. Kokalj, M. Lazzeri, L. Martin-Samos, N. Marzari, F. Mauri, R. Mazzarello, S. Paolini, A. Pasquarello, L. Paulatto, C. Sbraccia, S. Scandolo, G. Sclauzero, A. P. Seitsonen, A. Smogunov, P. Umari, and R. M. Wentzcovitch, J. Phys. Condens. Matter **21**, 395502 (2009).

[48] A. A. Mostofi, J. R. Yates, G. Pizzi, Y.-S. Lee, I. Souza, D. Vanderbilt, and N. Marzari, Comput. Phys. Commun. **185**, 2309 (2014).

[49] J. Park, J.-J. Zhou, and M. Bernardi, Phys. Rev. B **101**, 045202 (2020).

[50] C. Jacoboni, C. Canali, G. Ottaviani, and A. A. Quaranta, Solid State Electron. **20**, 77 (1977).

[51] R. A. Logan and A. J. Peters, J. Appl. Phys. **31**, 122 (1960).

[52] P. Norton, T. Braggins, and H. Levinstein, Phys. Rev. B **8**, 5632 (1973).

[53] J. Dorkel and P. Leturcq, Solid State Electron. **24**, 821 (1981).

[54] Phys. Rev. **109**, 1098 (1958).

[55] K. Bolotin, K. Sikes, Z. Jiang, M. Klima, G. Fudenberg, J. Hone, P. Kim, and H. Stormer, Solid State Commun. **146**, 351 (2008).

[56] M. Rein, N. Richter, K. Parvez, X. Feng, H. Sachdev, M. Kläui, and K. Müllen, ACS Nano **9**, 1360 (2015).

[57] G. Fugallo, A. Cepellotti, L. Paulatto, M. Lazzeri, N. Marzari, and F. Mauri, Nano Lett. **14**, 6109 (2014).

[58] X. Tong and M. Bernardi, Phys. Rev. Res. **3**, 023072 (2021).

Chapter 3

DOMINANT TWO-DIMENSIONAL ELECTRON-PHONON INTERACTIONS IN THE BULK DIRAC SEMIMETAL $\mathrm{Na_3Bi}$

This chapter is a slightly modified version of the manuscript: D. C. Desai*, J. Park*, J.-J. Zhou, and M. Bernardi, "Dominant two-dimensional electron–phonon interactions in the Bulk Dirac semimetal $\mathrm{Na_3Bi}$", *Nano Lett.*, 23, 9, 3947–3953 (2023). D.C.D participated in the conception of the project, performed calculations, analyzed the data, and participated in the writing of the manuscript.
* These authors contributed equally.

3.1 Introduction

Topological semimetals are characterized by electronic band crossings near the Fermi energy, which result in linear band dispersions and topologically nontrivial band structures [1]. There is a vast literature on their unusual properties, including high mobility and magnetoresistance [2–8], anomalous transport regimes [8–10], surface Fermi arcs [11–14], and topological phase transitions [15, 16]. The discovery of graphene—a two-dimensional Dirac semimetal (DSM)—has enabled studies of new physics in a carbon atom sheet [17]. In contrast with graphene, three-dimensional (bulk) DSMs are materials with rich structural and chemical complexity. They present a wide range of possible crystal structures and arrangements of Dirac cones, whose degeneracy is protected by crystal symmetry [1], which makes bulk DSMs interesting for device applications [18, 19].

Although many properties of DSMs can be explained using model low-energy Hamiltonians, the interactions between electrons and other degrees of freedom—such as phonons, photons, and spin—are not simple to quantify and give rise to rich physics in DSMs. Examples include phonon nonlinearities, unconventional nonequilibrium dynamics, and topological phase transitions, [20–24] etc. Electron-phonon (e-ph) interactions play a central role in this physics, but their understanding in bulk DSMs—and more generally in topological semimetals—is rather limited and relies mainly on phenomenological models [25, 26]. First-principles calculations of e-ph interactions, which have now been applied to many classes of materials [27–38], have been hindered in bulk DSMs by their complex atomic and electronic structures.

Sodium bismuthate ($\mathrm{Na_3Bi}$) is a prototypical bulk DSM [11, 39] whose Dirac cones have been observed by scanning tunneling spectroscopy [16, 40–42], angle-resolved photoemission (ARPES) [12, 39], and transport measurements [8]. In Na_3Bi, first-principles calculations have examined impurity-limited transport [43], nonequilibrium dynamics [44], and spin-orbit coupling [45]. However, a quantitative analysis of e-ph interactions is still missing. The interplay between crystal symmetry and electron spin, orbital, and momentum degrees of freedom suggests that $\mathrm{Na_3Bi}$ and other bulk DSMs may host unconventional e-ph interactions yet to be discovered. We explore this direction by carrying out a detailed first-principles study of e-ph interactions in Na_3Bi. We use density functional theory (DFT) [46, 47] to obtain the electronic structure, lattice vibrations, and their interactions; our calculations take into account spin-orbit coupling (SOC) and many-body corrections to the electronic band structure (with the GW method [48]), and employ an improved treatment of acoustic phonons (see section 3.3).

Leveraging these accurate tools, we discover a dominant two-dimensional (2D) e-ph interaction in Na_3Bi associated with a 2D optical phonon with e-ph coupling strength far greater than that of any other mode. Our analysis shows that this 2D e-ph interaction governs the scattering and transport of Dirac electrons, and reveals its microscopic origin. Similar “killer” phonon modes with dominant e-ph coupling controlling charge transport have been found in organic crystals [49] but not in topological materials. We also find that the strongly-coupled 2D mode breaks inversion symmetry in Na_3Bi and induces a dynamical phase transition to a Weyl semimetal (WSM). This finding points to new opportunities for ultrafast control of topological materials [20–24, 44].

3.2 Results

The unit cell of Na_3Bi, shown in Fig. 3.1(a), belongs to the hexagonal $P6_3/mmc$ space group. Its crystal structure alternates a layer of Bi plus Na atoms, labeled Na(1), and two layers made up only by Na atoms, labeled Na(2). Inversion and C_3 rotational symmetry result in a 4-fold band degeneracy near the Fermi energy, with contributions from Na $3s$ and Bi $6p$ orbitals [11, 42, 50–52]. The Dirac cone consists of two electronic bands, one with Na $3s$+Bi $6p_z$ and the other with Bi $6p_x+6p_y$ orbital character (the latter is denoted below as Bi-p_{xy} band). To determine an accurate band structure, we start from DFT and then apply a one-shot GW correction (see section 3.3), which increases the Fermi velocity of the Na $3s+$Bi $6p_z$ band by a factor of 1.8 and reduces the Fermi velocity of the Bi p_{xy}-band relative to DFT (Fig. 3.1(b),(c)). The Fermi velocity computed with GW $\sim$300 meV above the

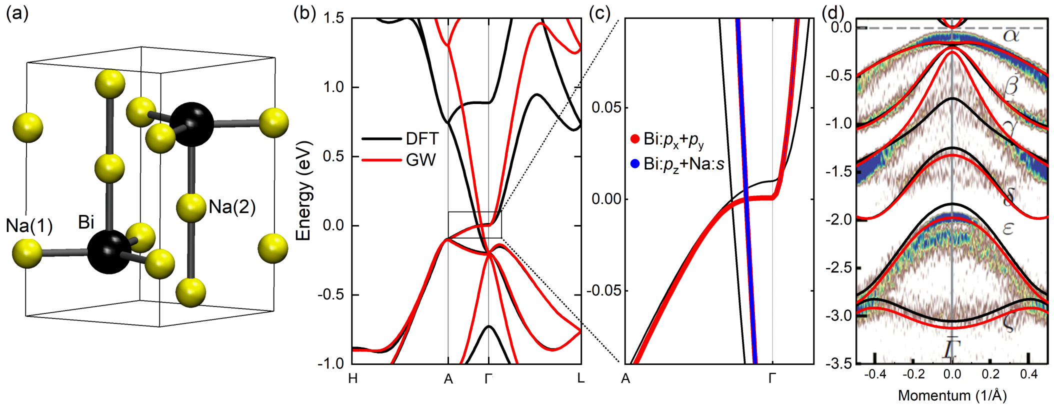

Figure 3.1: (a) Crystal structure of Na_3Bi with $P6_3/mmc$ space-group symmetry. The Bi (Na) atoms are shown with black (yellow) spheres. (b) Band structure of Na_3Bi comparing DFT (black) and GW (red) results. (c) Zoom-in of the band structure in (b) near the Dirac point, with states color-coded according to their orbital character. (d) Comparison of DFT and GW band structures with ARPES experimental data [12], shown along the M−Γ−M direction. The computed band structure was shifted by $k_z = 0.02$ Å^{-1} to compare with experiments [12].

Dirac node is 7.0×10^5 ms^{-1}, in excellent agreement with the experimental value of 8.1×10^5 ms^{-1} [9]. Our computed GW band structure agrees well with ARPES measurements by Liang et al. [12] (Fig. 3.1(d)).

The computed phonon dispersion in Na_3Bi is shown in Fig. 3.2(a). The phonon frequencies are positive for all modes (color-coded curves in Fig. 3.2(a)), indicating a dynamically stable $P6_3/mmc$ crystal structure with no soft modes or imaginary frequencies. Fine-tuning the acoustic sum rule is crucial to obtaining this well-behaved phonon dispersion. Our results employ an advanced acoustic sum rule which minimally affects the inter-atomic force constants from DFPT [53]; conversely, a widely-used—so-called "simple" —acoustic sum rule [54], which modifies the inter-atomic force constants to enforce translational symmetry, leads to spurious soft phonons near the K-point of the Brillouin zone [55] (gray curves in Fig. 3.2(a)). While previous work predicted the existence of a more stable $P\bar{3}c1$ phase at low temperature (< 46 K) [55], our study shows that the $P6_3/mmc$ structure is dynamically stable, and focuses on a temperature range (> 100 K) where the $P6_3/mmc$ crystal structure is the most stable [55].

Our settings, which combine a stable crystal structure, well-defined phonon dispersions, and electronic states with an accurate Fermi velocity, allow us to carry out reliable first-principles calculations of e-ph scattering and transport in Na_3Bi [31].

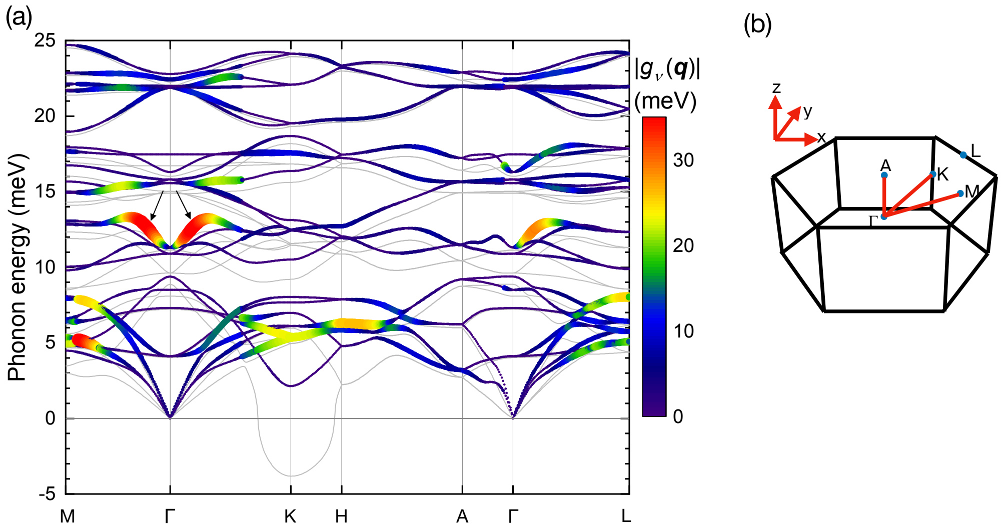

Figure 3.2: (a) Na_3Bi phonon dispersion overlaid with a color map of the e-ph coupling strength, $|g_\nu(\mathbf{q})|$, for wave-vector $\mathbf{q}$ along high-symmetry lines. The marker size is proportional to $|g_\nu(\mathbf{q})|$ and the arrows indicate the strongly-coupled 2D phonon mode. The phonon dispersion obtained with the simple acoustic sum rule is shown for comparison using gray lines, with imaginary frequencies shown as negative values. (b) Brillouin zone of Na_3Bi, shown to aid the interpretation of panel (a). The $\Gamma - M$ and $\Gamma - K$ directions are in the x-y plane, and $\Gamma - A$ corresponds to the z-direction.

We compute the e-ph matrix elements $g_{mn\nu}(\mathbf{k}, \mathbf{q})$, which encode the e-ph coupling between pairs of electronic states (initial state $|n\mathbf{k}\rangle$ and final state $|m\mathbf{k} + \mathbf{q}\rangle$, where n and m are band indices and $\mathbf{k}$ the electron crystal momentum) due to a phonon with mode index ν and wave-vector $\mathbf{q}$. These calculations are carried out with the PERTURBO code [56] as described in section 3.3.

Figure 3.2 shows the phonon dispersion in Na_3Bi overlaid with a color map of the e-ph coupling strength, defined as $|g_\nu(\mathbf{q})| \equiv (\sum_{mn} |g_{mn\nu}(\mathbf{k} = 0, \mathbf{q})|^2 / N_b)^{1/2}$ (here we sum over $N_b = 2$ lowest conduction bands) [56]. We find that the e-ph interactions are overall relatively weak in Na_3Bi, with an average value $|g_\nu(\mathbf{q})| \approx$ 5 meV. Yet one particular phonon mode, with ∼12 meV energy and wave-vector $\mathbf{q}$ in the Γ−M and Γ−K directions (which correspond to the crystal x-y plane; see Fig. 3.2(b)) exhibits a much stronger e-ph coupling than any other mode, with value $|g_\nu(\mathbf{q})| \approx 35$ meV. This strongly-coupled 2D mode is a longitudinal optical (LO) phonon that is infrared-active and has E_{1u} character at the zone center [57]. Its associated atomic vibrations, shown in Fig. 3.3(a), have primary contributions from

Na(2) atoms, which oscillate with large amplitudes in the Na-only layers of Na_3Bi, and have negligible contributions from the Na(1) and Bi atoms in the neighboring layers. Because the wave-vector and atomic displacements of this strongly-coupled 2D mode are both in the x-y plane, the dominant e-ph interactions in Na_3Bi are inherently two-dimensional.

To understand the microscopic origin these strong 2D e-ph interactions, we analyze their perturbation potential, whose local lattice-periodic part can be written as [47, 56]

$$\Delta V_{\nu\mathbf{q}}(\mathbf{r}) \equiv \sum_{\kappa} \frac{1}{\sqrt{M_\kappa}} \mathbf{e}^{(\kappa)}_{\nu\mathbf{q}} \cdot \partial_{\kappa,\mathbf{q}} V(\mathbf{r}) \ , \tag{3.1}$$

where M_κ is the mass and $\mathbf{e}^{(\kappa)}_{\nu\mathbf{q}}$ the displacement eigenvector of atom κ due to phonon mode $(\nu, \mathbf{q})$, and $\partial_{\kappa,\mathbf{q}} V(\mathbf{r})$ is the derivative of the local Kohn-Sham potential with respect to the position of atom κ [56]. We focus on the effect of the dominant Na(2) atomic vibrations on the Bi-p_{xy} Dirac-cone electronic states near Γ. Figure 3.3 shows the e-ph perturbation potential $\Delta V_{\nu\mathbf{q}}(\mathbf{r})$ generated by Na(2) atomic vibrations and plotted in the x-y plane containing Bi atoms. For the dominant 2D LO mode (Fig. 3.3(a)), which has wave-vector $\mathbf{q}$ in the x-y plane, the Na(2) atoms move out-of-phase within each layer, causing large perturbations at the Bi atoms. As a result electronic states in the Bi p_{xy}-band couple strongly with this phonon mode. Increasing $|\mathbf{q}|$ in the x-y plane leads to an even greater perturbation at the Bi site and thus stronger e-ph coupling. In contrast, for a 2D transverse optical mode propagating in the z-direction the Na(2) atoms move uniformly in-phase in the x-y plane (Fig. 3.3(b)). In this case, $\Delta V_{\nu\mathbf{q}}(\mathbf{r})$ has a symmetric pattern with nodes at Bi atoms, which suppresses e-ph coupling for the Bi-p_{xy} band. Accordingly, we find a very weak e-ph coupling for such transverse optical modes, as shown by the dark blue color in the Γ−A direction in Fig. 3.2(a).

We analyze two important consequences of the strong 2D e-ph coupling in Na_3Bi. First, we find that charge transport is governed by scattering of Dirac electrons with the strongly-coupled 2D mode, which contributes nearly half of the total e-ph scattering rate (Fig. 3.4(a)) and resistivity (see below). Other individual phonon modes contribute significantly less, up to 15% of the e-ph scattering rate for the mode with the second strongest coupling. Therefore, this strongly-coupled 2D LO mode is analogous to the "killer" phonons controlling charge transport recently discovered in organic crystals [49].

Because of the strong 2D e-ph coupling, Dirac-cone electronic states with in-plane momentum $\mathbf{k}$, which couple to each other via phonons with in-plane momenta,

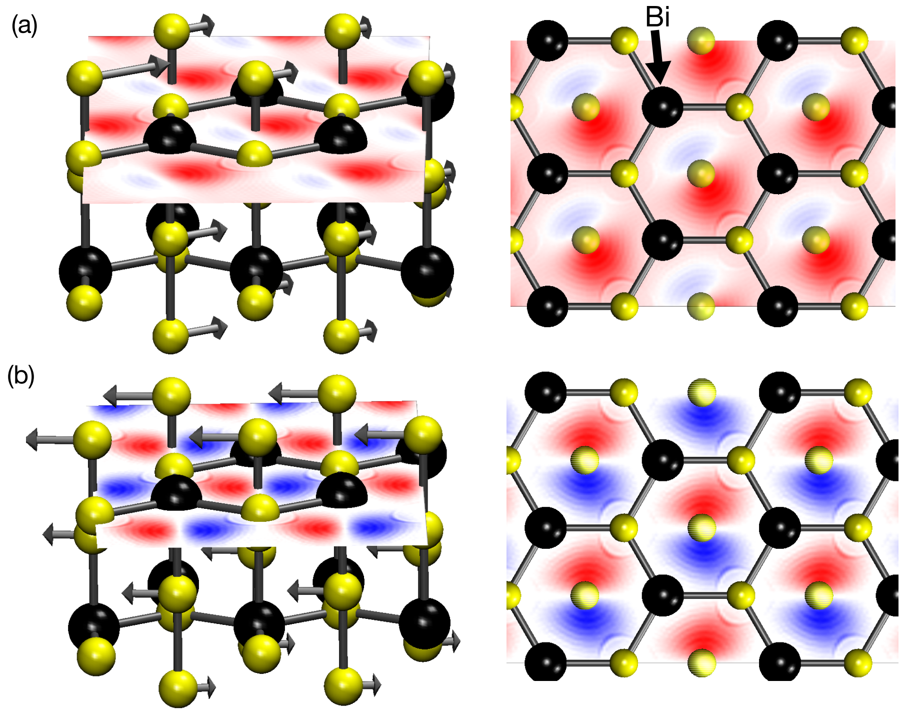

Figure 3.3: Side view (left) and top view (right) of atomic motions and e-ph perturbation potentials $\Delta V_{\nu\mathbf{q}}(\mathbf{r})$ for two phonon modes: (a) Strongly-coupled 2D longitudinal optical phonon with wave-vector $\mathbf{q}$=(1/6,0,0) in the x-y plane, associated with a large perturbation at the Bi site leading to strong e-ph interactions; (b) transverse optical mode with $\mathbf{q}$ = (0,0,1/8) along the z-axis, resulting in a negligible e-ph coupling due to the weak perturbation at the Bi site. In both cases, we compute $\Delta V_{\nu\mathbf{q}}(\mathbf{r})$ from Na(2) atomic vibrations and plot it in the x-y plane containing Bi and Na(1) atoms. Red and blue colors correspond to positive and negative values of $\Delta V_{\nu\mathbf{q}}(\mathbf{r})$, respectively.

exhibit large e-ph scattering rates (Fig. 3.4(b)). In contrast, electrons with momentum $\mathbf{k}$ in the z-direction scatter mostly via phonons with out-of-plane $\mathbf{q}$, and are associated with smaller scattering rates. This anisotropic scattering due to 2D e-ph coupling is evident in the entire temperature range we analyzed (77−300 K). We have verified that the e-ph matrix elements $g(\mathbf{k},\mathbf{q})$ possess a similar anisotropy, such that the e-ph coupling strength $|g(\mathbf{k},\mathbf{q})|$ is much greater for in-plane than for out-of-plane electron momenta.

We compute the phonon-limited mobility and resistivity using these first-principles e-ph scattering rates in the Boltzmann transport equation [56] (see section 3.3). Our results show that the in-plane mobility for temperatures between 150−400 K is very large (Fig. 3.4(c))−up to $\sim$30,000 cm^2/Vs at room temperature and high electron concentration, mainly as a result of the high Fermi velocity of the Bi p_{xy}-band and the overall weak e-ph coupling. This mobility limit, which applies to an ideally pure crystal of $\mathrm{Na_3Bi}$ where charge transport is impeded only by phonons, is exceptionally high and has the same order of magnitude as the mobility in graphene [17]. To our knowledge, such large electron mobilities have not yet been measured in $\mathrm{Na_3Bi}$ near room temperature; one possible reason is that $\mathrm{Na_3Bi}$ samples typically contain large concentrations of defects, particularly Na vacancies, which may make the intrinsic phonon-limited mobility difficult to observe [40, 41]. Improvements in growth techniques may bring the experimental mobility of $\mathrm{Na_3Bi}$ closer to our predicted theoretical limit. Note that in $\mathrm{Cd_3As_2}$, a widely studied DSM, mobility values as high as $\sim$40,000 $\mathrm{cm^2/Vs}$ at 130 K have been reported [58], which are comparable to the $\sim$100,000 $\mathrm{cm^2/Vs}$ we predict in $\mathrm{Na_3Bi}$ for the same temperature and carrier concentration.

To complete our discussion on transport, Fig. 3.4(d) shows the computed in-plane resistivity as a function of temperature for Fermi energies between $100-300$ meV. In this regime, the transport behavior is metallic, and the resistivity increases with temperature following a power law. Comparison with experiments is important despite the variability in $\mathrm{Na_3Bi}$ sample quality noted above. We compare our calculations with the measurements by Xiong *et al.* [9], which achieve the lowest resistivity among available experimental data [9, 40] indicating higher sample quality. Our computed resistivity is lower than their measured values [9] by about an order of magnitude at 50 K and a factor of $3-5$ at 250 K. The lower discrepancy at higher temperature indicates an improved agreement between theory and experiment in the intrinsic, phonon-limited transport regime studied in this work.

It is interesting to compare these findings with graphene, a 2D DSM. In both $\mathrm{Na_3Bi}$ and graphene, a 2D optical phonon has the strongest e-ph coupling [59, 60]. However, heavier atoms and weaker bonding in $\mathrm{Na_3Bi}$ result in softer phonons$-$the energy of the strongly-coupled 2D phonon in $\mathrm{Na_3Bi}$ is only $\sim$12 meV, and thus much smaller than the $\sim$200 meV energy of strongly-coupled 2D optical phonons in graphene [60]. At room temperature, where $k_\mathrm{B}T \approx 26$ meV, the strongly-coupled 2D phonons are thermally excited in $\mathrm{Na_3Bi}$, while in graphene only acoustic phonons are present. As a result, optical modes contribute less than 15% to the resistivity in graphene at 300 K [61], versus a dominant 50% resistivity contribution from the strongly-coupled 2D phonon in $\mathrm{Na_3Bi}$ (Fig. 3.4(d)). Note that while graphene is a 2D material, $\mathrm{Na_3Bi}$ is a bulk crystal where a dominant 2D e-ph interaction is

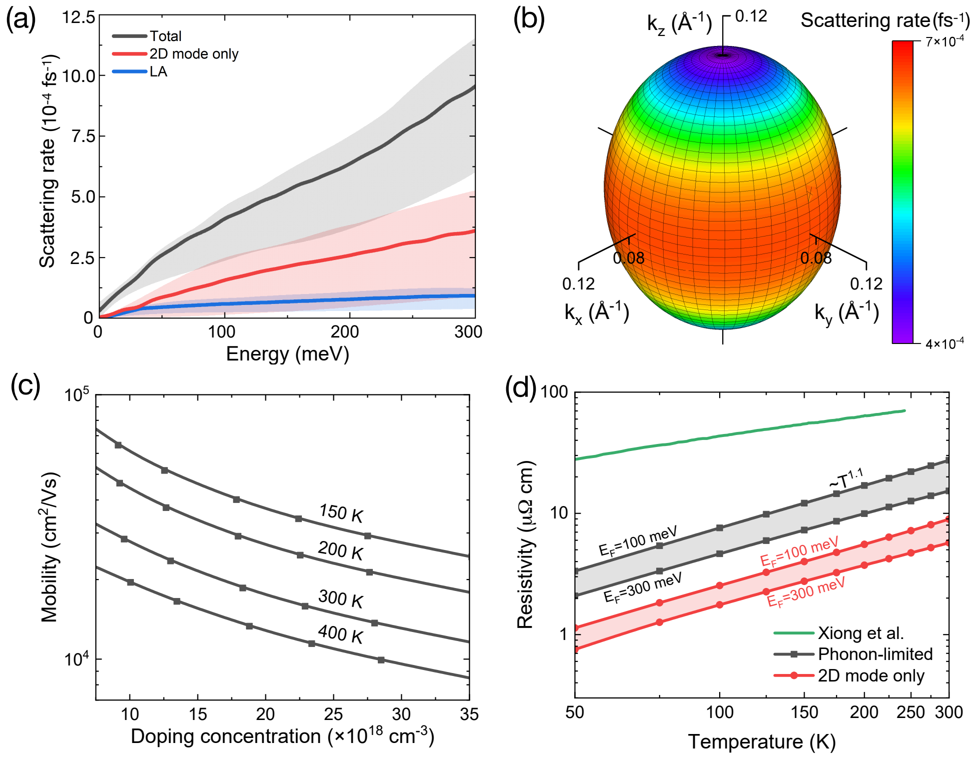

Figure 3.4: Calculations of transport and e-ph scattering in Na$_3$Bi. (a) E-ph scattering rates as a function of carrier energy at 300 K and E_{F}=200 meV. We show the total scattering rate (black) and the contributions from the strongly-coupled 2D mode (red) and the longitudinal acoustic (LA) mode with second strongest coupling (blue). For each curve, we plot the average scattering rate with a solid line, and show the standard deviation as a shaded region. (b) Fermi surface at E_{F}=200 meV color-coded according to the total e-ph scattering rates. (c) Electron mobility as a function of carrier concentration for temperatures between 150−400 K. (d) Temperature dependent resistivity for Fermi energies between 100−300 meV above the Dirac point, shown together with the strongly-coupled 2D-mode contribution. Experimental results by Xiong et al. [9] are shown for comparison.

unexpected.

Finally, we find that the atomic vibrations from the strongly-coupled 2D mode dynamically induce a phase transition to a WSM in Na$_3$Bi. Due to its E_{1u} character [57], this 2D mode dynamically breaks inversion symmetry and removes the four-fold degeneracy at the Dirac point, splitting each Dirac cone into a pair of Weyl cones. Figure 3.5 shows the DFT band structure in the k_x-k_y plane containing the Dirac node, comparing results for the pristine structure (Fig. 3.5(a)) and for the lattice distorted from the strongly-coupled 2D mode (Fig. 3.5(b)), which is computed with frozen-in atomic displacements along the 2D-mode eigenvector (see section 3.3).

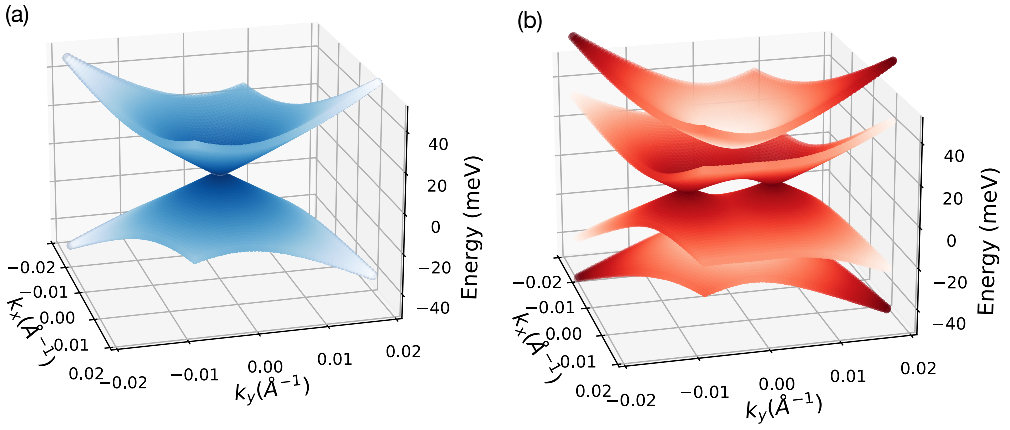

Figure 3.5: Electronic band structure computed with DFT for (a) pristine and (b) 2D-mode distorted Na_3Bi. The displacement in (b) is 3% of the in-plane lattice constant.

The atomic displacements split each Dirac node into a pair of Weyl nodes separated along k_y by about 0.01 $\AA^{-1}$; the system remains metallic throughout this phase transition. The Dirac degeneracy is lifted by breaking the threefold rotational symmetry. Additionally, inversion symmetry breaking from the strongly-coupled E_{1u} mode is crucial to obtaining the WSM phase. Therefore, phonon distortions that preserve inversion symmetry but break the threefold rotational symmetry − for example, E_{2g} modes, which are however weakly coupled − are not robust against a gap opening, and instead cause a phase transition to a topological insulator.

These results imply that 2D phonons with strong e-ph coupling can provide a versatile knob for ultrafast control in Na_3Bi. In particular, because the strongly-coupled 2D LO mode is infrared active [62] (but not Raman active), one could induce a topological phase transition in Na_3Bi by coherently driving this 2D mode using a THz pulse [63] or through carrier optical excitation followed by strong e-ph coupling [63]. Interestingly, Hübener et al. [44] have shown that a similar phase transition from a DSM to a WSM can be achieved in Na_3Bi with a different mechanism−strong light-matter coupling, which dresses the electronic states inducing Floquet-Weyl nodes. These predictions contribute to the thriving area of driven nonequilibrium dynamics in topological materials, where recent experiments on bulk DSMs [22] and WSMs [20, 21] have demonstrated nonequilibium topological phase transition using electric fields or optical pulses.

In conclusion, we have shown that the dominant e-ph interactions in a prototypical bulk DSM, Na_3Bi, are inherently two-dimensional and govern the scattering and transport of Dirac electrons. Our first-principles analysis reveals the microscopic origin of this strong 2D e-ph coupling; it also shows that the strongly-coupled 2D mode can induce a dynamical phase transition to a WSM, suggesting new routes for ultrafast control of Dirac electrons in bulk DSMs. These results seed the question of whether other bulk materials may host dominant low-dimensional e-ph interactions governing their physical properties. For example, MgB_2, a superconductor with a relatively high critical temperature of ∼40 K, has a crystal structure similar to Na_3Bi and has been hypothesized to host a 2D phonon with strong e-ph coupling [64, 65]. First-principles calculations such as those shown in this work can contribute to address these questions and advance future discoveries of electronic interactions and nonequilibrium dynamics in topological materials.

3.3 Methods

DFT, DFPT, and GW calculations

We perform DFT calculations in a plane-wave basis set using the QUANTUM ESPRESSO [54] code. We employ the PBEsol [66] exchange-correlation functional and fully-relativistic norm-conserving pseudopotentials from Pseudo Dojo [67]. These calculations use a coarse $12 \times 12 \times 8$ $\mathbf{k}$-point grid, a kinetic energy cutoff of 90 Ry, and relaxed lattice constants ($a = 5.42$ Å and $c = 9.67$ Å) which are in excellent agreement with the experimental values ($a = 5.45$ Å and $c = 9.66$ Å) [11]. The phonon dispersions and perturbation potentials are computed using coarse grids with $6 \times 6 \times 8$ $\mathbf{q}$-points using DFPT [47]. We employ the crystal acoustic sum rule from Ref. [53] to compute phonon dispersions. The GW correction to the electronic band structure is computed using the YAMBO code. [68] We employ 120 unoccupied bands and a 10 Ry energy cutoff for the dielectric screening combined with the Bruneval-Gonze terminator [69]; we have verified that increasing the number of unoccupied bands to 600 and the energy cutoff to 30 Ry has a negligible effect.

Electron-phonon matrix elements and perturbation potentials

Using electronic wave functions from DFT, together with phonon and e-ph perturbation potentials from DFPT, we obtain the e-ph coupling matrix elements on the coarse $\mathbf{k}$- and $\mathbf{q}$-point grids given above using the PERTURBO code. The e-ph matrix elements $g_{mn\nu}(\mathbf{k},\mathbf{q})$ are defined as

$$g_{mn\nu}(\mathbf{k},\mathbf{q}) = \sqrt{\frac{\hbar}{2\omega_{\nu\mathbf{q}}}} \langle\psi_{m\mathbf{k}+\mathbf{q}}| \, \Delta V_{\nu\mathbf{q}} \, |\psi_{n\mathbf{k}}\rangle \, , \tag{3.2}$$

where $|\psi_{n\mathbf{k}}\rangle$ and $|\psi_{m\mathbf{k}+\mathbf{q}}\rangle$ are Bloch states with momenta $\mathbf{k}$ and $\mathbf{k}+\mathbf{q}$, and $\Delta \mathrm{V}_{\nu\mathbf{q}}$ is the lattice-periodic part of the phonon perturbation potential [56]. Since the dominant contribution to $g(\mathbf{k},\mathbf{q})$ for the 2D mode comes from Na(2) atomic vibrations, we analyze the effect of Na(2) motions on the Bi p_{xy} band, which is achieved by setting $\mathbf{e}^{(\kappa)}_{\nu\mathbf{q}}$ to 0 in Eq. 3.1 for Na(1) and Bi atoms. A similar analysis can be performed for Na(1) and Bi atomic motions, or using the Na s + Bi p_z band, but their contributions to $g(\mathbf{k},\mathbf{q})$ are significantly smaller and do not affect our conclusions.

Electron-phonon scattering rates and charge transport

We interpolate the e-ph matrix elements on fine BZ grids with up to $130\times130\times90$ $\mathbf{k}$- and $\mathbf{q}$-points using maximally localized Wannier functions [70] generated with the WANNIER90 code. [71] We then compute the e-ph scattering rates at temperature T using [56]

$$\begin{aligned}\Gamma_{n\mathbf{k}}(T) =& \frac{2\pi}{\hbar}\sum_{m\nu\mathbf{q}} |g_{mn\nu}(\mathbf{k},\mathbf{q})|^2 \\ & [(N_{\nu\mathbf{q}} + 1 - f_{mk\vec{+}q})\delta(\varepsilon_{n\mathbf{k}} - \varepsilon_{mk\vec{+}q} - \hbar\omega_{\nu\mathbf{q}}) \\ & + (N_{\nu\mathbf{q}} + f_{mk\vec{+}q})\delta(\varepsilon_{n\mathbf{k}} - \varepsilon_{mk\vec{+}q} + \hbar\omega_{\nu\mathbf{q}})],\end{aligned} \tag{3.3}$$

where $\varepsilon_{n\mathbf{k}}$ and $f_{mk\vec{+}q}$ are electron band energies and occupations, respectively, while $\hbar\omega_{\nu\mathbf{q}}$ and $N_{\nu\mathbf{q}}$ denote phonon energies and occupations. The electron and phonon occupations govern the temperature dependence of the e-ph scattering rates.

Using PERTURBO [56], we obtain the carrier mobility as a function of temperature and doping concentration by solving the linearized Boltzmann transport equation: [56]

$$\mathbf{F}_{n\mathbf{k}} = \mathbf{v}_{n\mathbf{k}}\tau_{n\mathbf{k}} + \frac{\tau_{n\mathbf{k}}}{\mathcal{N}_{\mathbf{q}}}\sum_{m,\nu\mathbf{q}} W^{\nu\mathbf{q}}_{n\mathbf{k},m\mathbf{k}+\mathbf{q}}\mathbf{F}_{m\mathbf{k}+\mathbf{q}}, \tag{3.4}$$

where $W^{\nu\mathbf{q}}_{n\mathbf{k},m\mathbf{k}+\mathbf{q}}$ are phonon mode-dependent e-ph scattering rates from electronic state $|n\mathbf{k}\rangle$ to $|m\mathbf{k}+\mathbf{q}\rangle$ due to phonon mode $(\nu,\mathbf{q})$; $\mathbf{v}_{n\mathbf{k}}$ are band velocities, $\tau_{n\mathbf{k}}$ are relaxation times, and $\mathcal{N}_{\mathbf{q}}$ is the number of $\mathbf{q}$-points used in the Brillouin zone summation. Above, $\mathbf{F}_{n\mathbf{k}}(T)$ is a term proportional to the first-order deviation of the electron occupations $f_{n\mathbf{k}}$ from their equilibrium values $f^0_{n\mathbf{k}}$ due to the electric field $\mathbf{E}$, and is defined through

$$-f^0_{n\mathbf{k}}(1 - f^0_{n\mathbf{k}})\frac{e\mathbf{E}}{k_BT}\cdot\mathbf{F}_{n\mathbf{k}} = f_{n\mathbf{k}} - f^0_{n\mathbf{k}}. \tag{3.5}$$

The conductivity tensor $\sigma_{\alpha\beta}$ is computed using

$$\sigma_{\alpha\beta} = e^2 \int dE \, (-\partial f^0/\partial E) \, \Sigma_{\alpha\beta}(E,T), \tag{3.6}$$

where α and β are Cartesian directions, and $\Sigma_{\alpha\beta}(E,T)$ is the transport distribution function at energy E and temperature T: [30]

$$\Sigma_{\alpha\beta}(E,T) = \frac{1}{\mathcal{N}_{\mathbf{k}}\Omega} \sum_{n\mathbf{k}} \mathrm{v}^{\alpha}_{n\mathbf{k}} \mathbf{F}^{\beta}_{n\mathbf{k}}(T) \delta(E - \varepsilon_{n\mathbf{k}}). \tag{3.7}$$

Here, $\mathcal{N}_{\mathbf{k}}$ is the number of $\mathbf{k}$-points in the Brillouin zone and Ω is the unit cell volume.

Lattice-distorted band structure

We compute the lattice-distorted band structure by displacing the atoms in the unit cell according to the $\mathbf{q}$=0 atomic displacements corresponding to the strongly-coupled 2D mode. The Na(2) atoms were displaced by 3% of the lattice constant, and the Bi and Na(1) atoms were displaced according to the 2D mode eigenvector. We have also verified that atomic displacements corresponding to the inversion-symmetry preserving E_{2g} mode (with energy $\sim$22 meV) generate a topological insulating phase with a band gap of 35 meV.

References

[1] N. P. Armitage, E. J. Mele, and A. Vishwanath, Rev. Mod. Phys. **90**, 015001 (2018).

[2] L. P. He, X. C. Hong, J. K. Dong, J. Pan, Z. Zhang, J. Zhang, and S. Y. Li, Phys. Rev. Lett. **113**, 246402 (2014).

[3] T. Liang, Q. Gibson, M. N. Ali, M. Liu, R. J. Cava, and N. P. Ong, Nat. Mater. **14**, 280 (2015).

[4] J. Cao, S. Liang, C. Zhang, Y. Liu, J. Huang, Z. Jin, Z.-G. Chen, Z. Wang, Q. Wang, J. Zhao, S. Li, X. Dai, J. Zou, Z. Xia, L. Li, and F. Xiu, Nat. Commun. **6**, 7779 (2015).

[5] J. Feng, Y. Pang, D. Wu, Z. Wang, H. Weng, J. Li, X. Dai, Z. Fang, Y. Shi, and L. Lu, Phys. Rev. B **92**, 081306 (2015).

[6] A. Narayanan, M. D. Watson, S. F. Blake, N. Bruyant, L. Drigo, Y. L. Chen, D. Prabhakaran, B. Yan, C. Felser, T. Kong, P. C. Canfield, and A. I. Coldea, Phys. Rev. Lett. **114**, 117201 (2015).

[7] R. Amarnath, K. S. Bhargavi, and S. S. Kubakaddi, IOP Conf. Ser.: Mater. Sci. Eng. **561**, 012030 (2019).

[8] J. Xiong, S. K. Kushwaha, T. Liang, J. W. Krizan, M. Hirschberger, W. Wang, R. J. Cava, and N. P. Ong, Science **350**, 413 (2015).

[9] J. Xiong, S. Kushwaha, J. Krizan, T. Liang, R. J. Cava, and N. P. Ong, Europhys. Lett. **114**, 27002 (2016).

[10] C.-Z. Li, L.-X. Wang, H. Liu, J. Wang, Z.-M. Liao, and D.-P. Yu, Nat. Commun. **6**, 10137 (2015).

[11] Z. Wang, Y. Sun, X.-Q. Chen, C. Franchini, G. Xu, H. Weng, X. Dai, and Z. Fang, Phys. Rev. B **85**, 195320 (2012).

[12] A. Liang, C. Chen, Z. Wang, Y. Shi, Y. Feng, H. Yi, Z. Xie, S. He, J. He, Y. Peng, Y. Liu, D. Liu, C. Hu, L. Zhao, G. Liu, X. Dong, J. Zhang, M. Nakatake, H. Iwasawa, K. Shimada, M. Arita, H. Namatame, M. Taniguchi, Z. Xu, C. Chen, H. Weng, X. Dai, Z. Fang, and X.-J. Zhou, Chin. Phys. B **25**, 077101 (2016).

[13] S.-Y. Xu, C. Liu, S. K. Kushwaha, R. Sankar, J. W. Krizan, I. Belopolski, M. Neupane, G. Bian, N. Alidoust, T.-R. Chang, H.-T. Jeng, C.-Y. Huang, W.-F. Tsai, H. Lin, P. P. Shibayev, F.-C. Chou, R. J. Cava, and M. Z. Hasan, Science **347**, 294 (2015).

[14] P. J. W. Moll, N. L. Nair, T. Helm, A. C. Potter, I. Kimchi, A. Vishwanath, and J. G. Analytis, Nature **535**, 266 (2016).

[15] J. L. Collins, A. Tadich, W. Wu, L. C. Gomes, J. N. B. Rodrigues, C. Liu, J. Hellerstedt, H. Ryu, S. Tang, S.-K. Mo, S. Adam, S. A. Yang, M. S. Fuhrer, and M. T. Edmonds, Nature **564**, 390 (2018).

[16] H. Xia, Y. Li, M. Cai, L. Qin, N. Zou, L. Peng, W. Duan, Y. Xu, W. Zhang, and Y.-S. Fu, ACS Nano **13**, 9647 (2019).

[17] A. K. Geim and K. S. Novoselov, Nat. Mater. **6**, 183 (2007).

[18] R. D. Y. Hills, A. Kusmartseva, and F. V. Kusmartsev, Phys. Rev. B **95**, 214103 (2017).

[19] W. Yanez, Y. Ou, R. Xiao, J. Koo, J. T. Held, S. Ghosh, J. Rable, T. Pillsbury, E. G. Delgado, K. Yang, J. Chamorro, A. J. Grutter, P. Quarterman, A. Richardella, A. Sengupta, T. McQueen, J. A. Borchers, K. A. Mkhoyan, B. Yan, and N. Samarth, Phys. Rev. Appl. **16**, 054031 (2021).

[20] E. J. Sie, C. M. Nyby, C. D. Pemmaraju, S. J. Park, X. Shen, J. Yang, M. C. Hoffmann, B. K. Ofori-Okai, R. Li, A. H. Reid, S. Weathersby, E. Mannebach, N. Finney, D. Rhodes, D. Chenet, A. Antony, L. Balicas, J. Hone, T. P.

Devereaux, T. F. Heinz, X. Wang, and A. M. Lindenberg, Nature **565**, 61 (2019).

[21] M. Y. Zhang, Z. X. Wang, Y. N. Li, L. Y. Shi, D. Wu, T. Lin, S. J. Zhang, Y. Q. Liu, Q. M. Liu, J. Wang, T. Dong, and N. L. Wang, Phys. Rev. X **9**, 021036 (2019).

[22] C. Vaswani, L.-L. Wang, D. H. Mudiyanselage, Q. Li, P. M. Lozano, G. D. Gu, D. Cheng, B. Song, L. Luo, R. H. J. Kim, C. Huang, Z. Liu, M. Mootz, I. E. Perakis, Y. Yao, K. M. Ho, and J. Wang, Phys. Rev. X **10**, 021013 (2020).

[23] J. Xiao, Y. Wang, H. Wang, C. D. Pemmaraju, S. Wang, P. Muscher, E. J. Sie, C. M. Nyby, T. P. Devereaux, X. Qian, X. Zhang, and A. M. Lindenberg, Nat. Phys. **16**, 1028 (2020).

[24] A. S. Disa, T. F. Nova, and A. Cavalleri, Nat. Phys. **17**, 1087 (2021).

[25] I. Sklyadneva, R. Heid, P. M. Echenique, and E. V. Chulkov, Phys. Rev. B **103**, 024303 (2021).

[26] P.-F. Liu, J. Li, C. Zhang, X.-H. Tu, J. Zhang, P. Zhang, B.-T. Wang, and D. J. Singh, Phys. Rev. B **104**, 235422 (2021).

[27] M. Bernardi, Eur. Phys. J. B **89**, 239 (2016).

[28] L. A. Agapito and M. Bernardi, Phys. Rev. B **97**, 235146 (2018).

[29] M. Bernardi, D. Vigil-Fowler, J. Lischner, J. B. Neaton, and S. G. Louie, Phys. Rev. Lett. **112**, 257402 (2014).

[30] J.-J. Zhou and M. Bernardi, Phys. Rev. B **94**, 201201(R) (2016).

[31] J.-J. Zhou, O. Hellman, and M. Bernardi, Phys. Rev. Lett. **121**, 226603 (2018).

[32] J.-J. Zhou and M. Bernardi, Phys. Rev. Res. **1**, 033138 (2019).

[33] C.-H. Park, F. Giustino, M. L. Cohen, and S. G. Louie, Phys. Rev. Lett. **99**, 086804 (2007).

[34] A. Floris, A. Sanna, S. Massidda, and E. K. U. Gross, Phys. Rev. B **75**, 054508 (2007).

[35] W. Li, Phys. Rev. B **92**, 075405 (2015).

[36] T.-H. Liu, J. Zhou, B. Liao, D. J. Singh, and G. Chen, Phys. Rev. B **95**, 075206 (2017).

[37] J. Ma, A. S. Nissimagoudar, and W. Li, Phys. Rev. B **97**, 045201 (2018).

[38] S. Poncé, E. R. Margine, and F. Giustino, Phys. Rev. B **97**, 121201 (2018).

[39] Z. K. Liu, B. Zhou, Y. Zhang, Z. J. Wang, H. M. Weng, D. Prabhakaran, S.-K. Mo, Z. X. Shen, Z. Fang, X. Dai, Z. Hussain, and Y. L. Chen, Science **343**, 864 (2014).

[40] S. K. Kushwaha, J. W. Krizan, B. E. Feldman, A. Gyenis, M. T. Randeria, J. Xiong, S.-Y. Xu, N. Alidoust, I. Belopolski, T. Liang, M. Zahid Hasan, N. P. Ong, A. Yazdani, and R. J. Cava, APL Mater. **3**, 041504 (2015).

[41] M. T. Edmonds, J. L. Collins, J. Hellerstedt, I. Yudhistira, L. C. Gomes, J. N. B. Rodrigues, S. Adam, and M. S. Fuhrer, Sci. Adv. **3**, eaao6661 (2017).

[42] I. Di Bernardo, J. Collins, W. Wu, J. Zhou, S. A. Yang, S. Ju, M. T. Edmonds, and M. S. Fuhrer, Phys. Rev. B **102**, 045124 (2020).

[43] H. F. Yuan, W. Xu, X. N. Zhao, D. Song, G. R. Zhang, Y. M. Xiao, L. Ding, and F. M. Peeters, Phys. Rev. B **99**, 235303 (2019).

[44] H. Hübener, M. A. Sentef, U. De Giovannini, A. F. Kemper, and A. Rubio, Nat. Commun. **8**, 13940 (2017).

[45] N. Tancogne-Dejean, F. G. Eich, and A. Rubio, Npj Comput. Mater. **8**, 145 (2022).

[46] R. M. Martin, *Electronic Structure: Basic Theory and Practical Methods* (Cambridge University Press, 2004).

[47] S. Baroni, S. de Gironcoli, A. Dal Corso, and P. Giannozzi, Rev. Mod. Phys. **73**, 515 (2001).

[48] M. S. Hybertsen and S. G. Louie, Phys. Rev. B **34**, 5390 (1986).

[49] G. Schweicher, G. D'Avino, M. T. Ruggiero, D. J. Harkin, K. Broch, D. Venkateshvaran, G. Liu, A. Richard, C. Ruzié, J. Armstrong, A. R. Kennedy, K. Shankland, K. Takimiya, Y. H. Geerts, J. A. Zeitler, S. Fratini, and H. Sirringhaus, Adv. Mater. **31**, 1902407 (2019).

[50] G. S. Jenkins, C. Lane, B. Barbiellini, A. B. Sushkov, R. L. Carey, F. Liu, J. W. Krizan, S. K. Kushwaha, Q. Gibson, T.-R. Chang, H.-T. Jeng, H. Lin, R. J. Cava, A. Bansil, and H. D. Drew, Phys. Rev. B **94**, 085121 (2016).

[51] D. Shao, J. Ruan, J. Wu, T. Chen, Z. Guo, H. Zhang, J. Sun, L. Sheng, and D. Xing, Phys. Rev. B **96**, 075112 (2017).

[52] W.-C. Chiu, B. Singh, S. Mardanya, J. Nokelainen, A. Agarwal, H. Lin, C. Lane, K. Pussi, B. Barbiellini, and A. Bansil, Condens. Matter **5**, 39 (2020).

[53] N. Mounet, Masters thesis (2005).

[54] P. Giannozzi, S. Baroni, N. Bonini, M. Calandra, R. Car, C. Cavazzoni, D. Ceresoli, G. L. Chiarotti, M. Cococcioni, I. Dabo, A. D. Corso, S. de Gironcoli, S. Fabris, G. Fratesi, R. Gebauer, U. Gerstmann, C. Gougoussis, A. Kokalj, M. Lazzeri, L. Martin-Samos, N. Marzari, F. Mauri, R. Mazzarello, S. Paolini, A. Pasquarello, L. Paulatto, C. Sbraccia, S. Scandolo, G. Sclauzero, A. P. Seitsonen, A. Smogunov, P. Umari, and R. M. Wentzcovitch, J. Phys. Condens. Matter **21**, 395502 (2009).

[55] X. Cheng, R. Li, Y. Sun, X.-Q. Chen, D. Li, and Y. Li, Phys. Rev. B **89**, 245201 (2014).

[56] J.-J. Zhou, J. Park, I.-T. Lu, I. Maliyov, X. Tong, and M. Bernardi, Comput. Phys. Commun. **264**, 107970 (2021).

[57] G. Pizzi, S. Milana, A. C. Ferrari, N. Marzari, and M. Gibertini, ACS Nano **15**, 12509 (2021).

[58] M. Neupane, S.-Y. Xu, R. Sankar, N. Alidoust, G. Bian, C. Liu, I. Belopolski, T.-R. Chang, H.-T. Jeng, H. Lin, A. Bansil, F. Chou, and M. Z. Hasan, Nat. Commun. **5**, 3786 (2014).

[59] C.-H. Park, N. Bonini, T. Sohier, G. Samsonidze, B. Kozinsky, M. Calandra, F. Mauri, and N. Marzari, Nano Lett. **14**, 1113 (2014).

[60] X. Tong and M. Bernardi, Phys. Rev. Res. **3**, 023072 (2021).

[61] D. C. Desai, B. Zviazhynski, J.-J. Zhou, and M. Bernardi, Phys. Rev. B **103**, L161103 (2021).

[62] X.-X. Dong, J.-X. Chen, Y. Wang, Z.-L. Lv, and H.-Y. Wang, Mater. Res. Express **6**, 076308 (2019).

[63] R. Merlin, Solid State Commun. **102**, 207 (1997).

[64] K.-P. Bohnen, R. Heid, and B. Renker, Phys. Rev. Lett. **86**, 5771 (2001).

[65] J. M. An and W. E. Pickett, Phys. Rev. Lett. **86**, 4366 (2001).

[66] J. P. Perdew, A. Ruzsinszky, G. I. Csonka, O. A. Vydrov, G. E. Scuseria, L. A. Constantin, X. Zhou, and K. Burke, Phys. Rev. Lett. **100**, 136406 (2008).

[67] M. van Setten, M. Giantomassi, E. Bousquet, M. Verstraete, D. Hamann, X. Gonze, and G.-M. Rignanese, Comput. Phys. Commun. **226**, 39 (2018).

[68] D. Sangalli, A. Ferretti, H. Miranda, C. Attaccalite, I. Marri, E. Cannuccia, P. Melo, M. Marsili, F. Paleari, A. Marrazzo, G. Prandini, P. Bonfà, M. O. Atambo, F. Affinito, M. Palummo, A. Molina-Sánchez, C. Hogan, M. Grüning, D. Varsano, and A. Marini, J. Phys. Condens. Matter **31**, 325902 (2019).

[69] F. Bruneval and X. Gonze, Phys. Rev. B **78**, 085125 (2008).

[70] N. Marzari, A. A. Mostofi, J. R. Yates, I. Souza, and D. Vanderbilt, Rev. Mod. Phys. **84**, 1419 (2012).

[71] A. A. Mostofi, J. R. Yates, G. Pizzi, Y.-S. Lee, I. Souza, D. Vanderbilt, and N. Marzari, Comput. Phys. Commun. **185**, 2309 (2014).

Chapter 4

FIRST-PRINCIPLES MAGNETOTRANSPORT WITH BAND TOPOLOGY FOR QUANTITATIVE MODELING OF CHIRAL ANOMALY AND NONLINEAR HALL EFFECT

This chapter is a slightly modified version of the manuscript: D. C. Desai, J.-J. Zhou, S. Peng, J. Park, and M. Bernardi, "First-principles magnetotransport with band topology for quantitative modeling of chiral anomaly and nonlinear Hall effect", to be submitted. D.C.D participated in the conception of the project, performed calculations, analyzed the data, and participated in the writing of the manuscript.

4.1 Introduction

Band topology is a central theme in quantum materials and is responsible for emergent features such as robust edge states [1–3], topological superconductivity [4], spin Hall effects [5, 6], and unconventional transport [7–9]. This novel physics is relevant for wide-ranging applications in electronics, spintronics and quantum technology [10, 11]. The theory of Berry curvature and topological invariants provides a deeper understanding of topological phases [3]. These developments have also led to predictions and discoveries of topological transport regimes, including the chiral anomaly [12–14] and nonlinear Hall effect (NLHE) [15, 16].

Although predictions of chiral anomaly in solids have a long history [17], this effect has been observed only recently in topological Weyl semimetals in the form of a large negative longitudinal magnetoresistance (LMR) [18–25]. The decrease in resistance is caused by charge pumping between two Weyl cones when parallel electric and magnetic fields are applied. Experiments on Weyl semimetals have achieved resistivities decreasing more than 50% at large magnetic fields [18, 20]. This behavior contrasts with magnetotransport in topologically trivial materials, where the LMR is positive and increases with magnetic field.

The NLHE is a more recent development in topological transport, and has become an exciting research topic with measurements reported in a wide range of materials [26–34]. Unlike the chiral anomaly, the NLHE does not require a magnetic field or magnetization, but rather it is an intrinsic higher-order response to an electric field resulting in a nonlinear Hall effect [15].

Previous theoretical work used a combination of the semiclassical Boltzmann transport equation (BTE) and Berry curvature to study the chiral anomaly [35, 36] and NLHE [16]. These studies advance qualitative understanding of topological transport, but focus on models with simplifying approximations such as constant relaxation times and Berry curvature dipole (BCD) from band theory without interactions.

First-principles calculations using density functional theory (DFT) [37] and its linear-response variant, density functional perturbation theory (DFPT) [38], have enabled studies of band topology and electronic Berry curvature [39, 40] and separately electron-phonon (e-ph) interactions and phonon-limited electronic transport [41–50]. However, studies combining these advances are nearly absent, with the exception of very recent calculations by Lihm et al. [51] predicting a significant enhancement of the NLHE in GeTe due to e-ph interactions. Yet, first-principles calculations of chiral anomaly are still missing, the NLHE has not been studied in a wider range of materials, and a unified framework to study chiral transport and the NLHE on the same footing is still lacking.

Here, we show first-principles calculations of resistivity and magnetotransport in the prototypical Weyl semimetal TaAs, as well as nonlinear Hall conductivities and interaction-renormalized BCD in bulk $BaMnSb_2$, bilayer WTe_2 (BL-WTe_2), and strained monolayer WSe_2 (ML-WSe_2). Our approach combines first-principles e-ph interactions and Berry curvature, and allows us to access both classical (Lorentz) and quantum (chiral) contributions to magnetotransport, and to sample electronic momenta with large Berry curvatures using an importance-sampling technique. Our predicted resistivity and magnetoresistance in TaAs are in very good agreement with experiments (both within 40% of measured values) and shed light on the relative magnitudes of classical and chiral contributions. Our calculations of nonlinear Hall conductivities and BCD show a strong interplay between e-ph interactions and Berry curvature in the NLHE. Taken together, this paper provides an accurate method for studying intrinsic (e-ph limited) transport properties in the presence of nontrivial band topology and shed light on their microscopic origin.

4.2 Methods

We describe the chiral anomaly starting from the semiclassical equations of motion (EOM). In a material with applied electric and magnetic fields ($\mathbf{E}$ and $\mathbf{B}$ respectively), the EOM for position ($\mathbf{x}$) and momentum ($\mathbf{k}$) are modified by the Berry curvature $\Omega_{n\mathbf{k}}$ and become [52, 53]

$$\begin{aligned}\dot{\mathbf{x}} &= \frac{1}{1+\frac{e}{\hbar}\mathbf{B}\cdot\mathbf{\Omega}_{n\mathbf{k}}}[\mathbf{v}_{n\mathbf{k}} + \frac{e}{\hbar}\mathbf{E}\times\mathbf{\Omega}_{n\mathbf{k}} + \frac{e}{\hbar}(\mathbf{v}_{n\mathbf{k}}\cdot\mathbf{\Omega}_{n\mathbf{k}})\mathbf{B}] \\ \dot{\mathbf{k}} &= \frac{-e}{\hbar}\frac{1}{1+\frac{e}{\hbar}\mathbf{B}\cdot\mathbf{\Omega}_{n\mathbf{k}}}[\mathbf{E} + \mathbf{v}_{n\mathbf{k}}\times\mathbf{B} + \frac{e}{\hbar}(\mathbf{E}\cdot\mathbf{B})\mathbf{\Omega}_{n\mathbf{k}}],\end{aligned} \tag{4.1}$$

where e is the electron charge, $\hbar$ is Planck's constant, and $\mathbf{v}_{n\mathbf{k}}$ is the band velocity for a Bloch state with crystal momentum $\mathbf{k}$ and band index n. Using these EOMs, we derive a modified linearized BTE that takes band topology into account. At steady state, the BTE reads:

$$\begin{aligned}&\frac{1}{1+\frac{e}{\hbar}\mathbf{B}\cdot\mathbf{\Omega}_{n\mathbf{k}}}(\mathbf{v}_{n\mathbf{k}} + \frac{e}{\hbar}(\mathbf{v}_{n\mathbf{k}}\cdot\mathbf{\Omega}_{n\mathbf{k}})\mathbf{B} + \frac{e}{\hbar}(\mathbf{v}_{n\mathbf{k}}\times\mathbf{B})\nabla_{\mathbf{k}}\mathbf{F}_{n\mathbf{k}}) \\ &\quad = \frac{1}{\mathcal{N}_{\mathbf{q}}}\sum_{m,\nu\mathbf{q}}(1+\frac{e}{\hbar}\mathbf{B}\cdot\mathbf{\Omega}_{m\mathbf{k}+\mathbf{q}})W^{\nu\mathbf{q}}_{n\mathbf{k},m\mathbf{k}+\mathbf{q}}(\mathbf{F}_{n\mathbf{k}} - \mathbf{F}_{m\mathbf{k}+\mathbf{q}}),\end{aligned} \tag{4.2}$$

where $\mathbf{F}_{n\mathbf{k}}$ is proportional to the change in electronic occupations relative to equilibrium, $f_{n\mathbf{k}} - f^0_{n\mathbf{k}} = -f^0_{n\mathbf{k}}(1-f^0_{n\mathbf{k}})\frac{e\mathbf{E}}{k_BT}\cdot\mathbf{F}_{n\mathbf{k}}$, with $f^0_{n\mathbf{k}}$ the Fermi-Dirac distribution [54]. The right-hand side of Eq. (4.2) is the collision term, where $W^{\nu\mathbf{q}}_{n\mathbf{k},m\mathbf{k}+\mathbf{q}}$ is the scattering rate from state $|n\mathbf{k}\rangle$ to $|m\mathbf{k}+\mathbf{q}\rangle$ due to absorption or emission of a phonon (with wave-vector $\mathbf{q}$ and mode index ν) as defined in [54] and $\mathcal{N}_{\mathbf{q}}$ is the number of $\mathbf{q}$-points in the summation. The factor $(1+\frac{e}{\hbar}\mathbf{B}\cdot\mathbf{\Omega}_{m\mathbf{k}+\mathbf{q}})$ on the right-hand arises from the Berry phase correction to the electron density of states [55].

Solving for $\mathbf{F}_{n\mathbf{k}}$ gives the conductivity tensor $\sigma_{\alpha\beta}$ in the Cartesian directions α and β [54],

$$\sigma_{\alpha\beta} = \frac{e^2S}{\mathcal{N}_{\mathbf{k}}Vk_{\mathrm{B}}T}\sum_{n\mathbf{k}}(1+\frac{e}{\hbar}\mathbf{B}\cdot\mathbf{\Omega}_{n\mathbf{k}})f^0_{n\mathbf{k}}(1-f^0_{n\mathbf{k}})\,\dot{\mathbf{x}}_{\alpha}\mathbf{F}_{n\mathbf{k}}(\mathbf{B})_{\beta}, \tag{4.3}$$

where S, V and $\mathcal{N}_{\mathbf{k}}$ are the spin-degeneracy, unit-cell volume, and number of unit cells respectively. The implicit dependence of σ on Berry curvature gives rise to chiral transport in Weyl semimetals. In particular, the anomalous term in Eq. (4.1) causes the conductivity to increase with magnetic field (negative LMR), in contrast with the usual decrease caused by the Lorentz force in simple metals [12].

The NLHE can be described with a similar formalism. We expand the expression for current density $\mathbf{J}$ to second order in the applied electric field [15]:

$$J_{\alpha} = \sigma_{\alpha\beta}E_{\beta} + \chi_{\alpha\beta\gamma}E_{\beta}E_{\gamma}, \tag{4.4}$$

where we sum over repeated indices; $\sigma_{\alpha\beta}$ is defined above and its transverse (Hall) components are zero in systems with time reversal symmetry. Therefore, the leading order Hall response is given by the second-order term $\chi_{\alpha\beta\gamma}E_\beta E_\gamma$. To obtain an expression for the third-rank conductivity tensor χ, we start from the current,

$$\mathbf{J} = \frac{-Se}{\mathcal{N}_\mathbf{k} V}\sum_{n\mathbf{k}} f_{n\mathbf{k}}\mathbf{v}_{n\mathbf{k}}. \tag{4.5}$$

Setting $\mathbf{B}$=0 in Eqs. (4.1) and (4.3) and plugging in the above expression for $\mathbf{J}$, we obtain

$$\chi_{\alpha\beta\gamma} = \epsilon_{\alpha\beta\delta}T_{\delta\gamma} + \epsilon_{\alpha\gamma\delta}T_{\delta\beta} \tag{4.6}$$

where $\epsilon_{\alpha\beta\gamma}$ is the Levi-Civita tensor and

$$T_{\alpha\beta} = \frac{e^3 S}{2\mathcal{N}_\mathbf{k} V\hbar k_\mathrm{B} T}\sum_{n\mathbf{k}} f^0_{n\mathbf{k}}(1 - f^0_{n\mathbf{k}})\,(\mathbf{\Omega}_{n\mathbf{k}})_\alpha(\mathbf{F}_{n\mathbf{k}})_\beta \tag{4.7}$$

This formula reduces the computation of the rank-three tensor $\chi_{\alpha\beta\gamma}$ to the computation of the rank-two tensor $T_{\alpha\beta}$. In the literature, using a constant relaxation time approximation this tensor is written as [16] $T_{\alpha\beta} = \frac{e^3 S\tau}{2\hbar^2}D_{\alpha\beta}$, where $D_{\alpha\beta}$ is the Berry curvature dipole defined within band theory without interactions [16]:

$$D_{\alpha\beta} = \int \frac{d^d\mathbf{k}}{(2\pi)^d}\Omega_{n\mathbf{k},\alpha}\frac{\partial f^{(0)}_{n\mathbf{k}}}{\partial k_\beta}. \tag{4.8}$$

We modify this expression to incorporate momentum-dependent e-ph scattering by defining a renormalized Berry curvature dipole

$$D^{\mathrm{e-ph}}_{\alpha\beta} = T_{\alpha\beta}\frac{2\hbar^2}{e^3 S\tau_\mathrm{avg}} = T_{\alpha\beta}\frac{2\hbar^2}{e^3 S}\left(\frac{\sum_{n\mathbf{k}} f^0_{nk}(1 - f^0_{n\mathbf{k}})\Gamma_{n\mathbf{k}}}{\sum_{n\mathbf{k}} f^0_{nk}(1 - f^0_{n\mathbf{k}})}\right) \tag{4.9}$$

where τ_avg is the average relaxation time. As we show below, the e-ph renormalization has a significant effect on the Berry curvature dipole and is essential to accurately predict the NLHE.

We implement Eqs. (4.2) and (4.7) in our open-source code PERTURBO [54]. The electronic ground state, band structure, and Berry curvature, as well as the lattice dynamics are computed for each material using QUANTUM ESPRESSO [56, 57]. We use maximally localized Wannier functions [58] from the WANNIER90 code [59]

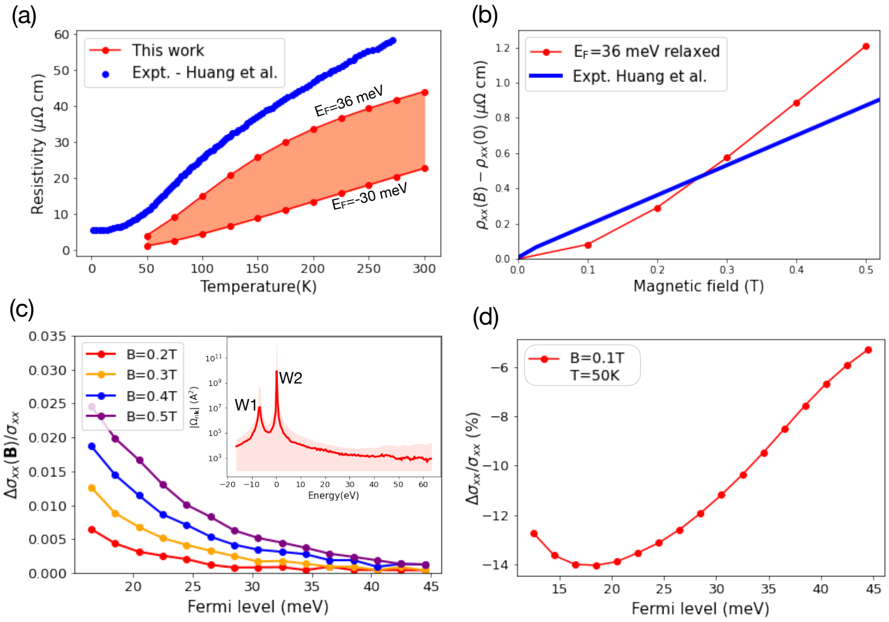

Figure 4.1: Magnetotransport in TaAs. (a) Resistivity as a function of temperature for Fermi energies within ±35 meV of the Weyl nodes. (b) Longitudinal magnetoresistance, $\rho_{xx}(\mathbf{B}) - \rho_{xx}(0)$, versus magnetic field at $T = 100$ K. Experimental data are from Ref. [19]. (c) Chiral contribution, and (d) Lorentz contribution, to the longitudinal magnetoconductance as a function of Fermi energy for different values of magnetic field.

and employ Perturbo to compute and interpolate the e-ph matrix elements on fine grids and obtain converged transport properties [54]. To compute the conductivity in Eq. (4.3), we develop an adaptive refinement technique that generates a nonuniform $\mathbf{k}$-grid to optimally sample states with large Berry curvatures. Additional details are provided in the Supplemental Material (SM) (section 4.5).

4.3 Results

We first discuss transport and chiral anomaly in TaAs. Figure 4.1(a) shows the phonon-limited resistivity ρ_{xx} in TaAs as a function of temperature for a range of Fermi energies within 30 meV of the Weyl node. Our results agree with experimental data from Ref. [19]. In particular, for temperatures above $\sim$200 K, where transport is usually limited by e-ph interactions, our predicted resistivity is within 30% of the measured values. The resistivity differs from experiments by a factor of $2-3$ at low temperatures, where transport is governed by scattering with defects and impurities not considered in this work. Figure 4.1(b) shows the classical (Lorentz) contribution to the magnetoresistance, $\rho_{xx}(B) - \rho_{xx}(0)$ for magnetic fields applied along the x-axis, which is also in quantitative agreement with experiments [19]. These results point to a dominant role of e-ph interactions in controlling the resistivity and magnetotransport in TaAs.

To quantify the chiral anomaly in the presence of e-ph interactions, we compute the chiral contribution (the second term in the left-hand side of Eq. (4.2)) to the longitudinal magnetoconductance, $\Delta\sigma_{xx}(\mathbf{B})/\sigma_{xx}$. Figure 4.1(c) shows this quantity as a function of Fermi energy for different magnetic field values at T=50 K. Consistent with experimental data and previous theoretical work, the magnetoconductance is positive and increases with magnetic field. This is a clear signature of chiral transport since the classical contribution (third term in Eq. (4.2)) leads to a conductance decreasing with magnetic field.

To better understand the trends in Fig. 4.1(c), we analyze the distribution of Berry curvature as a function of electron energy (inset of Fig. 4.1(c)). In our calculations,TaAs exhibits 12 pairs of Weyl nodes, with 8 pairs at zero energy (labelled W2), and 4 pairs at -10 meV (labelled W1), consistent with previous calculations [19, 60] and angle-resolved photoemission spectroscopy (ARPES) measurements [61]. We consider lightly n-doped systems with Fermi energy above the Weyl nodes. As a result, the dominant contribution to magnetoconductance comes from the large Berry curvature near the W2 nodes. As the chiral contribution is proportional to the Berry curvature, we expect the chiral anomaly to be more pronounced for E_F close to the W2 nodes, and to decay sharply for increasing Fermi energies. This is precisely the behavior observed in our calculations in Fig. 4.1(c).

We additionally analyze the Lorentz contribution to the magnetoconductance (at T=50 K for B=0.1 T) in Fig. 4.1(d). We find that this is significantly larger than the chiral contribution in Fig. 4.1(c), and attribute this to the Lorentz term dominating in the semiclassical limit (see SM 4.5 for additional discussion). The divergence of the Berry curvature near the W2 nodes leads to a breakdown of the semiclassical limit, which restricts our calculations to Fermi energies more than 10 meV away from the Weyl nodes. In this energy window, the chiral contribution is found to decay rapidly with increasing Fermi energy, enhancing the transverse velocity from the classical term. Our approach can quantify both classical and topological contributions to the conductivity in this range of higher Fermi energies. This can help rationalize the experimental data from Ref. [21], where the Fermi energies of the samples are much closer to the Weyl nodes, and thus the chiral contribution

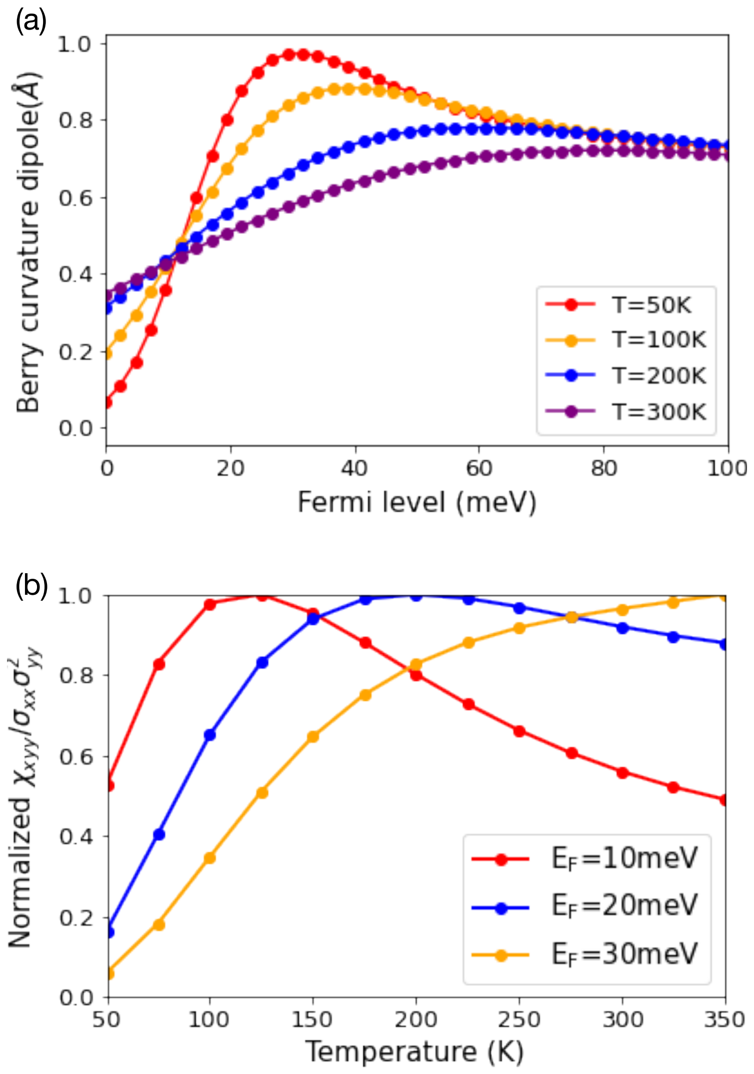

Figure 4.2: (a) Berry curvature dipole D_{yz} as a function of Fermi energies for different temperatures. (b) Hall response $(\chi_{xyy}/(\sigma_{xx}\sigma_{yy}^2))$ as a function of temperature for Fermi energies near the conduction band minimum. The response has been normalized to one by diving the response by its peak values.

dominates magnetotransport. Transport calculations in this energy window within a few meV of the Weyl nodes will require a quantum treatment involving Landau levels, a topic left for future work.

We now turn to calculations of NLHE. We first discuss $BaMnSb_2$, a bulk material with a strong nonlinear Hall response near room temperature, as shown in recent experiments [31]. As e-ph scattering is expected to play an important role at such temperatures, we compute the BCD renormalized by e-ph interactions using Eq. (4.9) and show it in Fig. 4.2(a) as a function of Fermi energy for different temperatures. At low temperature, the BCD exhibits a sharp characteristic peak for E_F = 30 meV, consistent with previous calculations [31]. We find that the BCD decreases with temperature, a trend we attribute to increasing e-ph interactions and carrier thermal excitation near the Fermi energy, both of which smooth out the 30-meV peak.

A quantity suitable for direct comparison with experiments is the Hall response V_{xyy}/I_y^2, where V_{xyy} is the nonlinear Hall voltage generated along the x-direction on application of a current I_y along the y-axis. A straightforward calculation shows that the Hall response measured in experiments is proportional to $\chi_{xyy}/\sigma_{xx}\sigma_{yy}^2$. We compute this quantity in Fig. 4.2(b) and show it as a function of temperature for Fermi energies near the BCD peak. The Hall response at E_{F}=20 meV peaks around 200 K, consistent with the experimental observation of a response peak at high temperature [31]. As we show in Fig. 4.2(b), small changes in Fermi energy can alter the temperature trend significantly. Because Hall responses depend on both the second-order conductivities χ_{xyy} and the linear conductivities (σ_{xx} and σ_{yy}), theories of NLHE based on the BCD alone cannot predict the Hall response without knowledge of the scattering time τ. For example, using Eqs. (4.6) and (2.7), we can show that $(\chi_{xyy}/\sigma_{xx}\sigma_{yy}^2) \propto 1/\tau^2$ in the constant relaxation time approximation (RTA). Such a strong dependence on τ highlights the importance of accurately including scattering effects for quantitative predictions of NLHE.

We next study the NLHE and e-ph renormalized BCD in two 2D materials, bilayer WTe_2 and strained ML-WSe_2, where previous work reported the existence of a finite BCD [26, 62]. In ML-WSe_2, it has been shown that breaking C_3 symmetry by applying a uniaxial strain along the a-axis induces a finite BCD and Hall response [34, 62]. Accordingly, we perform our calculations on 3$\%$ strained ML-WSe_2.

Figure 4.3(a) shows D_{xz}^{e-ph} at T=50 K and T=140 K for several different Fermi energies in the valence band, and compares it with the original values D_{xz} (defined in Eqn. (4.8)). We find that e-ph interactions significantly change the dipoles. Additionally, while original BCD is nearly constant between T=50 K and T=140 K, e-ph interactions induce markedly different responses at these temperatures. Note that the increase in dipole between T=50 K and T=140 K measured by Qin et al. [34] agrees with our calculations of D_{xz}^{e-ph}, a trend not captured by the original values D_{xz}.

Figure 4.3(b) shows D_{xz}^{e-ph} in BL-WTe_2 for calculations performed both in the RTA approximation and using the full BTE at T=100 K. BL-WTe_2 has a small band gap,

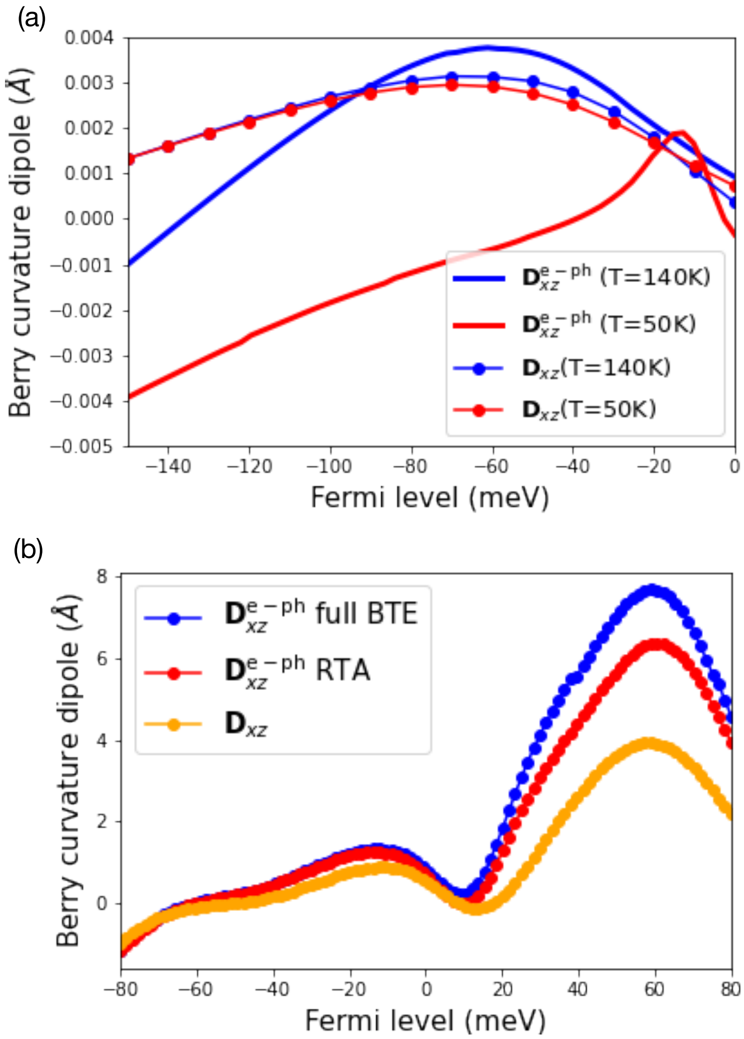

Figure 4.3: (a) Original and e-ph normalized dipoles D_{xz} in strained ML-WSe$_2$ at T=50 K (red)and T=140 K (blue). (b) D_{xz} for original (orange), e-ph normalization using RTA (red) and using full BTE (blue) at T=100 K in bilayer WTe$_2$.

and placing the Fermi energy near the band edge leads to large Berry curvatures, and thus a large dipole. A comparison of D_{xz}^{e-ph} in the RTA approximation with the original values(defined in Eq. (4.8)) shows a 50% enhancement near the conduction band preak in BL-WTe$_2$. A further enhancement is observed with a full BTE calculation, which predicts a 2× change compared to the original value. The changes in dipole induced by e-ph interactions highlight their importance in quantifying nonlinear Hall transport and correctly capturing its dependence on crucial quantities such as temperature.

4.4 Conclusion

In conclusion, this work demonstrates precise calculations of chiral anomaly and NLHE in topologically nontrivial materials. We compute chiral magnetoconductance in TaAs, providing accurate values in the semiclassical limit. Our calculations of the normalized Hall responses in $BaMnSb_2$ are consistent with experiments, and our comparison of the intrinsic and e-ph normalized BCD in strained ML-WSe_2 and BL-WTe_2 highlight the critical role of e-ph interactions to obtain quantitative predictions for the NLHE. Our formalism improves on previous predictions by being able to provide accurate estimates of topological transport. Building on the success of first-principles calculations in predicting transport in quantum materials, this formalism can be applied to a wide range of topological semimetals and semiconductors, paving the way for a better microsopic understanding of quantum processes in topological materials and expanding their practical applications.

4.5 Supplemental material

Computational Details

The ground state, electronic bandstructures and phonons in TaAs, $BaMnSb_2$, monolayer WSe_2, and bilayer WTe_2 are obtained using the QUANTUM ESPRESSO code [56]. We relax the TaAs structure using PBE exchange correlation functional and compute charge density using a coarse $12{\times}12{\times}12$ $\mathbf{k}$ grid. The lattice constants are a=b=3.437 Åand c=11.656 Å. We use fully relativistic norm-conserving pseudopotentials with spin-orbit coupling (SOC), an energy cutoff of 72 Ry and a Marzari-Vanderbilt smearing scheme with smearing parameter of 0.01 Ry. The electron wavefunctions and phonon properties are computed on $8{\times}8{\times}8$ $\mathbf{k}$ and $4{\times}4{\times}4$ $\mathbf{q}$ grids respectively. We generate maximally localized Wannier functions using the WANNIER90 code [59] to interpolate electron and phonon properties on fine grids. For $BaMnSb_2$, we relax the crystal structure by performing a spin-polarized calculation without SOC using the PBEsol [63] exchange-correlation functional, an energy cutoff of 90Ry and a Hubbard correction parameter U=5 eV for Mn atoms. The lattice constants are a=4.539 Å, b=4.497 Åand c=24.30 Å. We use $8{\times}8{\times}2$ and $4{\times}4{\times}1$ $\mathbf{k}$ and $\mathbf{q}$ grids for electron and phonon properties respectively. For monolayer WSe_2, we relax the lattice constants using PBE exchange correlation functional with SOC and an energy cutoff of 100Ry, obtaining 3.27 Åfor the relaxed value. We further relax the atomic positions after applying 3% strain along the x-direction. The electron wavefunctions and phonons are computed on coarse $24{\times}24{\times}1$ and $12{\times}12{\times}1$ $\mathbf{k}$ and $\mathbf{q}$ grids respectively. Finally, for bilayer WTe_2, we use the HSE06

Hybrid functional [64] with SOC to relax the crystal structure with a screening parameter 0.4^{-1} [26], and obtain lattice constants a=3.477 Å, b=6.249 Å. We use a 16×8×1 $\mathbf{k}$ $\mathbf{k}$ grid to compute electron wavefunctions and charge densities. Note that while electronic properties are obtained using the HSE06 functional, we use PBE to compute phonons on a 4×2×1 $\mathbf{q}$ grid.

Berry curvature, e-ph interactions and transport

We use our in-house open-source code PERTURBO [54] to calculate Berry curvature, e-ph interactions, and transport properties. We have developed routines to calculate Berry curvature based on the formalism developed by Wang et al. [39]. We benchmark our code by comparing Berry curvatures calculated using our routines and using WANNIER90. Additionally, we employ a 201×201×201 $\mathbf{k}$ and relaxation time approximation (RTA) to compute the classical contributions to charge transport and magnetotransport (Figs. 4.1(a), 4.1(b), and 4.1(d) in the main text). For chiral transport (Fig. 4.1(c)), we use the full BTE and a non-uniform adaptive $\mathbf{k}$ grid developed in PERTURBO to sample more points near the Weyl cones. We outline a detailed implementation of the adaptive grid in the next section. For $BaMnSb_2$, since the calculation of e-ph interactions for spin-polarized DFT calculations for noncollinear spins is not implemented yet, our bandstructure and phonons have been computed without SOC. However, we calculate Berry curvature using the SOC bandstructure and wavefunctions, and map them to our no SOC bandstructure to get a better accuracy for the Berry curvature dipoles and nonlinear Hall transport. Our calculations of BCD transport and e-ph interactions in $BaMnSb_2$, strained monolayer WSe_2 and bilayer WTe_2 are performed on extremely fine $\mathbf{k}$ and $\mathbf{q}$ grids of 501×501×4, 1000×1000×1, and 400×400×1 respectively. We have implemented routines to calculate the original and e-ph normalized BCD in PERTURBO, and have benchmarked the accuracy of our calculations with WANNIER BERRI code [65].

Adaptive grid implementation in TaAs

TaAs has a complex Fermi surface with 24 pairs of Weyl nodes, in addition to electron and hole pockets. As a result, uniform grids, even of the order of 200^3, are unsuccessful in capturing the Berry curvature divergence near the Weyl nodes. Since the Weyl nodes have a small Fermi surface compared to the trivial pockets, chiral transport requires very fine $\mathbf{k}$ grids of 1000×1000×1000 or higher to achieve convergence and sample Weyl singularities effectively. However, the computational

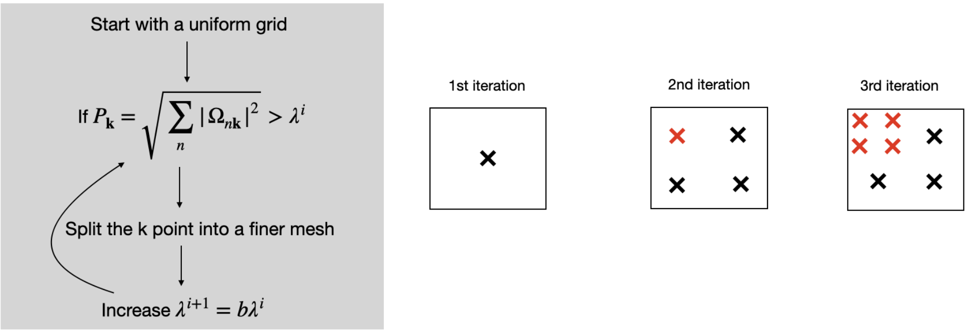

Figure 4.4: Algorithm for implementing an adaptive mesh. The red points are denoted as the points which satisfy Eqn. (4.10).

cost of e-ph coupling and transport calculations on such grids is prohibitively expensive, as the number of $\mathbf{k}$ points is very large (8 million) for a 1000^3 grid, even if only points with energies within a narrow window of the Weyl cones are considered.

To overcome this challenge, we devise an adaptive scheme to generate a non-uniform grid of $\mathbf{k}$ points based on the values of the Berry curvature at each $\mathbf{k}$. We start with a uniform $\mathbf{k}$ grid, and compute the Berry curvature at each point. We evaluate the quantity

$$P_{\mathbf{k}} = \sqrt{\sum_n |\Omega_{n\mathbf{k}}|^2} > \lambda^i \tag{4.10}$$

for a specified threshold λ_i, where i denotes the iteration. If $P_{\mathbf{k}} > \lambda^i$, we further split the $\mathbf{k}$ point into $2^3 = 8$ finer points, and repeat the procedure again, now with an updated threshold $\lambda^{i+1} = b\lambda^i$. A schematic of this algorithm is shown in Fig. 4.4.

Using this technique, we sample Weyl points with a sampling rate equivalent to that of a $1\text{M}\times1\text{M}\times1\text{M}$ $\mathbf{k}$ grid, although using only 200000 $\mathbf{k}$ points. A comparison of the Berry curvatures between $\mathbf{k}$ points on a 256^3 and 1000^3 grid and an adaptive mesh built on a 128^3 grid is shown in Fig. 4.5. This technique reduces the computational cost significantly while achieving dramatic accuracy.

Note that since the grid is now non-uniform, the collision integral in the right hand side of Boltzmann Transport Equation (Eq. (4.2) in the main text) is modified. One can calculate the collision terms by recasting the summation over phonon momenta $\mathbf{q}$ as summation over the final electronic state $\mathbf{k}' = \mathbf{k} + \mathbf{q}$. We obtain

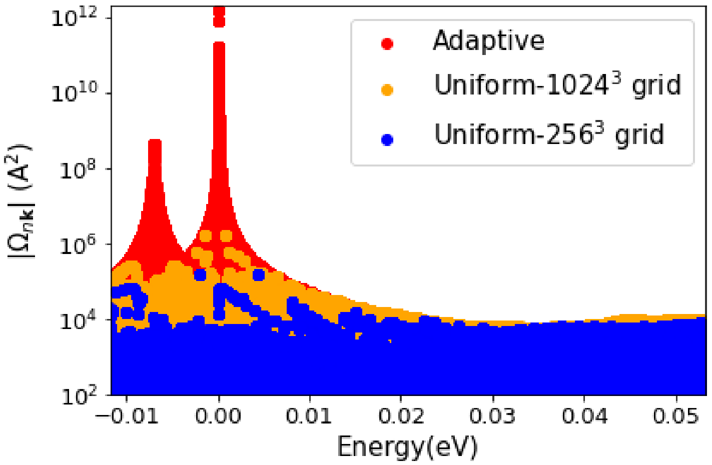

Figure 4.5: Comparison of Berry curvatures for a 256^3 uniform grid (blue), 1000^3 uniform grid (orange), and adaptive grid (red).

$$\begin{aligned}\frac{1}{1+\frac{e}{\hbar}\mathbf{B}\cdot\mathbf{\Omega}_{n\mathbf{k}}}(\mathbf{v}_{n\mathbf{k}}+\frac{e}{\hbar}(\mathbf{v}_{n\mathbf{k}}\cdot\mathbf{\Omega}_{n\mathbf{k}})\mathbf{B}+\frac{e}{\hbar}(\mathbf{v}_{n\mathbf{k}}\times\mathbf{B})\nabla_{\mathbf{k}}\mathbf{F}_{n\mathbf{k}})\\ =\sum_{m,\nu\mathbf{k}'}w_{\mathbf{k}'}(1+\frac{e}{\hbar}\mathbf{B}\cdot\mathbf{\Omega}_{m\mathbf{k}+\mathbf{q}})W^{\nu(\mathbf{k}'-\mathbf{k})}_{n\mathbf{k},m\mathbf{k}'}(\mathbf{F}_{n\mathbf{k}}-\mathbf{F}_{m\mathbf{k}'}),\end{aligned} \tag{4.11}$$

where $w_{\mathbf{k}'}$ refers to the weight of the $\mathbf{k}'$ point. We implement Eq. (4.11) in PERTURBO.

Breakdown of the semiclassical limit

Di Xiao et al. [55] proposed a phase space correction to the density of states arising from Berry curvature. As a result, all integrals over electronic momentum space are accompanied by a factor $(1+\frac{e}{\hbar}\mathbf{B}\cdot\mathbf{\Omega}_{n\mathbf{k}})$, where $\mathbf{B}$ is the magnetic field. Based on this correction factor, a quantitative limit to the breakdown of the semiclassical limit can be established, particularly in Weyl semimetals.

We expect that the density of states correction is small for weak magnetic fields. Based on the above condition, we can identify the Fermi energies in the semiclassical limit as energy regions where $\frac{e}{\hbar}|\mathbf{B}||\mathbf{\Omega}_{n\mathbf{k}}| \ll 1$. Since Berry curvature diverges at the Weyl nodes, we expect the inequality to be violated in regions close to the Weyl nodes. The shaded area in Fig. 4.6 shows the semiclassical region at B=0.3 T, where the BTE formalism describes electron dynamics accurately. The calculations in Fig. 4.1(c) in the main text are performed for Fermi energies in this region. However, for strong magnetic fields and for Fermi energies close to the Weyl node, a more comprehensive approach involving Landau levels is required.

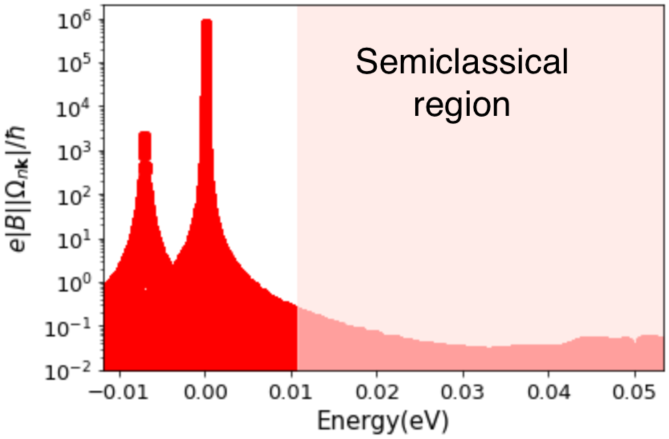

Figure 4.6: $\frac{e}{\hbar}|\mathbf{B}||\mathbf{\Omega}_{n\mathbf{k}}|$ as a function of electron energies for B=0.3 T. The shaded region represents the semiclassical limit where y-values are much smaller than 1.

References

[1] C. L. Kane and E. J. Mele, Phys. Rev. Lett. **95**, 226801 (2005).

[2] X.-L. Qi and S.-C. Zhang, Rev. Mod. Phys. **83**, 1057 (2011).

[3] M. Z. Hasan and C. L. Kane, Rev. Mod. Phys. **82**, 3045 (2010).

[4] L. Fu and C. L. Kane, Phys. Rev. Lett. **100**, 096407 (2008).

[5] B. A. Bernevig, T. L. Hughes, and S.-C. Zhang, Science **314**, 1757 (2006).

[6] X.-L. Qi and S.-C. Zhang, Phys. Today **63**, 33 (2010).

[7] Z. Zhang, N. Wang, N. Cao, A. Wang, X. Zhou, K. Watanabe, T. Taniguchi, B. Yan, and W.-b. Gao, Nat. Commun. **13**, 6191 (2022).

[8] A. Farrell and T. Pereg-Barnea, Phys. Rev. B **93**, 045121 (2016).

[9] D. Hsieh, Y. Xia, D. Qian, L. Wray, J. H. Dil, F. Meier, J. Osterwalder, L. Patthey, J. G. Checkelsky, N. P. Ong, A. V. Fedorov, H. Lin, A. Bansil, D. Grauer, Y. S. Hor, R. J. Cava, and M. Z. Hasan, Nature **460**, 1101 (2009).

[10] M. He, H. Sun, and Q. L. He, Front. Phys. **14**, 43401 (2019).

[11] Q. L. He, T. L. Hughes, N. P. Armitage, Y. Tokura, and K. L. Wang, Nat. Mater. **21**, 15 (2022).

[12] N. P. Armitage, E. J. Mele, and A. Vishwanath, Rev. Mod. Phys. **90**, 015001 (2018).

[13] A. A. Zyuzin and A. A. Burkov, Phys. Rev. B **86**, 115133 (2012).

[14] N. P. Ong and S. Liang, Nat. Rev. Phys. **3**, 394 (2021).

[15] Z. Z. Du, H.-Z. Lu, and X. C. Xie, Nat. Rev. Phys. **3**, 744 (2021).

[16] I. Sodemann and L. Fu, Phys. Rev. Lett. **115**, 216806 (2015).

[17] H. B. Nielsen and M. Ninomiya, Phys. Lett. B **130**, 389 (1983).

[18] J. Xiong, S. K. Kushwaha, T. Liang, J. W. Krizan, M. Hirschberger, W. Wang, R. J. Cava, and N. P. Ong, Science **350**, 413 (2015).

[19] X. Huang, L. Zhao, Y. Long, P. Wang, D. Chen, Z. Yang, H. Liang, M. Xue, H. Weng, Z. Fang, X. Dai, and G. Chen, Phys. Rev. X **5**, 031023 (2015).

[20] C.-Z. Li, L.-X. Wang, H. Liu, J. Wang, Z.-M. Liao, and D.-P. Yu, Nat. Commun. **6**, 10137 (2015).

[21] C.-L. Zhang, S.-Y. Xu, I. Belopolski, Z. Yuan, Z. Lin, B. Tong, G. Bian, N. Alidoust, C.-C. Lee, S.-M. Huang, T.-R. Chang, G. Chang, C.-H. Hsu, H.-T. Jeng, M. Neupane, D. S. Sanchez, H. Zheng, J. Wang, H. Lin, C. Zhang, H.-Z. Lu, S.-Q. Shen, T. Neupert, M. Zahid Hasan, and S. Jia, Nat. Commun. **7**, 10735 (2016).

[22] S. Liang, J. Lin, S. Kushwaha, J. Xing, N. Ni, R. J. Cava, and N. P. Ong, Phys. Rev. X **8**, 031002 (2018).

[23] M. Hirschberger, S. Kushwaha, Z. Wang, Q. Gibson, S. Liang, C. Belvin, B. A. Bernevig, R. J. Cava, and N. P. Ong, Nat. Mater. **15**, 1161 (2016).

[24] R. D. dos Reis, M. O. Ajeesh, N. Kumar, F. Arnold, C. Shekhar, M. Naumann, M. Schmidt, M. Nicklas, and E. Hassinger, New J. Phys. **18**, 085006 (2016).

[25] Y. Li, Z. Wang, P. Li, X. Yang, Z. Shen, F. Sheng, X. Li, Y. Lu, Y. Zheng, and Z.-A. Xu, Front. Phys. **12**, 127205 (2017).

[26] Q. Ma, S.-Y. Xu, H. Shen, D. MacNeill, V. Fatemi, T.-R. Chang, A. M. Mier Valdivia, S. Wu, Z. Du, C.-H. Hsu, S. Fang, Q. D. Gibson, K. Watanabe, T. Taniguchi, R. J. Cava, E. Kaxiras, H.-Z. Lu, H. Lin, L. Fu, N. Gedik, and P. Jarillo-Herrero, Nature **565**, 337 (2019).

[27] M. Huang, Z. Wu, J. Hu, X. Cai, E. Li, L. An, X. Feng, Z. Ye, N. Lin, K. T. Law, and N. Wang, Natl. Sci. Rev. **10**, nwac232 (2022).

[28] S.-C. Ho, C.-H. Chang, Y.-C. Hsieh, S.-T. Lo, B. Huang, T.-H.-Y. Vu, C. Ortix, and T.-M. Chen, Nat. Electron **4**, 116 (2021).

[29] P. He, H. Isobe, D. Zhu, C.-H. Hsu, L. Fu, and H. Yang, Nat. Commun. **12**, 698 (2021).

[30] A. Tiwari, F. Chen, S. Zhong, E. Drueke, J. Koo, A. Kaczmarek, C. Xiao, J. Gao, X. Luo, Q. Niu, Y. Sun, B. Yan, L. Zhao, and A. W. Tsen, Nat. Commun. **12**, 2049 (2021).

[31] L. Min, H. Tan, Z. Xie, L. Miao, R. Zhang, S. H. Lee, V. Gopalan, C.-X. Liu, N. Alem, B. Yan, and Z. Mao, Nat. Commun. **14**, 364 (2023).

[32] K. Kang, T. Li, E. Sohn, J. Shan, and K. F. Mak, Nat. Mater. **18**, 324 (2019).

[33] O. O. Shvetsov, V. D. Esin, A. V. Timonina, N. N. Kolesnikov, and E. V. Deviatov, JETP Lett. **109**, 715 (2019).

[34] M.-S. Qin, P.-F. Zhu, X.-G. Ye, W.-Z. Xu, Z.-H. Song, J. Liang, K. Liu, and Z.-M. L. o, Chin. Phys. Lett. **38**, 017301 (2021).

[35] D. T. Son and B. Z. Spivak, Phys. Rev. B **88**, 104412 (2013).

[36] K.-S. Kim, H.-J. Kim, and M. Sasaki, Phys. Rev. B **89**, 195137 (2014).

[37] R. M. Martin, *Electronic Structure: Basic Theory and Practical Methods* (Cambridge University Press, 2004).

[38] S. Baroni, S. de Gironcoli, A. Dal Corso, and P. Giannozzi, Rev. Mod. Phys. **73**, 515 (2001).

[39] X. Wang, J. R. Yates, I. Souza, and D. Vanderbilt, Phys. Rev. B **74**, 195118 (2006).

[40] W. Feng, C.-C. Liu, G.-B. Liu, J.-J. Zhou, and Y. Yao, Comput. Mater. Sci. **112**, 428 (2016).

[41] J.-J. Zhou and M. Bernardi, Phys. Rev. B **94**, 201201(R) (2016).

[42] V. A. Jhalani, J.-J. Zhou, and M. Bernardi, Nano Lett. **17**, 5012 (2017).

[43] N.-E. Lee, J.-J. Zhou, L. A. Agapito, and M. Bernardi, Phys. Rev. B **97**, 115203 (2018).

[44] N.-E. Lee, J.-J. Zhou, H.-Y. Chen, and M. Bernardi, Nat. Commun. **11**, 1607 (2020).

[45] J. Park, J.-J. Zhou, V. A. Jhalani, C. E. Dreyer, and M. Bernardi, Phys. Rev. B **102**, 125203 (2020).

[46] W. Li, Phys. Rev. B **92**, 075405 (2015).

[47] T. Sohier, D. Campi, N. Marzari, and M. Gibertini, Phys. Rev. Mater. **2**, 114010 (2018).

[48] D. C. Desai, B. Zviazhynski, J.-J. Zhou, and M. Bernardi, Phys. Rev. B **103**, L161103 (2021).

[49] D. J. Abramovitch, J.-J. Zhou, J. Mravlje, A. Georges, and M. Bernardi, Phys. Rev. Mater. **7**, 093801 (2023).

[50] I.-T. Lu, J.-J. Zhou, J. Park, and M. Bernardi, Phys. Rev. Mater. **6**, L010801 (2022).

[51] J.-M. Lihm and C.-H. Park, Phys. Rev. Lett. **132**, 106402 (2024).

[52] G. Sundaram and Q. Niu, Phys. Rev. B **59**, 14915 (1999).

[53] D. Xiao, M.-C. Chang, and Q. Niu, Rev. Mod. Phys. **82**, 1959 (2010).

[54] J.-J. Zhou, J. Park, I.-T. Lu, I. Maliyov, X. Tong, and M. Bernardi, Comput. Phys. Commun. **264**, 107970 (2021).

[55] D. Xiao, J. Shi, and Q. Niu, Phys. Rev. Lett. **95**, 137204 (2005).

[56] P. Giannozzi, S. Baroni, N. Bonini, M. Calandra, R. Car, C. Cavazzoni, D. Ceresoli, G. L. Chiarotti, M. Cococcioni, I. Dabo, A. D. Corso, S. de Gironcoli, S. Fabris, G. Fratesi, R. Gebauer, U. Gerstmann, C. Gougoussis, A. Kokalj, M. Lazzeri, L. Martin-Samos, N. Marzari, F. Mauri, R. Mazzarello, S. Paolini, A. Pasquarello, L. Paulatto, C. Sbraccia, S. Scandolo, G. Sclauzero, A. P. Seitsonen, A. Smogunov, P. Umari, and R. M. Wentzcovitch, J. Phys. Condens. Matter **21**, 395502 (2009).

[57] P. Giannozzi, O. Andreussi, T. Brumme, O. Bunau, M. B. Nardelli, M. Calandra, R. Car, C. Cavazzoni, D. Ceresoli, M. Cococcioni, N. Colonna, I. Carnimeo, A. D. Corso, S. de Gironcoli, P. Delugas, R. A. DiStasio, A. Ferretti, A. Floris, G. Fratesi, G. Fugallo, R. Gebauer, U. Gerstmann, F. Giustino, T. Gorni, J. Jia, M. Kawamura, H.-Y. Ko, A. Kokalj, E. Küçükbenli, M. Lazzeri, M. Marsili, N. Marzari, F. Mauri, N. L. Nguyen, H.-V. Nguyen, A. O. de-la Roza, L. Paulatto, S. Poncé, D. Rocca, R. Sabatini, B. Santra, M. Schlipf, A. P. Seitsonen, A. Smogunov, I. Timrov, T. Thonhauser, P. Umari, N. Vast, X. Wu, and S. Baroni, J. Phys. Condens. Matter **29**, 465901 (2017).

[58] N. Marzari, A. A. Mostofi, J. R. Yates, I. Souza, and D. Vanderbilt, Rev. Mod. Phys. **84**, 1419 (2012).

[59] A. A. Mostofi, J. R. Yates, G. Pizzi, Y.-S. Lee, I. Souza, D. Vanderbilt, and N. Marzari, Comput. Phys. Commun. **185**, 2309 (2014).

[60] J. Buckeridge, D. Jevdokimovs, C. R. A. Catlow, and A. A. Sokol, Phys. Rev. B **93**, 125205 (2016).

[61] L. X. Yang, Z. K. Liu, Y. Sun, H. Peng, H. F. Yang, T. Zhang, B. Zhou, Y. Zhang, Y. F. Guo, M. Rahn, D. Prabhakaran, Z. Hussain, S.-K. Mo, C. Felser, B. Yan, and Y. L. Chen, Nat. Phys. **11**, 728 (2015).

[62] J.-S. You, S. Fang, S.-Y. Xu, E. Kaxiras, and T. Low, Phys. Rev. B **98**, 121109 (2018).

[63] J. P. Perdew, A. Ruzsinszky, G. I. Csonka, O. A. Vydrov, G. E. Scuseria, L. A. Constantin, X. Zhou, and K. Burke, Phys. Rev. Lett. **100**, 136406 (2008).

[64] J. P. Perdew, A. Ruzsinszky, G. I. Csonka, O. A. Vydrov, G. E. Scuseria, L. A. Constantin, X. Zhou, and K. Burke, J. Chem. Phys. **118**, 82107 (2003).

[65] S. S. Tsirkin, Npj Comput. Mater. **7**, 33 (2021).

Chapter 5

ELECTRON-PHONON BAND RENORMALIZATION AND SUPERCONDUCTIVITY IN STRAINED RUO2

This chapter is a slightly modified version of the manuscript: D. C. Desai, Y. Luo, and M. Bernardi, "Electron-phonon band renormalization and superconductivity in strained RuO_2", to be submitted. D.C.D participated in the conception of the project, performed calculations, analyzed the data, and participated in the writing of the manuscript.

5.1 Introduction

Ruthenium oxide (RuO_2) is one of the most promising transition metal oxide (TMO) platforms to host high electrical conductivity and catalytic properties [1]. In recent years, studies of RuO_2 have gone beyond conventional transport and observed quantum behavior, including strain-enhanced superconductivity [2, 3], metal-insulator transition [4, 5], altermagnetism [6–12], and anomalous Hall effects [8, 13]. These properties make RuO_2 a very intriguing quantum material.

Experimental developments in RuO_2 have prompted many efforts on the computational forefront to analyze the microscopic processes governing these phenomena in more detail. However, while the band structure and electronic properties [2, 14–17] in RuO_2 have been well studied using Density Functional Theory (DFT) [18], the effects of phonons and e-ph interactions in RuO_2 remain less explored. Understanding e-ph interactions is crucial to explaining not only transport properties, but also other novel effects such as superconductivity and band renormalization. To our knowledge, only two recent works [2, 3] have computed e-ph interactions in strained RuO_2 to explain superconductivity enhancement upon application of strain.

RuO_2 thin films grown along the [110] direction on TiO_2 crystals are inherently strained, due to a large lattice mismatch with the TiO_2 substrates [2]. It has been found that a compressive strain of 4.7$\%$ along [001] alters the band structure, in addition to inducing a significant phonon anharmonicity [3]. This lattice anharmonicity poses a challenge to the calculation of e-ph interactions and superconducting T_c, causing unphysical divergences. Typically, to these avoid divergences, one imposes a phonon frequency cutoff by excluding phonons with energies below a small value, of the order of $\sim$1meV. However, this approach excludes soft modes with imaginary frequencies, potentially overlooking important physics. Recent advances to compute temperature dependent phonons using the temperature-dependent effective potentials (TDEP) [19] or stochastic self-consistent harmonic approximation (SSCHA) [20] methods have provided more accurate treatments of these soft modes. For example, previous work by Zhou et al. [21] has shown a significant improvement in e-ph interactions and mobility in Strontium Titanate ($SrTiO_3$) using the TDEP method.

In this work, we calculate e-ph interactions in RuO_2, taking into account Hubbard corrections to the DFT band structure and temperature dependence of phonons using

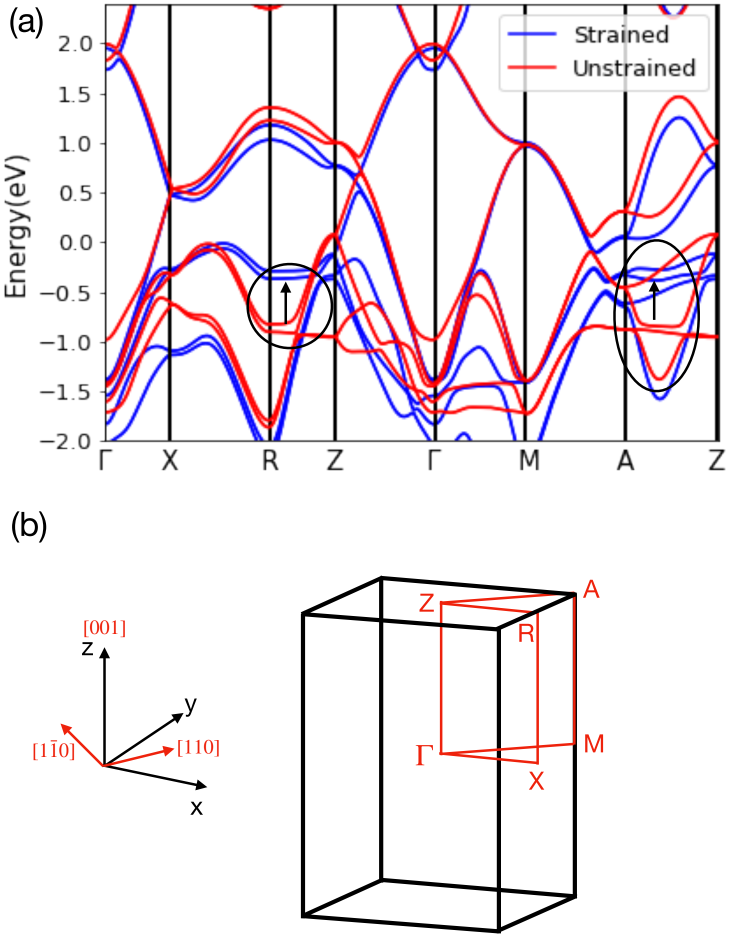

Figure 5.1: (a)A comparison of the band structures of strained (blue) and unstrained (red) RuO_2 calculated along the high symmetry path. The arrow represents a shift of the flat bands towards the Fermi level. (b) A schematic of the Brillouin zone of RuO_2. The high-symmetry path and the directions of strain are shown in red.

the SSCHA method. We further compute e-ph induced band renormalization and superconducting T$_c$ using the isotropic Migdal-Eliashberg formalism [22]. Our calculations of the band renormalization predict sharp kinks near the Fermi level at low temperature, highlighting the importance of e-ph interactions in capturing accurate band structure. Moreover, our calculations of the Eliashberg spectral function and superconducting T_c are in good agreement with experiments, and demonstrate that a combination of strain and doping can significantly enhance e-ph coupling and T_c. Note that our calculations also include soft modes not taken into account previously, ensuring maximum accuracy.

5.2 Results

RuO$_2$ phonons and e-ph coupling

Unstrained RuO$_2$ belongs to the tetragonal $P4_2/mnm$ space group. Application of strain reduces the space group symmetry, resulting in an orthorhombic structure. A comparison of the resulting band structure of the strained and unstrained phases along the high-symmetry path is shown in Fig. 5.1(a). The high-symmetry path is highlighted in red in the Brillouin zone in Fig. 5.1(b), along with the strain directions $[1\bar{1}0]$ and $[001]$. Consistent with ARPES measurements and previous calculations [2], there is a significant change in the band structure near the Fermi level. Particularly, the bands along the paths in the k$_z$ plane (R-Z and A-Z) become flat (represented by arrows in Fig. 5.1(a)), and are pushed up by 0.5 eV, resulting in an increase in the density of states near 0 eV (as defined in Fig. 5.1(a)). These flat bands in the k$_z$ in plane are comprised of $d_{||}$ orbitals [2], and contribute significantly

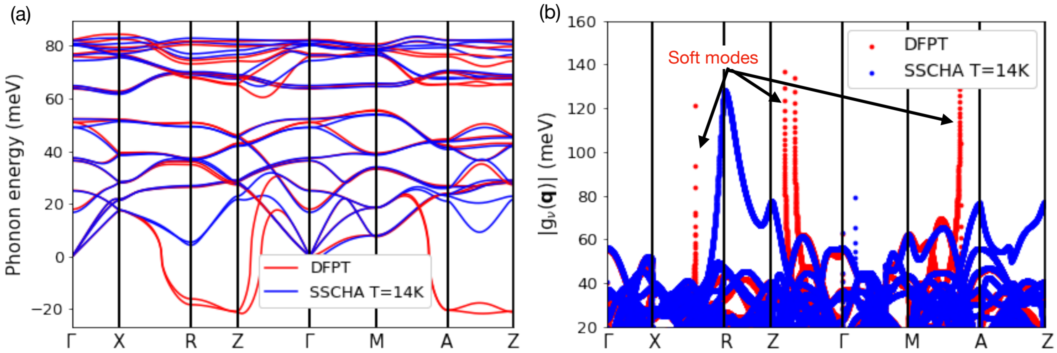

Figure 5.2: (a)Phonon dispersions along the high-symmetry path for strained RuO$_2$. The red curve denotes the DFPT calculation, and the blue curve denotes the temperature dependent SSCHA corrections at T=14 K. (b) e-ph coupling matrix elements $g_\nu(\mathbf{q})$ for DFPT(red) and SSCHA(blue) calculations.

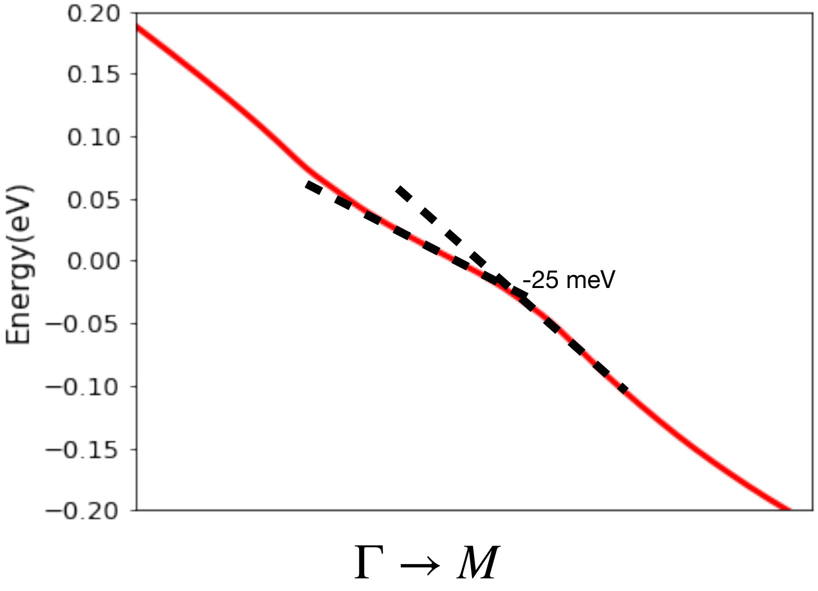

Figure 5.3: E-ph corrected band structure along the $\Gamma - M$ direction. The Fermi energy E_F is set to 0 eV.

to changes in the physical properties of RuO_2.

Figure 5.2(a) shows the phonon dispersions for strained RuO_2 along the high-symmetry path. We find that a DFPT calculation (red) predicts soft modes for phonons with momenta along the k_z plane, consistent with previous works [3]. While the crystal structure for the unstrained phase is dynamically stable, significant anharmonicity arises upon application of a large 4.7$\%$ compressive strain along the [001] direction. We refine the DFPT calculations using SSCHA to calculate harmonic phonons at T=14 K (blue curve in Fig. 5.2(a)). These corrections take into account the temperature dependence and the phonon anharmonicity to stabilize the phonon dispersions.

We compare the resulting e-ph interactions for DFPT and SSCHA corrected phonons in Fig. 5.2(b). We plot $|g_\nu(\mathbf{q})|$ = $[\sum_{m,n} |g_{mn\nu}(k_{1\bar{1}0} = -0.51\text{Å}^{-1}, \mathbf{q})|^2/N_b]^{1/2}$, where $g_{mn\nu}(\mathbf{k}, \mathbf{q})$ is defined in section 5.4, and N_b is the number of bands in the summation. We chose $k_{1\bar{1}0} = -0.51\text{Å}^{-1}$ as the band energy of this point is at the zero of the Fermi level. Note that the soft modes in the DFPT calculation lead to unphysical divergences in $|g_\nu(\mathbf{q})|$, which are removed by imposing SSCHA corrections. Using the e-ph interactions computed with the SSCHA method, we now calculate the band structure corrections and superconducting T_c.

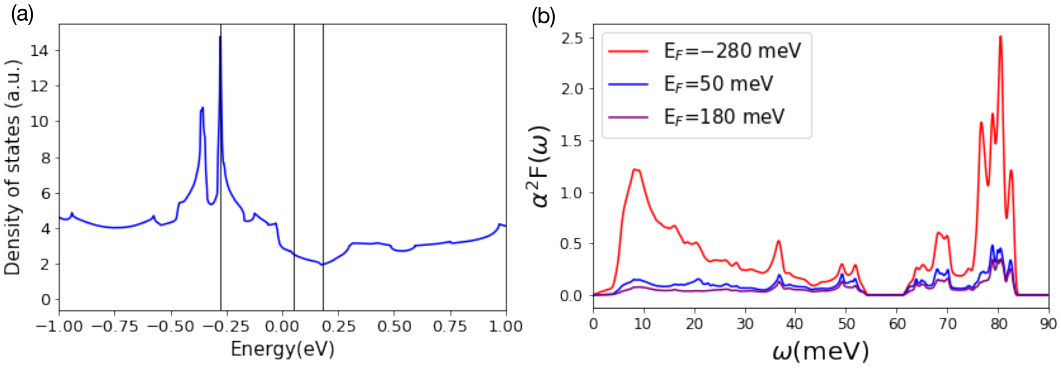

Figure 5.4: (a) Density of states within in strained RuO_2. The vertical black lines represent the Fermi energies at which Eliashberg spectral functions are evaluated in (b).

Electron-phonon band renormalization and superconductivity

We compute the e-ph corrected band structure for **k** along the $\Gamma - M$ direction (Fig. 5.2) with E$_F$ set to 0 eV. The corrections are obtained by computing the real part of the e-ph self energy, defined in section 5.4. We find that e-ph interactions significantly modify the band structure along $\Gamma - M$. The band structure displays a kink ∼25 meV below the Fermi level. This kink results from strong e-ph interactions in RuO_2 and can be observed using angle-resolved photoemission spectroscopy measurements. Similar kinks have been observed and predicted in several other materials [23–27], and act as observable signatures of strong electronic interactions. Taking these kinks into account while calculating physical properties such as transport is essential, as they significantly renormalize the band structure and velocity.

We now compute phonon-limited superconducting properties in strained RuO_2. Since the superconducting temperature T_c depends on the density of states (DOS) near E$_F$ [28], we first analyze DOS in strained RuO_2 in Fig. 5.2(a). There is a sharp peak at -280 meV originating from the flat d bands shown in Fig. 5.1(a). We find that DOS decreases significantly as energy is increased, with a nearly 7× drop at E=180 meV. Consequently, the Eliashberg spectral function $\alpha F^2(\omega)$ (defined in section 5.4) computed at E$_F$=−280 meV, 50 meV and 180 meV exhibits a large variability. Fig. 5.2(b) shows that $\alpha F^2(\omega)$ is significantly greater for E$_F$=−280 meV, and decreases with increasing E$_F$ up to 180 meV.

The quantity $\alpha F^2(\omega)$ is a measure of the effective e-ph coupling strength in any material, and directly relates to its superconducting properties. The phonon-mediated

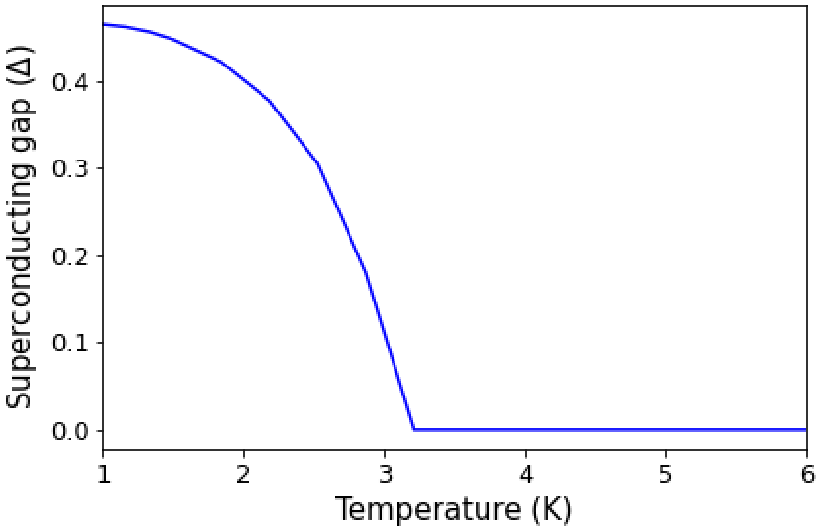

Figure 5.5: Superconducting gap Δ as a function of temperature for strained RuO_2 with E_F = 50 meV.

superconducting T_c can be calculated using the Migdal-Eliashberg formalism outlined in section 5.4. To quantify the changes in the spectral function between different Fermi energies, one can compute the average e-ph coupling strength, defined as [29]

$$\lambda^{\text{e-ph}} = 2 \int d\omega \frac{\alpha F^2(\omega)}{\omega}. \tag{5.1}$$

We calculate $\lambda^{\text{e-ph}}$ to be 0.33, 0.61, and 3.40 for E_F = 180 meV, 50 meV, and -280 meV. The coupling strength at $E_F = -280$ meV is nearly $10\times$ higher than at E_F=180 meV. This enhancement is attributed to the presence of flat bands and a large DOS. The variability of $\lambda^{\text{e-ph}}$ for different E_F provides a potential route to tune T_c in RuO_2 by doping.

Note that the weight of the spectral function for low-frequency phonons in Fig. 5.2(b) increases significantly for $E_F = -280$ meV. This increased weight is attributed to strong e-ph coupling for soft phonon modes described earlier, highlighting their role in T_c enhancement in strained RuO_2. Therefore, accurately treating these soft phonons is crucial to converging the superconducting properties, reaffirming the importance of applying temperature-dependent SSCHA corrections. Overall, our calculations show that an appropriate combination of strain and doping can significantly enhance T_c in RuO_2.

Finally, to compare our calculations with experiments, we evaluate the superconducting gap as a function of temperature at E_F=50 meV in Fig. 5.2 (details outlined in section 5.4). The gap goes to zero at T_c = 3.2 K. This temperature is in good agreement with measurements from Refs. [2] and [3], which observe an experimental T_c of 1.7 K - 2.0 K. While Fig. 5.2 shows a T_c calculation for E_F=50 meV, we have verified that varying Fermi energy within 200 meV of the zero point predicts a wide range of T_c, with the experimental measurements falling within this range. This agreement suggests that superconductivity observed in strained RuO_2 is possibly phonon-mediated, consistent with previous calculations [2, 3].

5.3 Conclusion

To conclude, we have demonstrated accurate calculations of e-ph interactions, band structure corrections and superconducting properties in strained RuO_2. Our calculations take into account Hubbard as well as temperature-dependent corrections to electronic and phononic properties respectively. We demonstrate observable signatures of strong e-ph coupling in the form of sharp kinks in the e-ph corrected band structure. Our calculations of the Eliashberg spectral function show that superconducting properties can be significantly enhanced by adjusting the Fermi energy. Moreover, our computed T_c values near the zero Fermi energy are in good quantitative agreement with experimental measurements of T_c, suggesting phonon-mediated superconductivity as a possible dominant mechanism in strained RuO_2. This work remains ongoing, and with the recent identification of RuO_2 as a prototypical altermagnet, we plan to extend our research to investigate the impact of magnetism on superconducting properties. Overall, our calculations shed light on the quantum properties in RuO_2, and demonstrates the importance of microsopic e-ph interactions in governing superconductivity.

5.4 Methods

Computational Details

The electronic ground state, wavefunctions and energies are computed using the QUANTUM ESPRESSO code [30]. We relax the atomic positions and the lattice constant along the [110] direction, while applying a fixed 2.2$\%$ strain along the [$1\bar{1}0$] direction and -4.7$\%$ along the [001] direction. The lattice constants for strained RuO_2 along [001], [$1\bar{1}0$], and [110] directions are 2.95 Å, 6.45 Å, and 6.41 Å respectively. We use the Hubbard parameter U=2 eV to correct the electronic band structure. The calculations employ a coarse $12\times8\times8$ $\mathbf{k}$ grid.

The phononic properties are computed using density functional perturbation theory (DFPT) [31] as implemented in QUANTUM ESPRESSO, and are further refined using the SSCHA code [20] to incorporate temperature dependence. The DFPT calculations are performed on a coarse 4×4×2 grid. For SSCHA calculations, we use an ensemble of 750 and 500 different configurations for T=14 K and T=160 K respectively, each composed of 4×4×2 supercell with random thermal displacements. While we use the Hubbard corrections to correct the band structure and wavefunctions, are phononic properties are computed using a plain DFT calculation.

We use the WANNIER90 [32] code to compute maximally localized Wannier functions [33] to interpolate electron and phonon properties on fine grids.

Electron-phonon coupling and band renormalization

The electron-phonon coupling matrix elements are calculated using the formula

$$g_{mn\nu}(\mathbf{k},\mathbf{q}) = \sqrt{\frac{\hbar}{2\omega_{\nu\mathbf{q}}}} \langle\psi_{m\mathbf{k}+\mathbf{q}}| \Delta V_{\nu\mathbf{q}} |\psi_{n\mathbf{k}}\rangle \,, \tag{5.2}$$

where $\hbar$ is the Planck's constant. $|\psi_{n\mathbf{k}}\rangle$ and $|\psi_{m\mathbf{k}+\mathbf{q}}\rangle$ denote the initial and final electronic states with band indices m,n and electron momenta $\mathbf{k}$ and $\mathbf{k}+\mathbf{q}$ respectively. $\omega_{\nu\mathbf{q}}$ and $\Delta V_{\nu\mathbf{q}}$ represent the phonon frequencies and perturbation potentials for a phonon with momentum $\mathbf{q}$ and mode index ν respectively.

Using the definition of e-ph coupling in Eq. 5.2, we can calculate the band structure corrections using the real part of the lowest order Fan-Migdal e-ph self energy, defined as [34, 35]

$$\Sigma_{n\mathbf{k}}(E,T) = \sum_{\nu\mathbf{q}m} |g_{mn\nu}(\mathbf{k},\mathbf{q})|^2 [\frac{N_{\nu\mathbf{q}} + 1 - f_{m\mathbf{k}+\mathbf{q}}}{E - \epsilon_{m\mathbf{k}+\mathbf{q}} - \hbar\omega_{\nu\mathbf{q}} - i\eta} + \frac{N_{\nu\mathbf{q}} + f_{m\mathbf{k}+\mathbf{q}}}{E - \epsilon_{m\mathbf{k}+\mathbf{q}} + \hbar\omega_{\nu\mathbf{q}} - i\eta}], \tag{5.3}$$

where $N_{\nu\mathbf{q}}$, $f_{m\mathbf{k}+\mathbf{q}}$ denote the phonon and electronic occupations given by the Bose-Einstein and Fermi-Dirac distributions respectively. $\epsilon_{m\mathbf{k}+\mathbf{q}}$, T and η represent the electronic energies, temperature and the smearing factor respectively. The real part of $\Sigma_{n\mathbf{k}}$ evaluated on-shell gives the correction to the DFT band structure.

$$\tilde{\epsilon}_{n\mathbf{k}} = \epsilon_{n\mathbf{k}} + \mathrm{Re}\Sigma_{n\mathbf{k}}(\epsilon_{n\mathbf{k}}, T). \tag{5.4}$$

We compute Re$\Sigma_{n\mathbf{k}}$ at T=14 K and T=160 K for $\mathbf{k}$ along the Γ-M direction with a Lorentzian smearing η = 10 meV and 10^7 uniform random $\mathbf{q}$ points.

Isotropic Eliashberg spectral function and superconducting T$_c$

Using the Migdal-Eliashberg theory, the isotropic Eliashberg function can be computed as [22, 35]

$$\begin{aligned} \alpha^2F(\omega) &= \frac{1}{2}\sum_{\nu\mathbf{q}} \omega_{\nu\mathbf{q}}\lambda_{\nu\mathbf{q}}\delta(\omega-\omega_{\nu\mathbf{q}}), \\ \lambda_{\nu\mathbf{q}} &= \frac{1}{N(\epsilon_F)\omega_{\nu\mathbf{q}}}\sum_{mn}|g_{mn\nu}(\mathbf{k},\mathbf{q})|^2\delta(\epsilon_{n\mathbf{k}}-\epsilon_F)\delta(\epsilon_{m\mathbf{k}+\mathbf{q}}-\epsilon_F), \end{aligned} \tag{5.5}$$

where $N(\epsilon_F)$ is the density of states at the Fermi level (ϵ_F). One can then solve for the superconducting temperature T$_c$ by evaluating the gap function Δ and the mass renormalization function Z

$$\begin{aligned} Z(i\omega_j) &= 1+\frac{\pi k_B T}{\omega_j}\sum_{j'}\frac{\omega_{j'}}{\sqrt{\omega_{j'}^2+\Delta^2(i\omega_j)}}\lambda(\omega_j-\omega_{j'}) \\ Z(i\omega_j)\Delta(i\omega_j) &= \pi k_B T\sum_{j'}\frac{\Delta(i\omega_{j'})}{\sqrt{\omega_{j'}^2+\Delta^2(i\omega_{j'})}}(\lambda(\omega_j-\omega_{j'})-\mu_c^*). \end{aligned} \tag{5.6}$$

Here, $\omega_j = \pi k_B T(2j+1)$ is the Matsubara frequency, $\lambda(\omega_j) = \int_0^\infty d\omega\alpha^2F(\omega)(2\omega/\omega_j^2+\omega^2)$ is the e-ph coupling strength and μ_c^* is a parameter representing the screened Coulomb potential. Using Eqs. (5.5) and (5.6), one can solve for the superconducting gap Δ. The superconducting temperature T$_c$ is the temperature at which $\Delta(\pi k_B T(2j+1))$ = 0.

We use random 400000 $\mathbf{k}$ and 200000 $\mathbf{q}$ points respectively to compute $\alpha^2F(\omega)$ using Eq. (5.5), with Gaussians of smearing 15 meV electrons and 0.2 meV to represent the delta functions for electrons and phonons respectively. Our calculations use μ_c^* = 0.3 [2]. We then solve for the superconducting gap and obtain T$_c$ using Eq. (5.6).

References

[1] H. Over, Chemical Reviews **112**, 3356 (2012).

[2] J. P. Ruf, H. Paik, N. J. Schreiber, H. P. Nair, L. Miao, J. K. Kawasaki, J. N. Nelson, B. D. Faeth, Y. Lee, B. H. Goodge, B. Pamuk, C. J. Fennie, L. F. Kourkoutis, D. G. Schlom, and K. M. Shen, Nat. Commun. **12**, 59 (2021).

[3] M. Uchida, T. Nomoto, M. Musashi, R. Arita, and M. Kawasaki, Phys. Rev. Lett. **125**, 147001 (2020).

[4] A. K. Rajapitamahuni, S. Nair, Z. Yang, A. K. Manjeshwar, S. G. Jeong, W. Nunn, and B. Jalan, Phys. Rev. Mater. **8**, 075002 (2024).

[5] D. Kutsuzawa, D. Oka, and T. Fukumura, Phys. Status Solidi B **257**, 2000188 (2020).

[6] O. Fedchenko, J. Minár, A. Akashdeep, S. W. D'Souza, D. Vasilyev, O. Tkach, L. Odenbreit, Q. Nguyen, D. Kutnyakhov, N. Wind, L. Wenthaus, M. Scholz, K. Rossnagel, M. Hoesch, M. Aeschlimann, B. Stadtmüller, M. Kläui, G. Schönhense, T. Jungwirth, A. B. Hellenes, G. Jakob, L. Šmejkal, J. Sinova, and H.-J. Elmers, Sci. Adv. **10**, eadj4883 (2024).

[7] K.-H. Ahn, A. Hariki, K.-W. Lee, and J. Kuneš, Phys. Rev. B **99**, 184432 (2019).

[8] Z. Feng, X. Zhou, L. Šmejkal, L. Wu, Z. Zhu, H. Guo, R. González-Hernández, X. Wang, H. Yan, P. Qin, X. Zhang, H. Wu, H. Chen, Z. Meng, L. Liu, Z. Xia, J. Sinova, T. Jungwirth, and Z. Liu, Nat. Electron **5**, 735 (2022).

[9] A. Ptok, ArXiv Cond-Mat (2023), arXiv:2309.02421 [cond-mat.mtrl-sci] .

[10] S. W. Lovesey, D. D. Khalyavin, and G. van der Laan, Phys. Rev. B **108**, L121103 (2023).

[11] S. Basak and A. Ptok, Acta Phys. Pol. A **145**, 93–96 (2024).

[12] A. Smolyanyuk, I. I. Mazin, L. Garcia-Gassull, and R. Valentí, Phys. Rev. B **109**, 134424 (2024).

[13] T. Tschirner, P. Keßler, R. D. Gonzalez Betancourt, T. Kotte, D. Kriegner, B. Büchner, J. Dufouleur, M. Kamp, V. Jovic, L. Smejkal, J. Sinova, R. Claessen, T. Jungwirth, S. Moser, H. Reichlova, and L. Veyrat, APL Mater. **11**, 101103 (2023).

[14] N. Mehtougui, D. Rached, R. Khenata, H. Rached, M. Rabah, and S. Bin-Omran, Mater. Sci. Semicond. Process. **15**, 331 (2012).

[15] Y. Qin, T. Yu, S. Deng, X.-Y. Zhou, D. Lin, Q. Zhang, Z. Jin, D. Zhang, Y.-B. He, H.-J. Qiu, L. He, F. Kang, K. Li, and T.-Y. Zhang, Nat. Commun. **13**, 3784 (2022).

[16] D.-S. Ko, W.-J. Lee, S. Sul, C. Jung, D.-J. Yun, H.-G. Kim, W.-J. Son, J. G. Chung, D. W. Jung, S. Y. Kim, J. Kim, W. Lee, C. Kwak, J. K. Shin, J.-H. Kim, and J. W. Roh, NPG Asia Mater. **10**, 266 (2018).

[17] V. Jovic, R. J. Koch, S. K. Panda, H. Berger, P. Bugnon, A. Magrez, K. E. Smith, S. Biermann, C. Jozwiak, A. Bostwick, E. Rotenberg, and S. Moser, Phys. Rev. B **98**, 241101 (2018).

[18] R. M. Martin, *Electronic Structure: Basic Theory and Practical Methods* (Cambridge University Press, 2004).

[19] O. Hellman, P. Steneteg, I. A. Abrikosov, and S. I. Simak, Phys. Rev. B **87**, 104111 (2013).

[20] L. Monacelli, R. Bianco, M. Cherubini, M. Calandra, I. Errea, and F. Mauri, J. Condens. Matter Phys. **33**, 363001 (2021).

[21] J.-J. Zhou, O. Hellman, and M. Bernardi, Phys. Rev. Lett. **121**, 226603 (2018).

[22] S. Poncé, E. Margine, C. Verdi, and F. Giustino, Comput. Phys. Commun. **209**, 116 (2016).

[23] A. Lanzara, P. V. Bogdanov, X. J. Zhou, S. A. Kellar, D. L. Feng, E. D. Lu, T. Yoshida, H. Eisaki, A. Fujimori, K. Kishio, J.-I. Shimoyama, T. Noda, S. Uchida, Z. Hussain, and Z.-X. Shen, Nature **412**, 510 (2001).

[24] P. D. Johnson, T. Valla, A. V. Fedorov, Z. Yusof, B. O. Wells, Q. Li, A. R. Moodenbaugh, G. D. Gu, N. Koshizuka, C. Kendziora, S. Jian, and D. G. Hinks, Phys. Rev. Lett. **87**, 177007 (2001).

[25] Z. Li, M. Wu, Y.-H. Chan, and S. G. Louie, Phys. Rev. Lett. **126**, 146401 (2021).

[26] F. Mazzola, J. W. Wells, R. Yakimova, S. Ulstrup, J. A. Miwa, R. Balog, M. Bianchi, M. Leandersson, J. Adell, P. Hofmann, and T. Balasubramanian, Phys. Rev. Lett. **111**, 216806 (2013).

[27] F. Mazzola, T. Frederiksen, T. Balasubramanian, P. Hofmann, B. Hellsing, and J. W. Wells, Phys. Rev. B **95**, 075430 (2017).

[28] C. C. Tsuei, D. M. Newns, C. C. Chi, and P. C. Pattnaik, Phys. Rev. Lett. **65**, 2724 (1990).

[29] J. P. Carbotte, Rev. Mod. Phys. **62**, 1027 (1990).

[30] P. Giannozzi, S. Baroni, N. Bonini, M. Calandra, R. Car, C. Cavazzoni, D. Ceresoli, G. L. Chiarotti, M. Cococcioni, I. Dabo, A. D. Corso, S. de Gironcoli, S. Fabris, G. Fratesi, R. Gebauer, U. Gerstmann, C. Gougoussis, A. Kokalj, M. Lazzeri, L. Martin-Samos, N. Marzari, F. Mauri, R. Mazzarello, S. Paolini, A. Pasquarello, L. Paulatto, C. Sbraccia, S. Scandolo, G. Sclauzero, A. P. Seitsonen, A. Smogunov, P. Umari, and R. M. Wentzcovitch, J. Phys. Condens. Matter **21**, 395502 (2009).

[31] S. Baroni, S. de Gironcoli, A. Dal Corso, and P. Giannozzi, Rev. Mod. Phys. **73**, 515 (2001).

[32] A. A. Mostofi, J. R. Yates, G. Pizzi, Y.-S. Lee, I. Souza, D. Vanderbilt, and N. Marzari, Comput. Phys. Commun. **185**, 2309 (2014).

[33] N. Marzari, A. A. Mostofi, J. R. Yates, I. Souza, and D. Vanderbilt, Rev. Mod. Phys. **84**, 1419 (2012).

[34] C.-H. Park, F. Giustino, M. L. Cohen, and S. G. Louie, Phys. Rev. Lett. **99**, 086804 (2007).

[35] Y. Luo, D. Desai, B. K. Chang, J. Park, and M. Bernardi, Phys. Rev. X **14**, 021023 (2024).

Chapter 6

DATA-DRIVEN COMPRESSION OF ELECTRON-PHONON INTERACTIONS

This chapter is a slightly modified version of the manuscript: Y. Luo, D. Desai, B. K. Chang, J. Park, and M. Bernardi, "Data-Driven Compression of Electron-Phonon Interactions", *Phys. Rev. X*, 14, 021023. D.D participated in the conception of the project, performed calculations, analyzed the data, and participated in the writing of the manuscript.

6.1 Introduction

Electrons in materials are subject to various interactions, including those with phonons, other electrons, and defects. Modeling of these interactions follows two main approaches—analytic treatments that qualitatively capture the main physics with minimal models using only a few parameters, and first-principles calculations aiming at quantitative accuracy but often requiring specialized workflows, high computational cost, and large amounts of data. A middle ground between these extremes would require formulating models of electron interactions that are economical, accurate, and interpretable. Examples of efficient models exist across domains—in quantum chemistry, low-rank approximations [1–3] can compress two-electron integrals to reduce the computational cost of post-Hartree Fock calculations [4, 5] and extract the critical vibrational modes in a chemical reaction [6, 7]; in correlated-electron physics, efficient parametrization of e-e interactions [8] enables the solution of functional renormalization-group flow [9, 10] and the Bethe-Salpeter equation [11, 12]. However, despite these isolated examples, it remains challenging to formulate widely applicable approaches to represent electron interactions both efficiently and accurately.

Focusing on electron-phonon (e-ph) interactions, analytic treatments such as deformation potential for acoustic phonons [13, 14] and the Fröhlich model for optical phonons [15], which use only a few parameters to describe e-ph interactions, are still widely utilized [16, 17]. In recent years, first-principles calculations of e-ph interactions using density functional theory (DFT) [18] and its linear-response variant, density functional perturbation theory (DFPT) [19], have enabled quantitative studies of properties ranging from transport to excited state dynamics to superconductivity [20–33]. Unlike the analytic models, in a typical first-principles calculation one represents the e-ph interactions using a multi-dimensional matrix with millions or billions of entries. This enormous number of parameters, which are computed rather than assumed, guarantees a faithful description of microscopic details such as the dependence on electronic states and phonon modes of e-ph interactions. Yet this complexity is also a barrier toward obtaining minimal models and tackling new physics. For example, materials with strong or correlated e-ph interactions need specialized treatments to capture polaron effects [28, 30, 34, 35] and electron correlations [36, 37]. Reducing the high dimensionality of first-principles e-ph interactions would allow one to more efficiently describe this physics while retaining quantitative accuracy. The development of data-driven methods to tackle the high-dimensional Hilbert space in the many-electron problem, including neural network states [38, 39] and tensor network methods [40–43], serve as inspiration.

Here we show a low-rank approximation of first-principles e-ph interactions which significantly accelerates e-ph calculations while using only a small fraction ($1-2\%$) of the data and preserving quantitative accuracy. This is achieved by developing SVD calculations of e-ph matrices in Wannier basis to achieve a minimal representation of e-ph coupling. We use our compressed e-ph matrices to compute a range of properties, including charge transport, spin relaxation, band renormalization, and superconductivity, both in metals and semiconductors. Across all benchmarks, the highly compressed e-ph representation achieves a quantitative accuracy comparable to the standard workflow, while also providing a deeper understanding of the dominant patterns governing e-ph interactions. Principal component analysis sheds light on the inherent compressibility of e-ph coupling matrices. Recent interesting work on improving the efficiency of e-ph calculations [44, 45] is distinct in method and scope from our data-driven approach.

6.2 Results

Compression of e-ph interactions

The key quantities in first-principles e-ph calculations are the e-ph matrix elements $g_{mn\nu}(\mathbf{k},\mathbf{q})$, which represent the probability amplitude for an electron in a band state $|n\mathbf{k}\rangle$, with band index n and crystal momentum $\mathbf{k}$, to scatter into a final state $|m\mathbf{k}+\mathbf{q}\rangle$ by emitting or absorbing a phonon with mode index ν, wave-vector $\mathbf{q}$, energy $\hbar\omega_{\nu\mathbf{q}}$, and polarization vector $\mathbf{e}_{\nu\mathbf{q}}$ [46]:

$$g_{mn\nu}(\mathbf{k},\mathbf{q}) = \sqrt{\frac{\hbar}{2\omega_{\nu\mathbf{q}}}} \sum_{\kappa\alpha} \frac{\mathbf{e}^{\kappa\alpha}_{\nu\mathbf{q}}}{\sqrt{M_\kappa}} \langle m\mathbf{k}+\mathbf{q}|\partial_{\mathbf{q}\kappa\alpha}V|n\mathbf{k}\rangle\,, \tag{6.1}$$

where $\partial_{\mathbf{q}\kappa\alpha}V \equiv \sum_p e^{i\mathbf{q}\mathbf{R}_p}\partial_{p\kappa\alpha}V$ is the lattice-periodic e-ph perturbation potential, given by the change in the DFT Kohn-Sham potential with respect to the position of atom κ (with mass M_κ and located in unit cell at $\mathbf{R}_p$) in the Cartesian direction α. The inset in Fig. 6.1(a) shows schematically such an e-ph scattering process. We separate the e-ph interactions into short- and long-ranged [47–53],

$$g_{mn\nu}(\mathbf{k},\mathbf{q}) = g^L_{mn\nu}(\mathbf{k},\mathbf{q}) + g^S_{mn\nu}(\mathbf{k},\mathbf{q}). \tag{6.2}$$

The long-range part $g^L_{mn\nu}(\mathbf{k},\mathbf{q})$ includes dipole (Fröhlich) and quadrupole contributions, which can be written analytically, using classical electromagnetism, in terms of Born effective charges and dynamical quadrupoles obtained from DFPT. The short-ranged part $g^S_{mn\nu}(\mathbf{k},\mathbf{q})$ cannot be written in closed form and needs numerical quantum mechanics to be computed, a consequence of the nearsightedness of electronic matter [54]. Because $g^S_{mn\nu}(\mathbf{k},\mathbf{q})$ is a smooth function of electron and phonon momenta, it is short-ranged in a real-space representation using a localized basis set such as atomic orbitals [55] or Wannier functions [46, 56].

The short-range e-ph coupling matrix in Wannier basis, $g^{\kappa\alpha}_{ij}(\mathbf{R}_e,\mathbf{R}_p)$, is obtained by transforming DFPT results computed on a coarse momentum grid $(\mathbf{k}_c,\mathbf{q}_c)$ [46]:

$$\begin{aligned} g^{\kappa\alpha}_{ij}(\mathbf{R}_e,\mathbf{R}_p) = \frac{1}{N_{\mathbf{k}_c}N_{\mathbf{q}_c}} \sum_{mn\mathbf{k}_c}\sum_{\mathbf{q}_c} e^{-i(\mathbf{k}_c\mathbf{R}_e+\mathbf{q}_c\mathbf{R}_p)} \\ \times\, \mathcal{U}^\dagger_{im}(\mathbf{k}_c+\mathbf{q}_c)\Delta V^S_{mn,\kappa\alpha}(\mathbf{k}_c,\mathbf{q}_c)\mathcal{U}_{nj}(\mathbf{k}_c), \end{aligned} \tag{6.3}$$

where $\mathcal{U}$ is a unitary transformation from Bloch to Wannier basis, and $\Delta V^S_{mn,\kappa\alpha}(\mathbf{k}_c,\mathbf{q}_c) = \langle m\mathbf{k}+\mathbf{q}|\partial_{\mathbf{q}\kappa\alpha}V^S|n\mathbf{k}\rangle$ is the short-ranged part of the perturbation potential in Bloch basis. To separate acoustic and optical modes, we carry out a rotation in atomic basis:

$$g^{\mu\alpha}_{ij}(\mathbf{R}_e,\mathbf{R}_p) = \sum_\kappa A^\mu_\kappa\, g^{\kappa\alpha}_{ij}(\mathbf{R}_e,\mathbf{R}_p), \tag{6.4}$$

where $A^\kappa_\mu = \exp\left(i\frac{2\pi}{N_{\mathrm{at}}}\kappa\mu\right)$ adds a relative phase to different atoms in the unit cell, and $\mu \in (0,...,N_{\mathrm{at}}-1)$ labels phonon modes (N_{at} is the number of atoms in the unit cell). This way, $\mu = 0$ corresponds to the acoustic subspace, where all the atoms in the unit cell move in phase, and $\mu \neq 0$ labels the optical modes. Here and below, we use a collective index $F = (ij, \mu\alpha)$ to label Wannier orbital pairs ij and phonon mode and direction $\mu\alpha$, simplifying the notation of the Wannier-basis e-ph matrices to $g^F(\mathbf{R}_e, \mathbf{R}_p)$.

When viewed as a matrix for each mode and orbital pair, $g^F(\mathbf{R}_e, \mathbf{R}_p)$ decays rapidly with lattice vectors $\mathbf{R}_e$ and $\mathbf{R}_p$ and has a typical size $N_{\mathbf{R}_e} \times N_{\mathbf{R}_p}$ ranging between $10^2 \times 10^2$ and $10^3 \times 10^3$. After carrying out SVD on $g^F(\mathbf{R}_e, \mathbf{R}_p)$, we obtain

$$g^F(\mathbf{R}_e, \mathbf{R}_p) = \sum_{\gamma} s^F_\gamma u^F_\gamma(\mathbf{R}_e)\, v^{F*}_\gamma(\mathbf{R}_p), \tag{6.5}$$

where s^F_γ is the singular value (SV) with index γ, and $u^F_\gamma(\mathbf{R}_e)$ and $v^{F*}{}_\gamma(\mathbf{R}_p)$ are the left and right singular vectors, respectively. One can interpret s^F_γ as the coupling strength between the generalized electron cloud $\sum_{\mathbf{R}_e} u^F_\gamma(\mathbf{R}_e) c^\dagger_i(\mathbf{R}_e) c_j(\mathbf{0})$ and phonon mode $\sum_{\mathbf{R}_p} v^{F*}_\gamma(\mathbf{R}_p)\big(b^\dagger_{\mu\alpha}(\mathbf{R}_p) + b_{\mu\alpha}(\mathbf{R}_p)\big)$, where $(c^\dagger, c)$ are creation and annihilation operators for electrons and $(b^\dagger, b)$ for phonons. For each channel F, there is a total of $\min(N_{\mathbf{R}_e}, N_{\mathbf{R}_p})$ SVs; we keep only the N_c largest ones, resulting in a truncated, low-rank e-ph matrix $\tilde{g}$:

$$\tilde{g}^F_{N_c}(\mathbf{R}_e, \mathbf{R}_p) = \sum_{\gamma=1}^{N_c} s^F_\gamma\, u^F_\gamma(\mathbf{R}_e)\, v^{F*}_\gamma(\mathbf{R}_p). \tag{6.6}$$

This matrix can be conveniently transformed to momentum space using

$$\begin{aligned}\tilde{g}^F_{N_c}(\mathbf{k}, \mathbf{q}) &= \sum_{\mathbf{R}_p, \mathbf{R}_e} e^{i\mathbf{k}\mathbf{R}_e + i\mathbf{q}\mathbf{R}_p}\, \tilde{g}^F_{N_c}(\mathbf{R}_e, \mathbf{R}_p) \\ &\approx \sum_{\gamma=1}^{N_c} s^F_\gamma\, u^F_\gamma(\mathbf{k})\, v^{F*}_\gamma(\mathbf{q}),\end{aligned} \tag{6.7}$$

where $u^F_\gamma(\mathbf{k}) = \sum_{\mathbf{R}_e} e^{i\mathbf{k}\mathbf{R}_e} u^F_\gamma(\mathbf{R}_e)$ and $v^{F*}_\gamma(\mathbf{q}) = \sum_{\mathbf{R}_p} e^{i\mathbf{q}\mathbf{R}_p} v^F_\gamma(\mathbf{R}_p)$ are singular vectors in momentum space. (Note that the long-range part of the e-ph matrix is added after interpolation of this short-ranged part.) Eq. (6.7) provides a generic parametrization of e-ph interactions, where by increasing the number of SVs one can systematically tune the accuracy and computational cost. According to the Eckart˘Young−Mirsky theorem, the truncated matrix $\tilde{g}$ obtained from SVD is an optimal low-rank approximation of e-ph interactions, in the sense that it minimizes the Frobenius-norm distance between the original and low-rank e-ph matrices [57]. From a computational viewpoint, Eq. (6.7) can greatly accelerate the calculation of e-ph interactions and the associated material properties, with a speed up by the inverse fraction of SVs kept in the truncated e-ph matrix. In most cases, we will keep only 1-2% of SVs, resulting in a 50-100 times speed-up for the key step in e-ph calculations (see Appendix 6.4 for details).

Error and Pareto-optimal interactions

To test the accuracy of the truncated e-ph matrix and its convergence with respect to the number of SVs (N_c), we define a relative error for the e-ph matrix averaged over electron bands and momenta, and phonon modes and wave-vectors:

$$\epsilon_g(N_c) = \frac{\sum_{mn\nu,\mathbf{kq}} |g_{mn\nu}(\mathbf{k},\mathbf{q}) - \tilde{g}^{N_c}_{mn\nu}(\mathbf{k},\mathbf{q})|^2}{\sum_{mn\nu,\mathbf{kq}} |g_{mn\nu}(\mathbf{k},\mathbf{q})|^2}, \tag{6.8}$$

where $\tilde{g}^{N_c}_{mn\nu}(\mathbf{k},\mathbf{q})$ is the low-rank (approximate) and $g_{mn\nu}(\mathbf{k},\mathbf{q})$ is the full first-principles e-ph matrix. Fig. 6.1(a) shows this error as a function of the fraction of SVs, $N_c/N_{\mathbf{R}_p}$, kept in the approximate matrix. In the language of model selection [57], the resulting curve of error versus number of parameters is the Pareto frontier for modeling e-ph interactions. We find that the error decreases rapidly with the number of SVs—for example, ϵ_g is as low as 1% when using only 2% of SVs, which achieves a $50\times$ compression of the original e-ph matrix. This error curve defines a Pareto-optimal region, highlighted in Fig. 6.1(a), where e-ph calculations are both accurate and parsimonious [57]. This region spans $1-4\%$ of SVs in most of our calculations—which corresponds to keeping $N_c \approx 10-50$ SVs—and suggests that many materials may possess only $\sim$10 dominant elementary e-ph interaction patterns. Accordingly, the e-ph coupling strength for each phonon mode [46, 58],

$$D_\nu(\mathbf{q}) = \hbar^{-1} \sqrt{2\omega_{\nu\mathbf{q}} M_{\mathrm{uc}} \sum_{mn} |g_{mn\nu}(\mathbf{k}=\Gamma,\mathbf{q})|^2 / N_b}\,, \tag{6.9}$$

(where M_{uc} is the mass of the unit cell and the band indices m and n run over N_b bands), shown in Fig. 6.1(b), can be computed accurately using just the largest 1.5% of SVs, matching closely the results using the full e-ph matrix.

Application to transport, spin and superconductivity

We showcase the accuracy of the low-rank approximate e-ph interactions by computing a wide range of material properties, including charge mobility, spin relaxation, phonon-assisted superconductivity, and phonon-induced band renormalization. Figs. 6.2(a) and 6.2(b) show the electron and hole mobility in silicon for temperatures between 100 and 400 K, obtained using the full e-ph matrix and compared with SVD using 1.5% of the SVs (see Appendix 6.4). The mobility is overestimated for electrons, and underestimated for hole carriers, despite the accuracy of the low-rank e-ph interactions in silicon (Fig. 6.1(a)). The error comes from the acoustic phonons, which interact weakly with electrons—and therefore are ignored in the low-rank e-ph matrix—but carry a considerable contribution to the

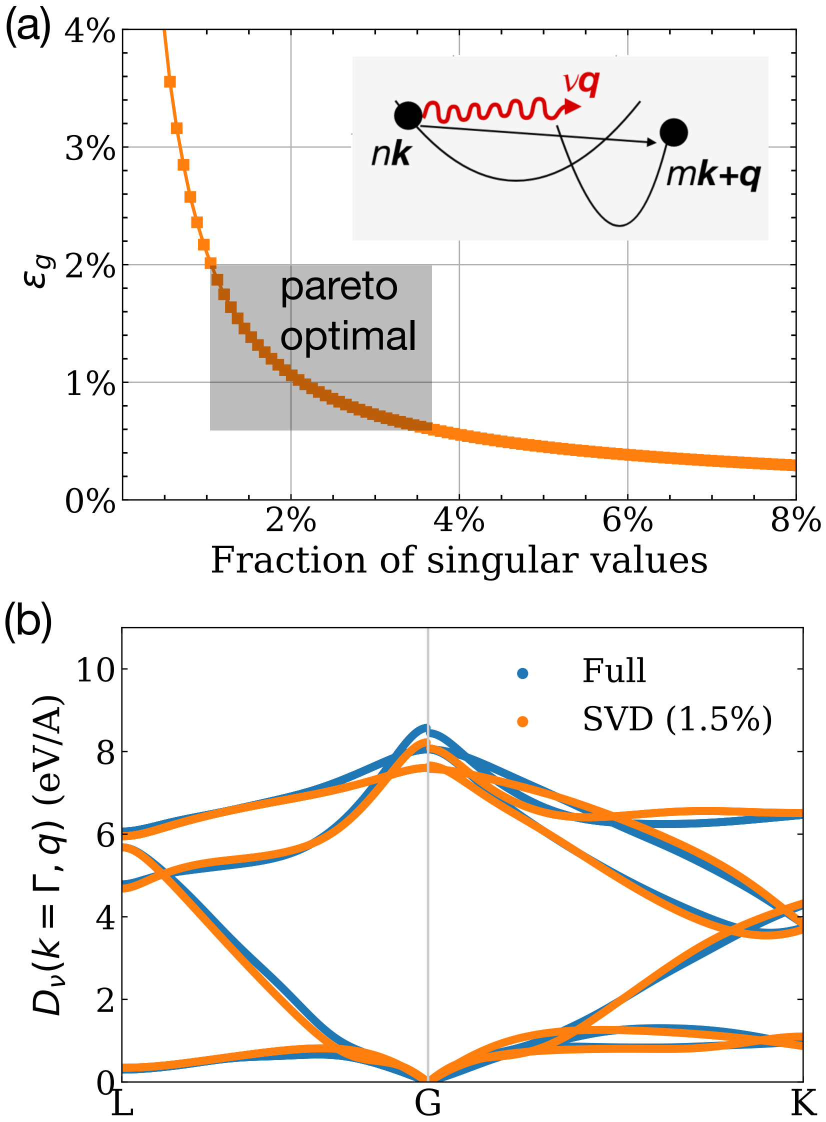

Figure 6.1: (a) Error on the compressed e-ph matrix, computed using Eq. (6.8), as a function of the fraction of SVs used in the low-rank approximation. The Pareto-optimal region is shown with a shaded rectangle. (b) Mode-resolved e-ph coupling strength computed using the full e-ph matrix (blue) and the low-rank approximate matrix (orange) for silicon. The full e-ph matrix elements are computed on a real-space grid with size $N_{\mathbf{R}_e} = 1325$ and $N_{\mathbf{R}_p} = 1325$, the smallest values to achieve convergence, setting the electron momentum to $\mathbf{k} = \Gamma$ and using the $N_b = 3$ highest valence bands. In the SVD calculation, we keep 20 out of 1325 SVs, corresponding to a $\sim$1.5% fraction of SVs, as noted in the legend.

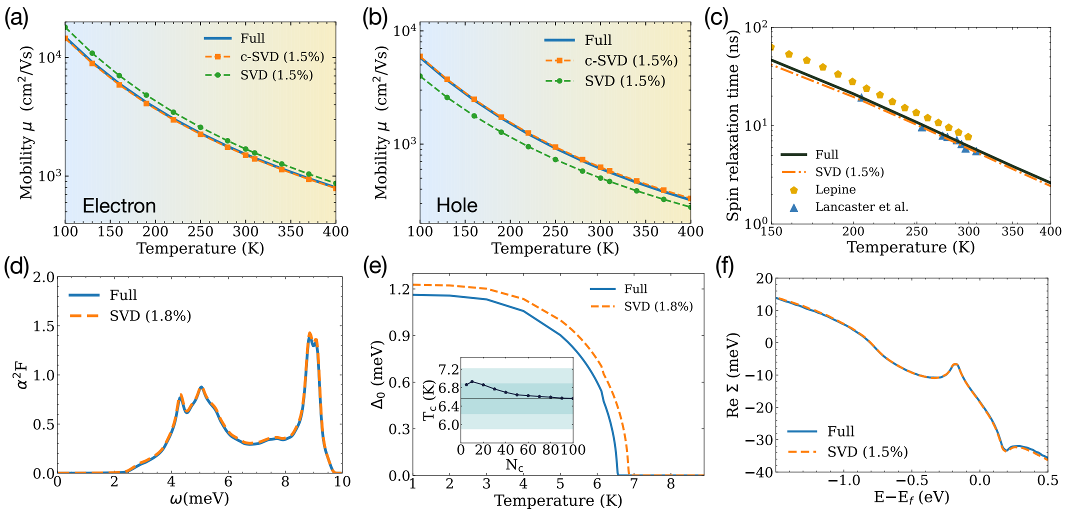

Figure 6.2: (a) Mobility of electrons in silicon, and (b) mobility of hole carriers in silicon, computed with the full e-ph matrix ($N_{\mathbf{R}_e} = N_{\mathbf{R}_p} = 1325$) and compared with standard and constrained SVD, in both cases using 1.5% of the SVs. (c) Spin relaxation times of electrons in silicon, computed with the full e-ph matrix ($N_{\mathbf{R}_e} = N_{\mathbf{R}_p} = 1325$) and using SVD with 1.5% of the SVs. Experimental data from Refs. [59, 60] are shown for comparison. (d) Eliashberg spectral function $\alpha^2F(\omega)$ for Pb, comparing full e-ph matrix ($N_{\mathbf{R}_e} = N_{\mathbf{R}_p} = 279$) with SVD results using 1.8% of the SVs. (e) Superconducting gap Δ_0 as a function of temperature, comparing full e-ph matrix results with SVD using 1.8% of the SVs. The inset shows the convergence of the critical temperature T_c with number of SVs; the darker (lighter) colored regions indicate 5% (10%) error relative to the full calculation. (f) Band renormalization for electronic states near the Dirac cone in graphene at 20 K, comparing the full calculation with SVD using 1.5% of the SVs.

mobility due to their large thermal occupation. To improve the treatment of acoustic phonons, we develop a constrained SVD (c-SVD) which preserves the deformation potential for long-wavelength acoustic phonons in the compressed e-ph matrix (see Appendix 6.4). When using c-SVD, the mobility computed using only 1.5% of the SVs is nearly identical to the full-matrix result for both carriers.

We also apply the low-rank approximation to spin-dependent e-ph matrices governing spin-flip e-ph interactions; these matrices enable first-principles calculations of spin relaxation times (SRTs) in centrosymmetric materials via the Elliot-Yafet mechanism [61] (see Appendix 6.4). The SRTs for electrons in silicon between 150 and 400 K are shown in Fig. 6.2(c). Our results from SVD with $N_c = 20$ (corresponding to ∼1.5% of the SVs) match closely the full e-ph matrix calculations and agree with experimental results [59, 60]. Different from charge transport, standard

SVD gives accurate SRTs in silicon because the optical phonons govern spin-flip processes. For materials where acoustic phonons contribute to spin relaxation, our c-SVD approach can be readily extended to the spin-dependent case.

Calculations of phonon-mediated superconductivity, presented here using lead (Pb) as an example, can also leverage our low-rank approximation (see Appendix 6.4). Fig. 6.2(d) compares the Eliashberg spectral function $\alpha^2F(\omega)$ from full e-ph matrix calculations with SVD results; using only the first $N_c = 5$ SVs (here equal to 1.8% of the SVs) suffices to reproduce the full calculation. We solve the isotropic Eliashberg equation self-consistently (see Appendix 6.4 for details) and compute the superconducting gap Δ_0 as a function of temperature (Fig. 6.2(e)) as well as the critical temperature T_c versus number of SVs (inset of Fig. 6.2(e)). The low-rank e-ph matrix with $N_c = 5$ SVs provides a gap function in good agreement with the full-matrix calculation, which can be further improved by using a larger fraction of SVs; the critical temperature for $N_c = 5$ SVs is very accurate, $T_c = 6.9$ K which is within 5% of the $T_c = 6.6$ K value obtained using the full e-ph matrix. This result implies that as few as five elementary e-ph interactions determine T_c in Pb. Finally, we compute band renormalization from e-ph interactions [62]] focusing on the contribution from the Fan-Migdal e-ph self-energy (see Appendix 6.4). The Debye-Waller term can also be added following Ref. [63]. Results for graphene show that band renormalization near the Dirac cone can be computed keeping only the five largest SVs; this highly compressed e-ph matrix correctly predicts the kinks near the Dirac cone and matches full e-ph matrix results over a 2 eV energy range. We also carry out convergence tests with respect to the fraction of SVs included in the calculation for all the materials studied here (see the Supplemental Material (section 6.5)). The rapid convergence with respect to the fraction of SVs guarantees that the full e-ph matrix calculation is not needed, and one can obtain accurate results by converging the desired property with respect to the fraction of SVs with minimal computational overhead.

While all the examples discussed above are for materials with nonpolar bonds, polar materials are even simpler to study with our compression method because the long-range (Frohlich) dipole contribution is dominant and is well modeled by an analytic formula using Born effective charges [47–49]. To illustrate this point, we demonstrate accurate mobility calculations in GaAs and $PbTiO_3$ using only 1% of the SVs (see the Supplemental Material (section 6.5)).

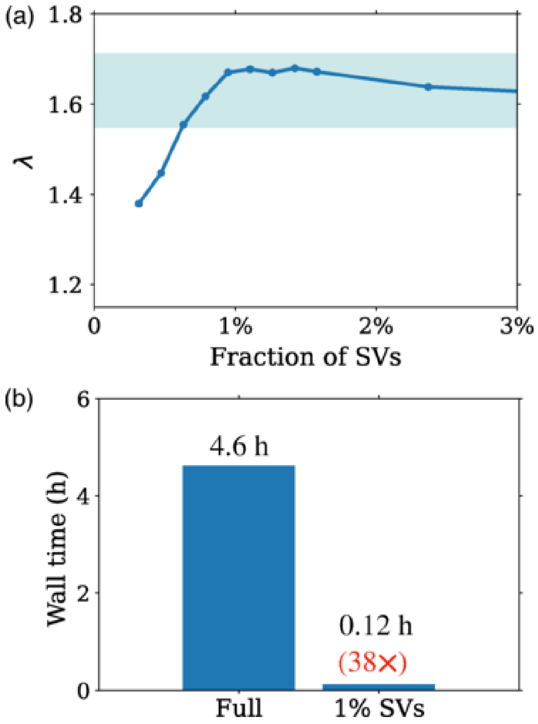

Figure 6.3: (a) e-ph coupling constant λ in doped monolayer MoS2 computed with our compression method using different fractions of SV. The doping concentration is 0.22 electrons per formula unit. The shaded region corresponds to an accuracy greater than 95$\%$ relative to the fully converged calculation. (b) Comparison of the wall time for computing the e-ph coupling constant λ with the full e-ph matrices and with our SVD compression technique using 1$\%$ of the SVs. The 38× speedup achieved by the SVD compression is indicated in red font.

Computational speedup from compression

We illustrate the computational speedup achieved by our compression method using the e-ph coupling constant λ in doped monolayer MoS2 as a case study [65]. Following Ref. [65], we employ a grid size of 288^2 $\mathbf{k}$- and $\mathbf{q}$- points for numerical integration and a Gaussain smearing of 0.002 Ry. We also leverage the improved Brillouin-zone sampling technique where only electronic states in a small energy window (0.006 Ry) near the Fermi surface are included in the calculation. In Fig. 6.3(a), we show the convergence of λ with respect to the fraction of SVs. The shaded region corresponds to an accuracy greater than 95$\%$ compared to the fully converged result. Similar to other quantities computed in this work, λ converges rapidly with the fraction of SVs; in particular, using only 1$\%$ of the SVs gives λ within 2$\%$ of the converged result. Figure 6.3(b) compares the computational wall time for the calculation employing the full e-ph matrices and for our SVD compression

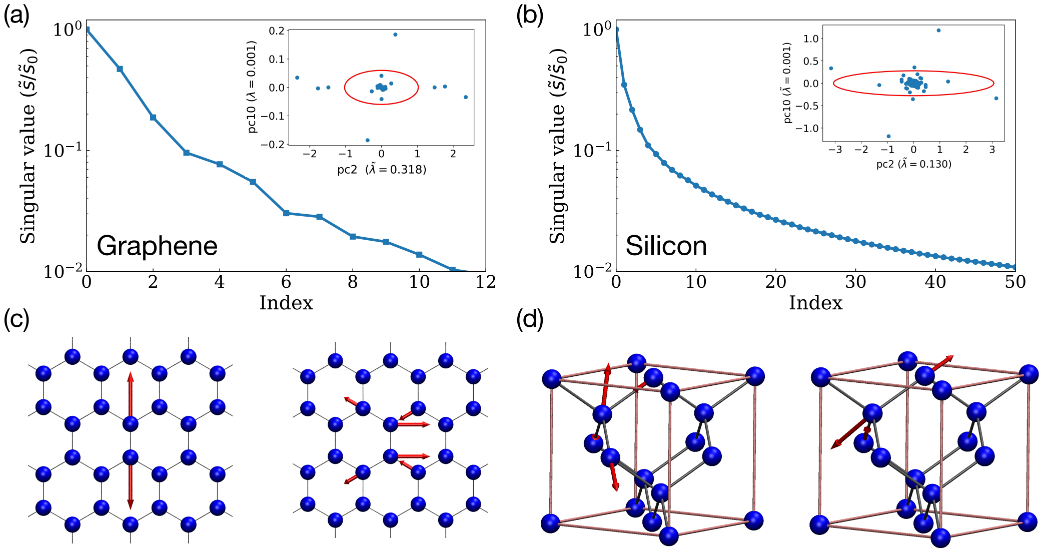

Figure 6.4: (a) Decay of the SVs in graphene and (b) decay of the SVs in silicon, shown by plotting the SVs referenced to the largest SV. Here, $\tilde{s}_i$ refers to the SVs averaged over Wannier orbitals and vibrational modes, $\tilde{s}_i = \sqrt{\sum_F (s_i^F)^2}$. The respective insets show the real part of the 2nd versus 10th principal components, obtained from the PCA of the e-ph matrices; in parentheses we give the fraction of explained variance [64], $\tilde{\lambda}_i = \sigma_i^2/\sum_i \sigma_i^2$, where σ_i^2 is the variance of the i-th principal component. The red oval shows the standard deviation of the corresponding principal components, obtained by dropping feature vectors with norm smaller than $10^{-3} \times \tilde{s}_0$. (c) Atomic vibrations associated with the dominant e-ph interactions in graphene, and (d) the same quantity in silicon, obtained by analyzing the phonon singular vectors, $\tilde{v}(\kappa\alpha\mathbf{R}_p)$ in Eq. (6.10), for the two largest SVs.

method with 1% SVs (note that both calculations use the same improved Brillouin-zone sampling scheme). Our approach achieves a speedup by 38 times relative to using the full e-ph matrices; if we count solely the time for e-ph interpolation, the speedup is 83 times. This example illustrates the 1–2 orders of magnitude speedup deriving from compressing the e-ph matrices with SVD. For a more detailed analysis of computational complexity, see Appendix 6.4.

Dominant modes and principal-component analysis

To understand the inherent compressibility of the e-ph matrices, we analyze the SV spectrum in graphene and silicon (Figs. 6.4(a) and 6.4(b)). In both materials, the SVs decay rapidly, dropping by $1-2$ orders of magnitude from the largest to the 10th largest SV. In principal component analysis (PCA) [57, 64], this decay can be understood as a consequence of high-variance generalized directions in the e-ph matrix, $g^F(\mathbf{R}_e, \mathbf{R}_p)$, which capture the vast majority of the physics, while other principal components can be viewed as noise and neglected [64]. We carry out PCA by treating each row of the matrix $g^F(\mathbf{R}_e, \mathbf{R}_p)$ as a feature vector, and find that the variance of the two leading principal components is one order of magnitude greater than for the 10th or following principal components, indicating that most of the physical information is already captured by the first few SVs (see the insets of Figs. 6.4(a) and 6.4(b)). This analysis reveals that only a few atomic vibrational patterns dominate e-ph coupling. Although these dominant modes are not known a priori, they can be learned efficiently with SVD. We also apply the PCA to lead (see Fig. 6.8 in Supplemental Material (section 6.5))]) and observe a similar rapid decay of the SVs. We remark that the dimensionality reduction is general: it occurs in all the materials studied here, and it is associated to the rapid decay of the SVs, which we view as a consequence of the nearsightedness of electronic interactions.

We visualize the atomic vibrations with dominant e-ph interactions by analyzing the vibrational singular vectors. To that end, we introduce a modified SVD that includes Wannier orbitals and phonon modes in the decomposition:

$$g_{ij}^{\kappa\alpha}(\mathbf{R}_e, \mathbf{R}_p) = \sum_{\gamma} s_\gamma \, \tilde{u}_\gamma(ij\mathbf{R}_e) \, \tilde{v}_\gamma^*(\kappa\alpha\mathbf{R}_p). \tag{6.10}$$

In this global SVD, the singular vectors $\tilde{u}$ depend only on electron variables and $\tilde{v}$ only on phonon variables. This way, the phonon singular vectors $\tilde{v}_\gamma^*(\kappa\alpha\mathbf{R}_p)$ can be interpreted as local vibrational modes (in the Wigner-Seitz cell associated with the coarse grid [46]) and visualized to study the dominant e-ph couplings. We show these singular vectors for the two modes with largest SVs in graphene and silicon in Figs. 6.4(c) and 6.4(d), using arrows on each atom, with length proportional to the singular vector $\tilde{v}_\gamma^*(\kappa\alpha\mathbf{R}_p)$, to indicate the atomic displacements in the modes obtained from SVD.

In graphene, where the electronic states consist of p_z orbitals centered on each carbon atom, the dominant mode resembles a longitudinal optical phonon that brings the p_z orbitals closer together in the unit cell. The second-strongest mode is a shear vibration resembling a transverse optical phonon, which spreads over multiple unit cells (Fig. 6.4(c)). For the other modes, we observe that the vibrational pattern progressively delocalizes over multiple unit cells for decreasing values of the SVs. In silicon, where the electronic states consist of sp^3-like Wannier orbitals oriented along the chemical bond directions, the two modes with dominant e-ph coupling are associated with compression and stretching of the bonds (Fig. 6.4(d)). The intuition gained from this mode analysis can aid the formulation of model Hamiltonians in chemically and structurally complex materials, where keeping only the dominant e-ph interactions can provide effective models of transport and polaron physics informed by first-principles calculations [66–70].

6.3 Discussion and conclusion

The accuracy of the low-rank e-ph matrices implies that current brute-force first-principles calculations overparametrize e-ph interactions, falling too far on the right side of the Pareto-optimal region in Fig. 6.1(a). Conversely, textbook approaches such as Holstein and Fröhlich models, which use only a handful of e-ph couplings, may fall short of achieving quantitative accuracy by using too few parameters. Our SVD compression in Wannier basis (followed by interpolation) provides a systematic route to achieve Pareto-optimal calculations. These optimal models enhance interpretability and enable a deeper understanding because they concentrate all the relevant e-ph physics in just a few parameters$-$in our case, the leading SVs and singular vectors, which represent dominant e-ph interactions.

In summary, our results unveil the hidden low-dimensional nature of e-ph interactions. While accurate, current first-principles calculations overparametrize these interactions due to a lack of a priori knowledge of the dominant atomic vibrational patterns governing e-ph coupling. We have shown that when this optimal representation is achieved via SVD, using only $10-20$ parameters (for each orbital pair and vibrational mode) is sufficient to obtain results with state-of-the-art accuracy. Surprisingly, this is only a small fraction ($1-2\%$) of the typical size of first-principles e-ph matrices. Compressing e-ph interactions significantly accelerates calculations of material properties ranging from transport to spin relaxation to superconductivity. Future work will extend these ideas to other electronic interactions, with the goal of advancing “precise but parsimonious” quantum many-body calculations in real materials.

6.4 Appendix

Computational complexity analysis

From a computational viewpoint, Eq. (6.7) can greatly accelerate the calculation of e-ph interactions and the associated material properties. The key bottleneck in these calculations is obtaining the e-ph matrix elements on fine momentum grids, $g_{mn\nu}(\mathbf{k}_f, \mathbf{q}_f)$, starting from the Wannier representation, with a cost scaling as $\mathcal{O}(N_{\mathbf{R}_p} N_{\mathbf{k}_f} N_{\mathbf{q}_f})$ for an optimal implementation [46] (for a fixed number of Wannier functions and atoms in the unit cell), where $N_{\mathbf{k}_f}$ and $N_{\mathbf{q}_f}$ are the number of points in the fine-momentum electron and phonon grids, with typical values of order $N_{\mathbf{k}_f} \approx N_{\mathbf{q}_f} \approx 10^6$. In contrast, when using SVD, this interpolation step costs only $\mathcal{O}(N_c N_{\mathbf{k}_f} N_{\mathbf{q}_f})$, with a speed up by a factor $N_{\mathbf{R}_p}/N_c$, the inverse fraction of SVs kept in the truncated e-ph matrix. In most cases, we will keep only $1-2\%$ of SVs, resulting in a ~100 times speed-up for the key step in e-ph calculations. We show specific timing comparisons for all the materials studied in this work in Fig. 6.5 of the Supplemental Material(section 6.5). In all cases, our algorithm achieves a speed up close to the ideal value of $N_{\mathbf{R}_p}/N_c$. The memory improvement is also dramatic. A converged transport calculation in silicon requires a $\mathbf{k}$ grid of 100^3 and $\mathbf{q}$ grid of 50^3 points [46]; on these fine grids, the memory required to store the entire e-ph matrix $g_{mn\nu}(\mathbf{k}_f, \mathbf{q}_f)$ is 700 TB, while the memory needed to store the singular vectors $u^F_\gamma(\mathbf{k}_f)$ and $v^F_\gamma(\mathbf{q}_f)$ is only 128 GB when we retain 1.5% of SVs, which guarantees accurate results as we show in Figs. 6.2(a) and 6.2(b). This efficiency removes the key bottleneck in first-principles e-ph calculations.

Mobility calculations

The first-principles mobility calculations in silicon follows our previous work [51]. We include the quadrupole contribution analytically for silicon. The quadrupole tensor can be written as

$$Q_{\mathrm{si},\alpha\beta\gamma} = (-1)^{\kappa+1} Q_{\mathrm{si}} |\epsilon_{\alpha\beta\gamma}|, \tag{6.11}$$

where $\epsilon_{\alpha\beta\gamma}$ is the Levi-Civita tensor and the value of $Q_{\mathrm{si}} = 13.67$ is taken from Refs. [71, 72].

We compute the phonon-limited mobility at temperature T using the BTE in the relaxation time approximation (RTA) [46]. We first obtain the e-ph scattering rate $\Gamma_{n\mathbf{k}}$ using Fermi's golden rule, which is equivalent to using the imaginary part of the lowest-order e-ph self-energy [73]:

$$\begin{aligned}\Gamma_{n\mathbf{k}} = \frac{2\pi}{\hbar} \frac{1}{\mathcal{N}_{\mathbf{q}}} \sum_{m\nu\mathbf{q}} &|g_{mn\nu}(\mathbf{k},\mathbf{q})|^2 \\ &\times [(N_{\nu\mathbf{q}} + 1 - f_{m\mathbf{k}+\mathbf{q}})\delta(\epsilon_{n\mathbf{k}} - \epsilon_{m\mathbf{k}+\mathbf{q}} - \hbar\omega_{\nu\mathbf{q}}) \\ &+ (N_{\nu\mathbf{q}} + f_{m\mathbf{k}+\mathbf{q}})\,\delta(\epsilon_{n\mathbf{k}} - \epsilon_{m\mathbf{k}+\mathbf{q}} + \hbar\omega_{\nu\mathbf{q}})],\end{aligned} \tag{6.12}$$

where $\mathcal{N}_{\mathbf{q}}$ is the number of $\mathbf{q}$ points and δ is the Dirac delta function. Then we obtain the mobility from the BTE by summing over contributions from different electronic states and scattering processes [46]:

$$\mu_{\alpha\beta}(T) = \frac{e}{n_c \Omega \mathcal{N}_{\mathbf{k}}} \int dE \left(-\frac{\partial f}{\partial E}\right) \sum_{n\mathbf{k}} \tau_{n\mathbf{k}}\, \mathbf{v}^{\alpha}_{n\mathbf{k}} \mathbf{v}^{\beta}_{n\mathbf{k}} \delta(E - \epsilon_{n\mathbf{k}}), \tag{6.13}$$

where Ω is the volume of the unit cell, $\tau_{n\mathbf{k}} = (\Gamma_{n\mathbf{k}})^{-1}$ are relaxation times, n_c is the carrier concentration, f is the Fermi-Dirac distribution, and $\mathcal{N}_{\mathbf{k}}$ is the number of $\mathbf{k}$ points; $\epsilon_{n\mathbf{k}}$ and $\mathbf{v}_{n\mathbf{k}}$ are electron energies and band velocities, respectively. Our calculations in silicon use a uniform grid with 200^3 $\mathbf{k}$ points and a uniform random grid with 10^5 $\mathbf{q}$ points, where $\mathbf{k}$ and $\mathbf{q}$ are electron and phonon momenta respectively. The delta function is approximated as a Gaussian with a 10 meV smearing [46].

c-SVD algorithm

Let us briefly describe our c-SVD algorithm. Similar to the acoustic sum rule (ASR) for the dynamical matrix [19], we formulate an ASR for the e-ph matrix elements:

$$g_{\nu_A}(\mathbf{k}, \mathbf{q} = 0) = 0, \tag{6.14}$$

where ν_A labels the acoustic modes, and we omit band indices for simplicity. The rationale for this e-ph ASR is that a rigid translation of the lattice will not change the electronic band structure. The real-space version of this e-ph ASR reads

$$\sum_{\kappa, \mathbf{R}_p} g^{\kappa\alpha}_{ij}(\mathbf{R}_e, \mathbf{R}_p) = \sum_{\mathbf{R}_p} g^{\mu=0,\alpha}_{ij}(\mathbf{R}_e, \mathbf{R}_p) = 0, \tag{6.15}$$

where $g^{\mu=0,\alpha}_{ij}(\mathbf{R}_e, \mathbf{R}_p)$ accounts for the acoustic subspace of the e-ph matrix defined in Eq. (6.4). With this ASR, the e-ph matrix for long-wavelength acoustic phonons can be approximated to first order in $\mathbf{q}$ as

$$\begin{aligned} \lim_{\mathbf{q}\to 0} g^{\mu=0,\alpha}(\mathbf{R}_e, \mathbf{q}) &= \lim_{\mathbf{q}\to 0} \sum_{\mathbf{R}_p} g^{\mu=0,\alpha}(\mathbf{R}_e, \mathbf{R}_p) e^{i\mathbf{q}\mathbf{R}_p} \\ &\approx i\mathbf{q} \cdot \mathbf{A}^{\alpha}(\mathbf{R}_e)\,, \end{aligned} \tag{6.16}$$

where we defined a real-space deformation potential, which in general can be anisotropic, as

$$\mathbf{A}^{\alpha}(\mathbf{R}_e) \equiv \sum_{\mathbf{R}_p} \mathbf{R}_p g^{\mu=0,\alpha}(\mathbf{R}_e, \mathbf{R}_p). \tag{6.17}$$

In the limit of $|\mathbf{q}| \to 0$, $\tilde{g}^{\mu=0,\alpha}(\mathbf{R}_e, \mathbf{q})$ vanishes linearly in $|\mathbf{q}|$, but the phonon occupation number diverges as $\frac{1}{|\mathbf{q}|}$; therefore in the long-wavelength limit acoustic phonon scattering is often important. This acoustic phonon contribution is challenging to preserve when using the compressed e-ph matrices because standard

SVD primarily captures large entries in the e-ph matrix. To address this point, we compress the e-ph matrix while conserving $\mathbf{A}^{\alpha}(\mathbf{R}_e)$ by imposing the following constraint:

$$\sum_{\mathbf{R}_p} \mathbf{R}_p\, \tilde{g}^{\mu=0,\alpha}_{N_c}(\mathbf{R}_e, \mathbf{R}_p) = \mathbf{A}^{\alpha}(\mathbf{R}_e). \tag{6.18}$$

Satisfying this set of linear equations leads to a constrained low-rank approximation [74], a more general optimization problem.

The c-SVD is applied only to the acoustic subspace, which corresponds to $F = (ij, \mu = 0\alpha)$, resulting in a compressed e-ph matrix of rank N_c:

$$\begin{aligned} \tilde{g}^{F}_{N_c}(\mathbf{R}_e, \mathbf{R}_p) &= \tilde{g}^{F}_{N_c-3}(\mathbf{R}_e, \mathbf{R}_p) \\ &\quad + \sum_{\beta\beta' \in (x,y,z)} \left(\delta \mathbf{A}^{\alpha}(\mathbf{R}_e)\right)_{\beta} \lambda_{\beta\beta'} \left(\mathbf{R}_p\right)_{\beta'} , \end{aligned} \tag{6.19}$$

where $\tilde{g}^{F}_{N_c-3}(\mathbf{R}_e, \mathbf{R}_p)$ is the truncated SVD of the e-ph matrix with $N_c - 3$ singular values (see Eq. (6.6)); $\delta\mathbf{A}^{\alpha}$ is the residual term for $\tilde{g}^{F}_{N_c-3}(\mathbf{R}_e, \mathbf{R}_p)$, defined as

$$\delta \mathbf{A}^{\alpha}(\mathbf{R}_e) = \mathbf{A}^{\alpha}(\mathbf{R}_e) - \sum_{\mathbf{R}_p} \mathbf{R}_p\, \tilde{g}^{\mu=0,\alpha}_{N_c-3}(\mathbf{R}_e, \mathbf{R}_p), \tag{6.20}$$

and $\lambda_{\beta\beta'}$ is the inverse of the overlap matrix between $\mathbf{R}_p$ vectors:

$$\sum_{\beta'} \lambda_{\beta\beta'} \sum_{\mathbf{R}_p} \left(\mathbf{R}_p\right)_{\beta'} \left(\mathbf{R}_p\right)_{\beta''} = \delta_{\beta\beta''}. \tag{6.21}$$

Using this approach, the compressed e-ph matrix $\tilde{g}^{F}_{N_c}(\mathbf{R}_e, \mathbf{R}_p)$ gives the same deformation potential as the full e-ph matrix in Eq. (6.17), and its rank is smaller than or equal to N_c. This c-SVD workflow requires only a minimal computational overhead relative to standard SVD.

Spin relaxation times

The first-principles calculation of SRTs in silicon follows our recent work [61]. The spin-flip relaxation time $\tau^{\text{flip}}_{n\mathbf{k}}$, for a band electron in state $|n\mathbf{k}\rangle$, accounts for the Elliott-Yafet spin relaxation mechanism and is computed using [61, 75, 76]

$$\begin{aligned} \frac{1}{\tau^{\text{flip}}_{n\mathbf{k}}} &= \frac{4\pi}{\hbar} \sum_{m\nu\mathbf{q}} |g^{\text{flip}}_{mn\nu}(\mathbf{k}, \mathbf{q})|^2 \\ &\quad \times \left[(N_{\nu\mathbf{q}} + 1 - f_{m\mathbf{k}+\mathbf{q}})\, \delta(\epsilon_{n\mathbf{k}} - \epsilon_{m\mathbf{k}+\mathbf{q}} - \hbar\omega_{\nu\mathbf{q}}) \right. \\ &\quad \left. + (N_{\nu\mathbf{q}} + f_{m\mathbf{k}+\mathbf{q}})\, \delta(\epsilon_{n\mathbf{k}} - \epsilon_{m\mathbf{k}+\mathbf{q}} + \hbar\omega_{\nu\mathbf{q}}) \right]. \end{aligned} \tag{6.22}$$

The key ingredients in this equation are the spin-flip e-ph matrix elements,

$$g^{\text{flip}}_{mn\nu}(\mathbf{k},\mathbf{q}) = \langle m\mathbf{k}+\mathbf{q} \Downarrow | \Delta\hat{V}_{\nu\mathbf{q}} | n\mathbf{k} \Uparrow \rangle \,, \tag{6.23}$$

with $\Downarrow$ and $\Uparrow$ denoting nearly spin-down and nearly spin-up states, respectively. These matrix elements describe the probability amplitude to flip the spin of a band electron due to a particular phonon mode $\nu\mathbf{q}$. The macroscopic spin relaxation time, $\tau_s(T)$, is a thermal average over electronic states of the spin-flip scattering rates [61]:

$$\tau_s(T) = \left\langle \frac{1}{\tau^{\text{flip}}_{n\mathbf{k}}} \right\rangle_T^{-1} = \left(\frac{\sum_{n\mathbf{k}} \frac{1}{\tau^{\text{flip}}_{n\mathbf{k}}} \left(-\frac{df_{n\mathbf{k}}}{dE}\right)}{\sum_{n\mathbf{k}} \left(-\frac{df_{n\mathbf{k}}}{dE}\right)} \right)^{-1} . \tag{6.24}$$

The SRT calculations employ a uniform grid with up to 140^3 $\mathbf{k}$ points and a 5 meV Gaussian smearing for the delta functions.

Eliashberg spectral function and superconducting gap

We carry out DFT calculations on lead (Pb) using the generalized gradient approximation [77] in the Quantum ESPRESSO code [78]. The ground state and electron wave functions are computed on a $14 \times 14 \times 14$ $\mathbf{k}$-point grid with a kinetic energy cutoff of 90 Ry, and the lattice constant is set to 4.88 Å. We use DFPT to calculate the phonon frequencies and eigenvectors, and the e-ph matrix elements $g_{mn\nu}(\mathbf{k},\mathbf{q})$, on coarse $6 \times 6 \times 6$ $\mathbf{k}$- and $\mathbf{q}$-point grids. We wannierize the 4 bands near the Fermi surface using the Wannier90 code [79], and obtain the e-ph matrices in Wannier basis using Perturbo [46]. The Eliashberg spectral function is computed as

$$\begin{aligned} \alpha^2F(\omega) &= \frac{1}{2}\sum_{\nu\mathbf{q}} \omega_{\nu\mathbf{q}}\, \lambda_{\nu\mathbf{q}}\, \delta(\omega-\omega_{\nu\mathbf{q}}), \quad \text{with} \\ \lambda_{\nu\mathbf{q}} &= \frac{1}{N(\epsilon_F)\omega_{\nu\mathbf{q}}} \sum_{mn\mathbf{k}} |g_{mn\nu}(\mathbf{k},\mathbf{q})|^2 \\ &\qquad \times \delta(\epsilon_{n\mathbf{k}}-\epsilon_F)\delta(\epsilon_{m\mathbf{k}+\mathbf{q}}-\epsilon_F), \end{aligned} \tag{6.25}$$

where $N(\epsilon_F)$ is the density of states at the Fermi energy (ϵ_F). The Eliashberg function $\alpha^2F(\omega)$ encodes the isotropic and retarded effective attraction between electronic states on the Fermi surface. Using $\alpha^2F(\omega)$, we obtain the gap function by solving the isotropic Migdal-Eliashberg Eq. [80]:

$$\begin{aligned} Z(i\omega_j) &= 1 + \frac{\pi k_B T}{\omega_j} \sum_{j'} \frac{\omega_{j'}}{\sqrt{\omega_{j'}^2 + \Delta^2(i\omega_j)}} \lambda(\omega_j - \omega_{j'}), \\ Z(i\omega_j)\Delta(i\omega_j) &= \pi k_B T \sum_{j'} \frac{\Delta(i\omega_{j'})}{\sqrt{\omega_{j'}^2 + \Delta^2(i\omega_{j'})}} \\ &\qquad \times \left[\lambda(\omega_j - \omega_{j'}) - \mu_c^*\right], \end{aligned} \tag{6.26}$$

where T is the temperature, $\omega_j = (2j+1)\pi k_B T$ is the Matsubara frequency, μ_c^* is the screened Coulomb potential, $Z(i\omega_j)$ is the mass renormalization function, $\Delta(i\omega_j)$ is the superconducting gap function, and $\lambda(\omega_j) = \int_0^\infty d\omega \alpha^2 F(\omega) \frac{2\omega}{\omega_j^2 + \omega^2}$ is the isotropic e-ph coupling strength.

For the numerical integrations in Eq. (6.25), we employ a **k**-point grid consisting of 400,000 quasi-random Sobol points (generated using SciPy[81]) and a **q**-point grid with 30,000 uniformly distributed random points; the delta functions are approximated as Gaussians with a 30 meV smearing for electrons and 0.1 meV smearing for phonons. Using the converged $\alpha^2 F(\omega)$ function, we set $\mu_c^* = 0.1$ and solve Eq. (6.26) iteratively for a range of temperatures. The critical temperature T_c is obtained as the temperature where $\Delta_o = \Delta(i\omega_j = i\pi k_B T)$ extrapolates to zero.

Band structure renormalization

The DFT ground state calculation in graphene uses the local density approximation with a norm-conserving pseudopotential from Pseudo DOJO[82]. We employ a 90 Ry plane-wave kinetic energy cutoff, a $60 \times 60 \times 1$ **k**-point grid, and a 2.46 Å lattice constant. For the DFPT calculation, we use coarse grids with $36 \times 36 \times 1$ **k**-points for electrons and $18 \times 18 \times 1$ **q**-points for phonons. The band structure renormalized by e-ph interactions, $\tilde{\epsilon}_{n\mathbf{k}}$, is obtained as the DFT band structure plus the real part of the e-ph self-energy evaluated on-shell,

$$\tilde{\epsilon}_{n\mathbf{k}} = \epsilon_{n\mathbf{k}} + \mathrm{Re}\, \Sigma_{n\mathbf{k}}(E = \epsilon_{n\mathbf{k}}, T). \tag{6.27}$$

We use the lowest-order (Fan-Migdal) e-ph self-energy,

$$\begin{aligned} \Sigma_{n\mathbf{k}}(E,T) &= \frac{1}{\mathcal{N}_\mathbf{q}} \sum_{\nu \mathbf{q} m} |g_{mn\nu}(\mathbf{k},\mathbf{q})|^2 \\ &\times \left[\frac{N_{\nu\mathbf{q}} + 1 - f_{m\mathbf{k}+\mathbf{q}}}{E - \epsilon_{m\mathbf{k}+\mathbf{q}} - \hbar\omega_{\nu\mathbf{q}} - i\eta} + \frac{N_{\nu\mathbf{q}} + f_{m\mathbf{k}+\mathbf{q}}}{E - \epsilon_{m\mathbf{k}+\mathbf{q}} + \hbar\omega_{\nu\mathbf{q}} - i\eta} \right], \end{aligned} \tag{6.28}$$

where η is a Lorentzian smearing [83]. We employ 10^7 uniform random $\mathbf{q}$-points for the numerical integration in Eq. (6.28) and set the Lorentzian smearing to 15 meV.

For more accurate band renormalization calculations, one could use Wannier function perturbation theory (WFPT) to overcome errors resulting from finite number of Wannier functions [84].

6.5 Supplemental Material

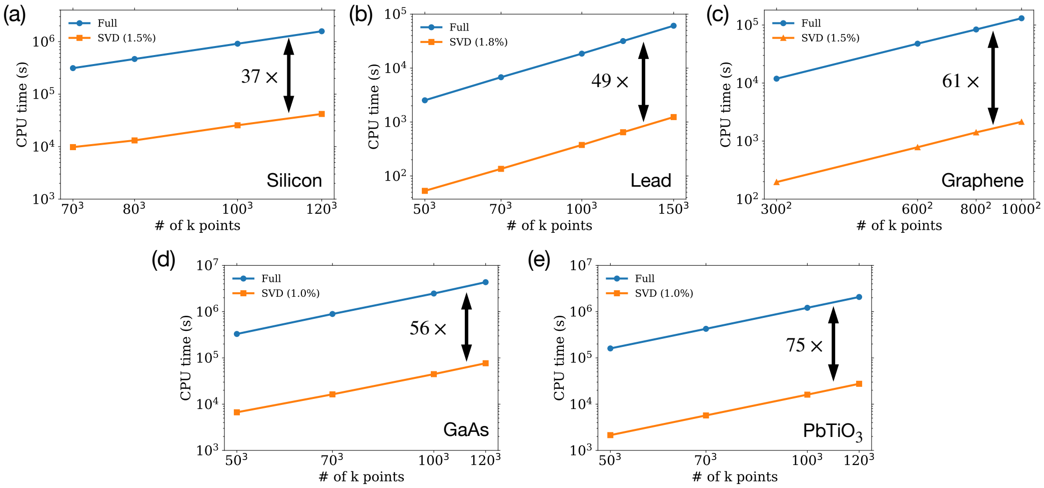

Figure 6.5: CPU time for interpolating e-ph matrix elements in momentum space using SVD compared to the full e-ph matrix for (a) silicon, (b) lead, (c) graphene, (d) GaAs, and (e) $PbTiO_3$. The numbers in the figures show the actual speedup of SVD method. The actual speedup of SVD method is close to the ideal speedup, the inverse of the inverse of the fraction of SVs.

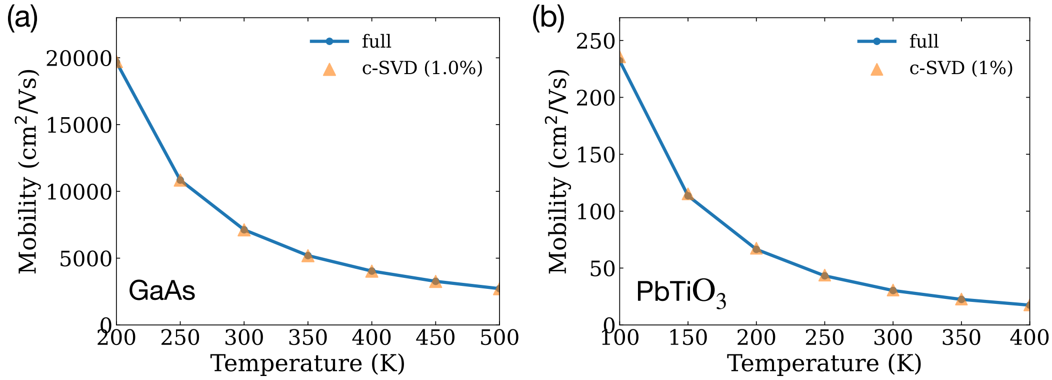

Figure 6.6: Mobility of electrons in two polar materials, (a) GaAs and (b) $PbTiO_3$, computed with the full e-ph matrix and compared with c-SVD, in both cases, uisng 1% SVs.

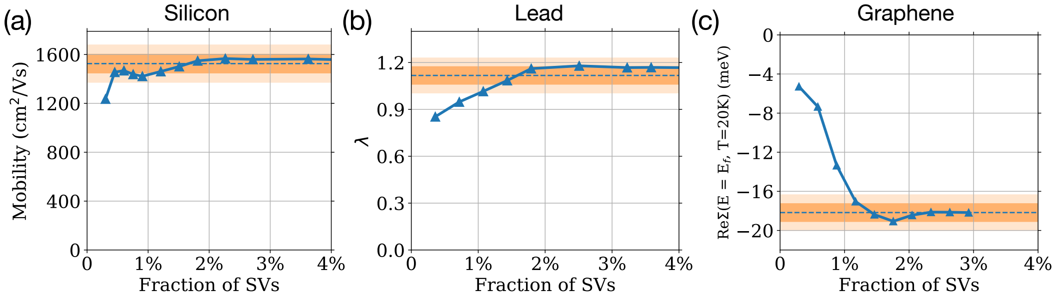

Figure 6.7: Convergence analysis of various properties with respect to the fraction of singular values (SVs): (a) electronic mobility in silicon at room temperature (T=300 K), (b) e-ph coupling constant in lead, (c) real part of Fan-Migdal e-ph self-energy in graphene at a specific k-point on the fermi surface, k =(0.3333, 0.2955, 0.0) in crystal coordinate, with the fermi enerngy at 0.6 eV above the Dirac cone. The darker orange shade shows the region where the error is less than 5%, and the lighter orange shade shows the region where the error is less than 10%. The dashed line is the reference result obtained from a calculation using the full e-ph matrix.

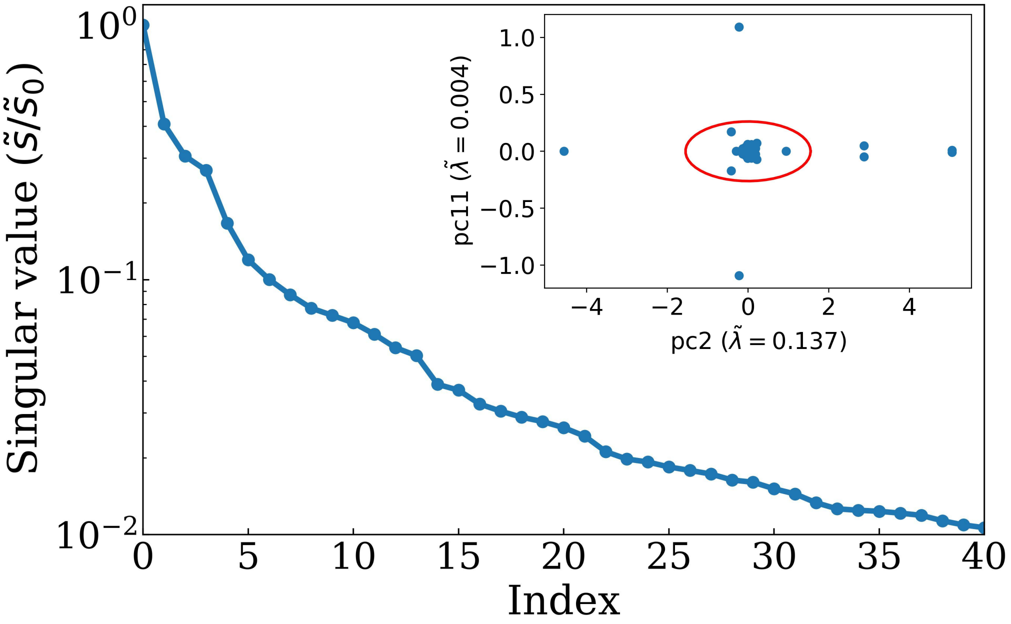

Figure 6.8: Decay of the SVs in lead shown by plotting the SVs referenced to the largest SV. The inset shows the real part of the 2nd versus 11th principal components, obtained from the PCA of the e-ph matrix.

Table 6.1: Mobility of electrons in GaAs.

	1% SVs	2% SVs	Full
Mobility @ 300K (cm^2/Vs)	7121	7126	7127
Relative error	0.084%	0.014%	0%

Table 6.2: Mobility of electrons in PbTiO$_3$.

	1% SVs	2% SVs	Full
Mobility @ 300K (cm^2/Vs)	30.69	30.46	29.97
Relative error	2.4%	1.6%	0%

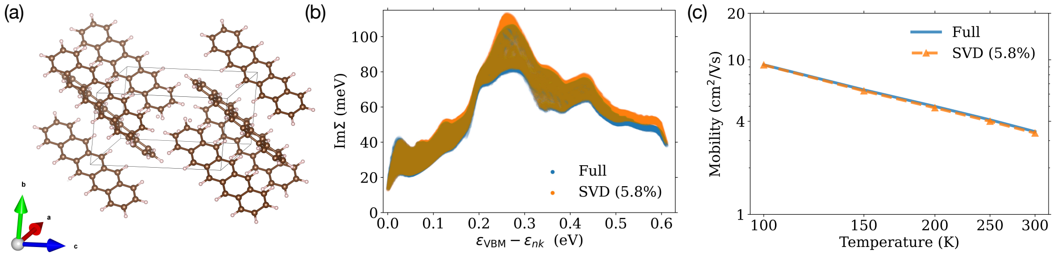

Figure 6.9: (a) Crystal structure of pentacene with 72 atoms in the unit cell. (b) The imaginary part of the lowest-order e-ph self-energy in the full calculation and in our compression method using only 5.8% of SVs for holes in pentacene. (c) The corresponding hole mobility in **a** direction versus temperature.

References

[1] B. I. Dunlap, Phys. Chem. Chem. Phys. **2**, 2113 (2000).

[2] B. Q. Pham and M. S. Gordon, J. Chem. Theory. Comput. **15**, 2254 (2019).

[3] J. Lu and L. Ying, J. Comput. Phys. **302**, 329 (2015).

[4] E. G. Hohenstein, R. M. Parrish, and T. J. Martínez, J. Chem. Phys. **137**, 044103 (2012).

[5] A. E. DePrince III and C. D. Sherrill, J. Chem. Theory. Comput. **9**, 2687 (2013).

[6] L. Riccardi, P. H. Nguyen, and G. Stock, The Journal of Physical Chemistry B **113**, 16660 (2009).

[7] Y. Yuan, Q. Zhu, R. Song, J. Ma, and H. Dong, Journal of Chemical Theory and Computation **16**, 4631 (2020).

[8] C. Husemann and M. Salmhofer, Phys. Rev. B **79**, 195125 (2009).

[9] W.-S. Wang, Y.-Y. Xiang, Q.-H. Wang, F. Wang, F. Yang, and D.-H. Lee, Phys. Rev. B **85**, 035414 (2012).

[10] W.-S. Wang, Z.-Z. Li, Y.-Y. Xiang, and Q.-H. Wang, Phys. Rev. B **87**, 115135 (2013).

[11] C. J. Eckhardt, C. Honerkamp, K. Held, and A. Kauch, Phys. Rev. B **101**, 155104 (2020).

[12] M. Wallerberger, H. Shinaoka, and A. Kauch, Phys. Rev. Research **3**, 033168 (2021).

[13] J. Bardeen and W. Shockley, Phys. Rev. **80**, 72 (1950).

[14] C. Herring and E. Vogt, Phys. Rev. **101**, 944 (1956).

[15] H. Fröhlich, Adv. Phys. **3**, 325 (1954).

[16] G. D. Mahan, *Many-Particle Physics*, 3rd ed. (Springer, 2000).

[17] A. M. Ganose, J. Park, A. Faghaninia, R. Woods-Robinson, K. A. Persson, and A. Jain, Nat. Commun. **12**, 2222 (2021).

[18] R. M. Martin, *Electronic Structure: Basic Theory and Practical Methods* (Cambridge University Press, 2004).

[19] S. Baroni, S. de Gironcoli, A. Dal Corso, and P. Giannozzi, Rev. Mod. Phys. **73**, 515 (2001).

[20] M. Bernardi, D. Vigil-Fowler, J. Lischner, J. B. Neaton, and S. G. Louie, Phys. Rev. Lett. **112**, 257402 (2014).

[21] W. Li, Phys. Rev. B **92**, 075405 (2015).

[22] J.-J. Zhou and M. Bernardi, Phys. Rev. B **94**, 201201(R) (2016).

[23] T.-H. Liu, J. Zhou, B. Liao, D. J. Singh, and G. Chen, Phys. Rev. B **95**, 075206 (2017).

[24] V. A. Jhalani, J.-J. Zhou, and M. Bernardi, Nano Lett. **17**, 5012 (2017).

[25] J. Ma, A. S. Nissimagoudar, and W. Li, Phys. Rev. B **97**, 045201 (2018).

[26] J.-J. Zhou, O. Hellman, and M. Bernardi, Phys. Rev. Lett. **121**, 226603 (2018).

[27] T. Sohier, D. Campi, N. Marzari, and M. Gibertini, Phys. Rev. Mater. **2**, 114010 (2018).

[28] J.-J. Zhou and M. Bernardi, Phys. Rev. Res. **1**, 033138 (2019).

[29] S. Poncé, W. Li, S. Reichardt, and F. Giustino, Rep. Prog. Phys. **83**, 036501 (2020).

[30] N.-E. Lee, J.-J. Zhou, H.-Y. Chen, and M. Bernardi, Nat. Commun. **11**, 1607 (2020).

[31] D. C. Desai, B. Zviazhynski, J.-J. Zhou, and M. Bernardi, Phys. Rev. B **103**, L161103 (2021).

[32] B. K. Chang, J.-J. Zhou, N.-E. Lee, and M. Bernardi, NPJ Comput. Mater. **8**, 63 (2022).

[33] Z. Zheng, Y. Shi, J.-J. Zhou, O. V. Prezhdo, Q. Zheng, and J. Zhao, Nat. Comput. Sci **3**, 532 (2023).

[34] Y. Luo, B. K. Chang, and M. Bernardi, Phys. Rev. B **105**, 155132 (2022).

[35] J. Lafuente-Bartolome, C. Lian, W. H. Sio, I. G. Gurtubay, A. Eiguren, and F. Giustino, Phys. Rev. Lett. **129**, 076402 (2022).

[36] J.-J. Zhou, J. Park, I. Timrov, A. Floris, M. Cococcioni, N. Marzari, and M. Bernardi, Phys. Rev. Lett. **127**, 126404 (2021).

[37] Z. Li, G. Antonius, M. Wu, F. H. da Jornada, and S. G. Louie, Phys. Rev. Lett. **122**, 186402 (2019).

[38] D. Pfau, J. S. Spencer, A. G. D. G. Matthews, and W. M. C. Foulkes, Phys. Rev. Res. **2**, 033429 (2020).

[39] J. Hermann, Z. Schätzle, and F. Noé, Nat. Chem. **12**, 891 (2020).

[40] U. Schollwöck, Rev. Mod. Phys. **77**, 259 (2005).

[41] G. K.-L. Chan and S. Sharma, Annu. Rev. Phys. Chem. **62**, 465 (2011).

[42] R. Orús, Ann. Phys. **349**, 117 (2014).

[43] F. Verstraete, T. Nishino, U. Schollwöck, M. C. Bañuls, G. K. Chan, and M. E. Stoudenmire, Nat. Rev. Phys. **5**, 273 (2023).

[44] A. S. Chaves, A. Antonelli, D. T. Larson, and E. Kaxiras, Phys. Rev. B **102**, 125116 (2020).

[45] T. Deng, G. Wu, M. B. Sullivan, Z. M. Wong, K. Hippalgaonkar, J.-S. Wang, and S.-W. Yang, npj Comput. Mater. **6**, 46 (2020).

[46] J.-J. Zhou, J. Park, I.-T. Lu, I. Maliyov, X. Tong, and M. Bernardi, Comput. Phys. Commun. **264**, 107970 (2021).

[47] P. Vogl, Phys. Rev. B **13**, 694 (1976).

[48] J. Sjakste, N. Vast, M. Calandra, and F. Mauri, Phys. Rev. B **92**, 054307 (2015).

[49] C. Verdi and F. Giustino, Phys. Rev. Lett. **115**, 176401 (2015).

[50] V. A. Jhalani, J.-J. Zhou, J. Park, C. E. Dreyer, and M. Bernardi, Phys. Rev. Lett. **125**, 136602 (2020).

[51] J. Park, J.-J. Zhou, V. A. Jhalani, C. E. Dreyer, and M. Bernardi, Phys. Rev. B **102**, 125203 (2020).

[52] G. Brunin, H. P. C. Miranda, M. Giantomassi, M. Royo, M. Stengel, M. J. Verstraete, X. Gonze, G.-M. Rignanese, and G. Hautier, Phys. Rev. Lett. **125**, 136601 (2020).

[53] G. Brunin, H. P. C. Miranda, M. Giantomassi, M. Royo, M. Stengel, M. J. Verstraete, X. Gonze, G.-M. Rignanese, and G. Hautier, Phys. Rev. B **102**, 094308 (2020).

[54] E. Prodan and W. Kohn, Proc. Natl. Ac. Sci. U.S.A. **102**, 11635 (2005).

[55] L. A. Agapito and M. Bernardi, Phys. Rev. B **97**, 235146 (2018).

[56] F. Giustino, M. L. Cohen, and S. G. Louie, Phys. Rev. B **76**, 165108 (2007).

[57] S. L. Brunton and J. N. Kutz, *Data-driven science and engineering: Machine learning, dynamical systems, and control* (Cambridge University Press, Cambridge, 2022).

[58] J. Sjakste, N. Vast, M. Calandra, and F. Mauri, Phys. Rev. B **92**, 054307 (2015).

[59] D. J. Lépine, Phys. Rev. B **2**, 2429 (1970).

[60] G. Lancaster, J. A. van Wyk, and E. E. Schneider, Proc. Phys. Soc. **84**, 19 (1964).

[61] J. Park, J.-J. Zhou, and M. Bernardi, Phys. Rev. B **101**, 045202 (2020).

[62] G. Grimvall, *The electron-phonon interaction in metals* (North-Holland, New York, 1981).

[63] H. Shang and J. Yang, J. Chem. Phys. **158**, 130901 (2023).

[64] P. Mehta, M. Bukov, C.-H. Wang, A. G. Day, C. Richardson, C. K. Fisher, and D. J. Schwab, Phys. Rep. **810**, 1 (2019).

[65] Y. Ge and A. Y. Liu, Phys. Rev. B **87**, 241408 (2013).

[66] N.-E. Lee, H.-Y. Chen, J.-J. Zhou, and M. Bernardi, Phys. Rev. Mater. **5**, 063805 (2021).

[67] Y. Luo, B. K. Chang, and M. Bernardi, Phys. Rev. B **105**, 155132 (2022).

[68] W. H. Sio, C. Verdi, S. Poncé, and F. Giustino, Phys. Rev. Lett. **122**, 246403 (2019).

[69] M. Setvin, C. Franchini, X. Hao, M. Schmid, A. Janotti, M. Kaltak, C. G. Van de Walle, G. Kresse, and U. Diebold, Phys. Rev. Lett. **113**, 086402 (2014).

[70] A. Janotti, J. B. Varley, M. Choi, and C. G. Van de Walle, Phys. Rev. B **90**, 085202 (2014).

[71] M. Royo and M. Stengel, Phys. Rev. X **9**, 021050 (2019).

[72] X. Gonze, B. Amadon, G. Antonius, F. Arnardi, L. Baguet, J.-M. Beuken, J. Bieder, F. Bottin, J. Bouchet, E. Bousquet, N. Brouwer, F. Bruneval, G. Brunin, T. Cavignac, J.-B. Charraud, W. Chen, M. Côté, S. Cottenier, J. Denier, G. Geneste, P. Ghosez, M. Giantomassi, Y. Gillet, O. Gingras, D. R. Hamann, G. Hautier, X. He, N. Helbig, N. Holzwarth, Y. Jia, F. Jollet, W. Lafargue-Dit-Hauret, K. Lejaeghere, M. A. Marques, A. Martin, C. Martins, H. P. Miranda, F. Naccarato, K. Persson, G. Petretto, V. Planes, Y. Pouillon, S. Prokhorenko, F. Ricci, G.-M. Rignanese, A. H. Romero, M. M. Schmitt, M. Torrent, M. J. van Setten, B. Van Troeye, M. J. Verstraete, G. Zérah, and J. W. Zwanziger, Comput. Phys. Commun. **248**, 107042 (2020).

[73] M. Bernardi, Eur. Phys. J. B **89**, 239 (2016).

[74] M. T. Chu, R. E. Funderlic, and R. J. Plemmons, Linear Algebra Its Appl. **366**, 157 (2003).

[75] R. J. Elliott, Phys. Rev. **96**, 266 (1954).

[76] Y. Yafet, *Solid State Physics* (Academic Press, New York, 1963).

[77] J. P. Perdew, K. Burke, and M. Ernzerhof, Phys. Rev. Lett. **77**, 3865 (1996).

[78] P. Giannozzi, S. Baroni, N. Bonini, M. Calandra, R. Car, C. Cavazzoni, D. Ceresoli, G. L. Chiarotti, M. Cococcioni, I. Dabo, A. D. Corso, S. de Gironcoli, S. Fabris, G. Fratesi, R. Gebauer, U. Gerstmann, C. Gougoussis, A. Kokalj, M. Lazzeri, L. Martin-Samos, N. Marzari, F. Mauri, R. Mazzarello, S. Paolini, A. Pasquarello, L. Paulatto, C. Sbraccia, S. Scandolo, G. Sclauzero, A. P. Seitsonen, A. Smogunov, P. Umari, and R. M. Wentzcovitch, J. Phys. Condens. Matter **21**, 395502 (2009).

[79] A. A. Mostofi, J. R. Yates, G. Pizzi, Y.-S. Lee, I. Souza, D. Vanderbilt, and N. Marzari, Comput. Phys. Commun. **185**, 2309 (2014).

[80] S. Poncé, E. Margine, C. Verdi, and F. Giustino, Comput. Phys. Commun. **209**, 116 (2016).

[81] P. Virtanen, R. Gommers, T. E. Oliphant, M. Haberland, T. Reddy, D. Cournapeau, E. Burovski, P. Peterson, W. Weckesser, J. Bright, S. J. van der Walt, M. Brett, J. Wilson, K. J. Millman, N. Mayorov, A. R. J. Nelson, E. Jones, R. Kern, E. Larson, C. J. Carey, İ. Polat, Y. Feng, E. W. Moore, J. VanderPlas, D. Laxalde, J. Perktold, R. Cimrman, I. Henriksen, E. A. Quintero, C. R.

Harris, A. M. Archibald, A. H. Ribeiro, F. Pedregosa, P. van Mulbregt, and SciPy 1.0 Contributors, Nat. Methods **17**, 261 (2020).

[82] M. van Setten, M. Giantomassi, E. Bousquet, M. Verstraete, D. Hamann, X. Gonze, and G.-M. Rignanese, Comput. Phys. Commun. **226**, 39 (2018).

[83] C.-H. Park, F. Giustino, M. L. Cohen, and S. G. Louie, Phys. Rev. Lett. **99**, 086804 (2007).

[84] J.-M. Lihm and C.-H. Park, Phys. Rev. X **11**, 041053 (2021).

Chapter 7

SUMMARY AND FUTURE DIRECTIONS

In conclusion, this thesis shows a unified framework that integrates e-ph interactions, magnetic fields, and Berry curvatures to calculate transport properties in a wide range of materials, and develops a corresponding first-principles code. These advances pave the way for studies of magnetotransport, magnetic materials, and topological quantum materials.

Chapter 2 focuses on calculations of magnetotransport in silicon, GaAs and graphene. Our calculations of magnetoresistance, Hall mobility, and Hall factor in silicon achieve excellent agreement with experiments. In GaAs, we find that Hall mobilities display an accuracy similar to charge transport calculations in zero magnetic field. The Hall factor in GaAs computed with the iterative (ITA) approach is notably closer to experimental values compared to the RTA Hall factor, despite the better accuracy of RTA mobilities in polar semiconductors. We also calculate magnetoresistance in graphene for different carrier concentrations, finding very large values, consistent with experimental data. These results validate our approach and show its ability to precisely predict magnetotransport in metals and semiconductors. Additionally, our calculations of the changes in steady-state occupations due to external fields reveal an alternating step-like pattern when plotted on the Dirac cone in graphene. This feature is attributed to strong electron-optical phonon interactions, and is prominent only when backscattering is taken into account. Taken together, our work enables accurate calculations of magnetotransport properties in these materials, and also provides a detailed understanding of these phenomena on a microscopic level.

In Chapter 3, we study e-ph interactions, phonon perturbation potentials, and the resitivity in the Dirac semimetal Na_3Bi. Our calculations of e-ph interactions and scattering rates show that a two-dimensional optical phonon corresponding to in-plane vibrations of Na atoms accounts for roughly half of the e-ph scattering and charge transport, despite the presence of 23 other phonon modes. We further explore the cause of this anisotropy between in-plane and out-of-plane directions by analyzing the real-space perturbation created by the 2D phonon. We find that a combination of out-of-phase motions of the Na atoms creates large perturbations at Bi sites, and therefore interact with Bi $p_{x/y}$ orbitals, causing strong e-ph coupling.

Our calculations further demonstrate that a distortion of Na atoms corresponding to the 2D phonon creates a dynamic phase transition to a Weyl semimetal. While similar 'killer' 2D modes that govern charge transport have been identified previously in organic crystals [1], they have not been predicted or observed in topological semimetals. Therefore, studying these phonons not only offers a potential route for ultrafast control of phase transitions, but also serves as a crucial first step in understanding the nature of electronic interactions in topological semimetals.

In Chapter 4, we integrate first-principles BTE and Berry curvature to compute topological transport effects such as the chiral anomaly and nonlinear Hall effect (NLHE). We calculate magnetotransport properties, such as magnetoconductance and magnetoresistance, in TaAs, and analyze the classical (Lorentz) and quantum (Berry curvature related) contributions to transport. Our calculation of the Berry curvature contribution to the magnetoconductance demonstrates positive values with increasing magnetic fields, consistent with experiments and previous theoretical work. We also perform calculations of nonlinear Hall responses in bulk $BaMnSb_2$, strained ML-WSe_2, and BL-WTe_2, and obtain results consistent with experimental data. Our calculations of the Berry curvature dipole in ML-WSe_2 and BL-WTe_2 show a significant change when e-ph interactions are taken into account, highlighting the interplay of electron interactions and band topology. Taken together, these calculations accurately quantify topological effects and their role in transport, and demonstrate a rich interplay between topology and e-ph interactions.

Chapter 5 focuses on the consequences of e-ph interactions beyond charge transport. We perform extensive calculations on (un)strained RuO_2, a correlated metal. Our calculations show that straining RuO_2 along the c-axis leads to a significant phonon anharmonicity and changes in the electronic structure. After correcting for phonon anharmonicity using the stochastic self-consistent harmonic approximation (SSCHA), we observe signatures of strong e-ph interactions, including distinctive kinks in the bandstructure due to e-ph band renormalization, and a high superconducting T_c. Our calculations achieve very good agreement with experiments, providing concrete evidence for the accuracy of e-ph interactions and their broad applicability beyond charge transport. We plan to extend these results by including altermagnetism in our calculations and analyzing its effects on superconductivity in RuO_2.

In Chapter 6, we focus on compressing e-ph interactions using data-driven techniques such as singular value decomposition (SVD). Using (un)constrained SVD method developed in our group, we compute e-ph interactions using a small fraction of singular values and achieve very good accuracy. We further compute mobilities, spin-relaxation times, Eliashberg spectral function, and band renormalization in a wide varity of materials from compresed e-ph interactions, obtaining results that closely match with those of the full e-ph matrix. This work reveals the inherent low-dimensional nature of e-ph interactions, allowing us to extract physical insights from such low-rank approximations, while also reducing the computational cost.

This thesis opens several research directions for future work. First, our BTE workflow primarily focuses on e-ph interactions and phonon-limited transport properties, but with recent advances in computing electron interactions with defects [2] and ionized impurities [3], it is now possible to extend these methods to study magnetotransport and topological transport at low temperatures in regimes governed by defects. Since the signatures of chiral transport are more prominent at low temperature, including electronic interactions beyond phonons could help bridge the accuracy gap between our calculations and experimental measurements.

Second, the current formalism to solve the BTE with magnetic fields and Berry curvature captures the dominant effects very accurately. However, an extension of the BTE to include inter-band velocity and Berry curvature terms is necessary to further improve the accuracy of our framework. In principle, this can be achieved using either density-matrix theory or many-body perturbation theory, in both cases by including off-diagonal velocity matrix elements in band space. However, due to several practical considerations, first-principles calculations of the coupled BTE with inter-band transitions are missing. Recently, our group has successfully developed and implemented an analogous formalism to compute inter-band contributions to spin relaxation from first-principles [4, 5]. These efforts point towards the feasibility of a more complete first-principles description of topological effects that also takes into account such inter-band transitions.

Third, we also consider the possibility of adding quantum corrections due to magnetic field. In our current BTE formalism, the effects of magnetic field are taken into account through a classical force term, which does not alter the electronic band structure. While this approach captures magnetotransport effects very accurately at low magnetic fields, this formalism is no longer valid at large fields, where additional corrections such as Zeeman splitting and Landau levels are needed. However, first-principles Landau level calculations are scarce, and implementing these corrections to electrons, phonons, and e-ph scattering is non-trivial. Future efforts in this direction will further enhance our understanding of magnetotransport properties at high fields. For example, it has been shown theoretically that the semiclassical description of chiral anomaly breaks down in the ’ultraquantum’ limit, where a Landau level description is needed to explain the unconventional behavior [6]. First-principles calculations that integrate magnetic field effects with e-ph interactions at strong fields are essential for developing a more comprehensive theory of magnetotransport.

Finally, our work in Chapters 4 and 6 provides a foundation to explore data-driven compression of band topology, allowing one to extract low-rank features and offer deeper insight into the topological properties of a material.

In conclusion, this thesis presents important advancements to the theory of first-principles transport calculations, enabling accurate predictions of novel effects such as magnetic fields and topology that were previously out of reach.

References

[1] G. Schweicher, G. D’Avino, M. T. Ruggiero, D. J. Harkin, K. Broch, D. Venkateshvaran, G. Liu, A. Richard, C. Ruzié, J. Armstrong, A. R. Kennedy, K. Shankland, K. Takimiya, Y. H. Geerts, J. A. Zeitler, S. Fratini, and H. Sirringhaus, Adv. Mater. **31**, 1902407 (2019).

[2] I.-T. Lu, J.-J. Zhou, and M. Bernardi, Phys. Rev. Mater. **3**, 033804 (2019).

[3] I.-T. Lu, J.-J. Zhou, J. Park, and M. Bernardi, Phys. Rev. Mater. **6**, L010801 (2022).

[4] J. Park, Y. Luo, J.-J. Zhou, and M. Bernardi, Phys. Rev. B **106**, 174404 (2022).

[5] J. Park, J.-J. Zhou, Y. Luo, and M. Bernardi, Phys. Rev. Lett. **129**, 197201 (2022).

[6] D. T. Son and B. Z. Spivak, Phys. Rev. B **88**, 104412 (2013).